Università degli Studi di Genova

Scuola Politecnica

Dipartimento di Ingegneria Meccanica (DIME)

Sez. MASET (Macchine, Sistemi Energetici e Trasporti)

Ph.D. Thesis in Fluid Machinery Engineering

XXX Cycle

Study of Hybrid Solar Gas Turbine System: T100 Modeling and Dynamic Analysis of Thermal Energy Storage

Supervisors:

Prof. Aristide F.Massardo

Prof. Ing. Alberto. Traverso

PhD Candidate:

Mariam Mahmood

Genova, November 2017

ABSTRACT

Concentrated Solar Power (CSP) hybrid gas turbine systems particularly based on the micro Gas Turbines (mGT) will be of great importance in future power infrastructure where energy security, economic feasibility and clean and efficient power generation are the key concerns. Integration of Thermal Energy Storage (TES) in CSP hybrid gas turbine systems could be a viable solution to overcome the intermittent nature of solar power, and increase the dispatchability. Based on this perception, a comprehensive analysis of both mGT cycle and TES technology should be undertaken, in order to achieve a better understanding of the behavior of TES and its interaction with other components in a hybrid gas turbine system. The present work intends to contribute to this analysis through mGT and TES system modeling and testing. This thesis is framed in two main parts: first part deals with T100 mGT modeling and second part focuses on the study of thermal storage systems. Regarding TES, detailed dynamic analysis of sensible heat storage is provided, while a preliminary study of thermochemical storage is conducted.

The mGT performance diagnosis involves the development for steady-state simulation of T100, model validation, and application in real operating conditions at the Ansaldo Energia AE-T100 test rig. Furthermore, diagnostic application of the AE-T100 model for whole mGT cycle is discussed with the help of two case studies at AE-T100 test rig. AE-T100 model has also been applied in the real operating conditions of micro Humid Air Turbine (mHAT) system located at Vrije Universiteit Brussel (VUB), to highlight the modeling capability of AE-T100 tool as well as monitoring the recuperator performance in the VUB-mHAT cycle.

The second part of this work concerns the dynamic modeling and experimental validation of a sensible TES system at laboratory scale, which is part of the Hybrid Solar Gas Turbine (HSGT) system developed at the University of Genova. TES is modeled with the help of a two-dimensional CFD model based on the ANSYS-FLUENT code, and a one-dimensional TRANSEO model employing software designed by the Thermochemical Power Group (TPG) at the University of Genova. The experimental validation, modeling capability to present the actual thermal stratification and State of Charge (SoC) of the TES, and scope of each model are also discussed. This study also highlighted the potential of TES system based on the monolithic structures for hybrid gas turbine systems i.e. low pressure drop across the TES

which are acceptable for the whole gas turbine hybrid system, modular structure of the storage and very low thermal losses.

In addition to the sensible heat storage system, ThermoChemical Storage (TCS) based on the redox cycle of cobalt oxides pair Co_3O_4\CoO was finally studied by the candidate during research period at Zhejiang University, China. The mathematical model which has been developed in MATLAB is based on the mass and energy conservation and reaction kinetics of the redox cycle, and has been validated against the experimental data available from literature. This work was aimed to study the process of thermochemical storage and understand the reaction kinetics of cobalt oxides with less computational effort. This analysis will help in design and optimization of the actual TCS system at the Zhejiang University, China.

Overall, the knowledge and modelling capabilities developed for mGT cycle and TES systems in this study will be merged to develop a single simulation tool for mGT based CSP hybrid systems, in the future.

Acknowledgment

I am highly indebted to several people for their extended help during the entire research work.

First of all, I would like to express my sincere gratitude to my supervisors, Prof. Aristide F. Massardo and Prof. Alberto Traverso for providing me this research opportunity, and for their scholarly inputs, consistent encouragement, mentorship, and support at all the levels. I have learned a lot under their valuable guidance, which will further help me to polish my research skills.

I am grateful to the National University of Sciences and Technology (NUST)-Pakistan for providing me financial support to carry out this research work. Indeed, this would not have been possible without their cooperation.

I would also like to thank my Chinese supervisor, Prof. Gang Xiao, for hosting me at Zhejiang University-China. In this regard, I am also thankful to Prof. Mario L. Ferrari (University of Genova) for his support and guidance during the research period in China. Thanks to my Chinese colleagues at Zhejiang University, for the warm welcome and all the support during my stay.

Thanks to all the researchers at the Thermochemical Power Group (TPG) and staff members for all the technical assistance, lab-scale experience, and for the good time spent together.

Special thanks to all the Pakistani friends in Genova, who extended their support all the time and made me feel like home during three years.

Finally, I would like to express my honest and eternal gratitude towards my family, for their everlasting and unconditional love, patience and encouragement. I would not have been able to accomplish this goal without their love, moral support and prayers.

Table of Contents

List of Figures

List of Tables

Nomenclature

Variables

T	Temperature [°C]
η	Efficiency/effectiveness
t	Time [s]
$e_{rel,i}$	Relative percent error of i^{th} parameter
V	Flow velocity [m/s]
p	Pressure [bar]
S_i	Source term for the i^{th} momentum equation
λ	Thermal conductivity [W/m.K]
K	Reaction rate constant (s^{-1})
C_p	Specific heat capacity [J/kg.K]
ε	Porosity
α_{fs}	Interfacial area density [area of the fluid / solid interface per unit volume of the porous zone, m^{-1}]
α	Permeability [m^2]
μ	Dynamic viscosity [Pa s]
h	Convective heat transfer coefficient [W/m^2. K]
ṁ	Mass flow rate [kg/s]
m	Mass [kg]
r	Radius [m]
S_h	Heat source (W)
H	Reaction enthalpy (J/mol)
L	Length of the storage [m]
Q	Energy [J]
U	Heat loss coefficient [W/m^2. K]
x	Variable

Subscripts

amb	ambient
c	charging
d	discharging
des	design
des,eff	design effectiveness
eq	equilibrium
out	outlet
rec	recuperator
rel	relative

in	inlet
f	fluid
i	any point inside the cycle
ins	insulation
min	minimum
max	maximum
s	solid
red	reduction
oxi	oxidation

Abbreviations

AS	Air Split
Btoe	Billion tons of oil equivalent
CFD	Computational Fluid Dynamics
CHP	Combined Heat and Power
CSP	Concentrated Solar Power
CRS	Central Receiver System
DSA	Dynamic Systems Analyzer
DG	Distributed Generation
F.S.	Full Scale
EFmGT	Externally Fired Micro Gas Turbine
FAR	Fuel Air Ratio
Gtoe	Giga tons of oil equivalent
HSGT	Hybrid Solar Gas Turbine
HTF	Heat Transfer Fluid
LTNE	Local Thermal Non-Equilibrium
LHV	Lower Heating Value
mGT	micro Gas Turbine

mHAT	micro Humid Air Turbine
PCM	Phase Change Material
RES	Renewable Energy Sources
RTD	Resistance Temperature Detector
RANS	Reynolds-Averaged Navier–Stokes
SGTU	Solar Gas Turbine Upgrade
TES	Thermal Energy Storage
TCS	ThermoChemical storage
TIT	Turbine Inlet Temperature
TOT	Turbine Outlet Temperature
RMS	Root Mean Square
UDF	User Defined Function

1 Introduction

In this chapter a brief overview of the global energy market, clean and efficient power systems, and status of the renewable energy sources, hybrid systems and energy storage system, is presented. An outline of the topics covered in this PhD Thesis is also provided.

1.1 Global Energy Scenario

Energy is the backbone of economy and a prerequisite for societal development and human well-being. In a politically, economically and environmentally volatile world, provision of clean and secure energy supply is essential to maintain the pace of economic growth of a country. Rapid population growth and urban sprawl particularly in non-OECD countries like China and India, is accelerating the overall energy demand. According to BP Statistical Review of World Energy 2017, the world's population is projected to increase by 1.5 billion to reach nearly 8.8 billion by 2035 [1].

This population rise is linked to the economic expansion. Much of the expected growth in the global economy is driven by the emerging economies, with China and India as the economic giants accounting for around half of this increase. China is likely to be the largest contributor of Gross Domestic Product (GDP) gains, followed by India. Consequently, their energy consumption is also rising significantly (Fig.1-1) [2].

These demographic and economic trends will also drive up the global energy demand. According to baseline scenario presented in Global Energy and Climate outlook (GECO) 2015 by European commission, primary energy demand increases from 13 Gtoe in 2010 to 18

Gtoe in 2030, and 22 Gtoe in 2050 (Fig.1.2). The structure of demand by fuel evolves with each fuel's relative scarcity: the share of oil is progressively declining, gas maintains a fairly constant share, coal makes up to a third of the total energy mix in 2050, and contribution of biomass and other renewables is increasing gradually representing 22% of the total mix in 2050 vs. 13% in 2010.

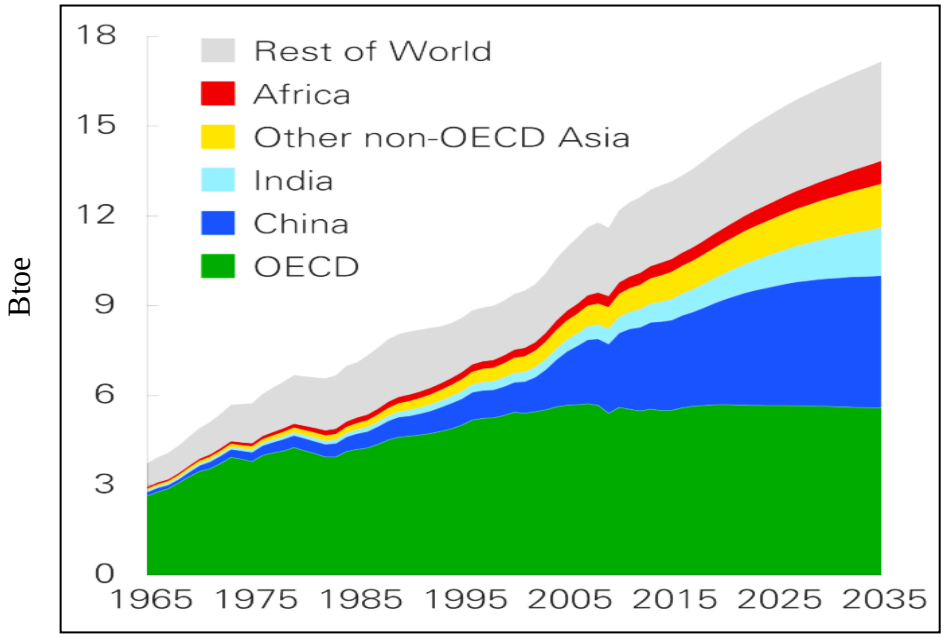

Figure 1-1 Energy consumption by region (Source: BP Statistical Review of World Energy 2017)

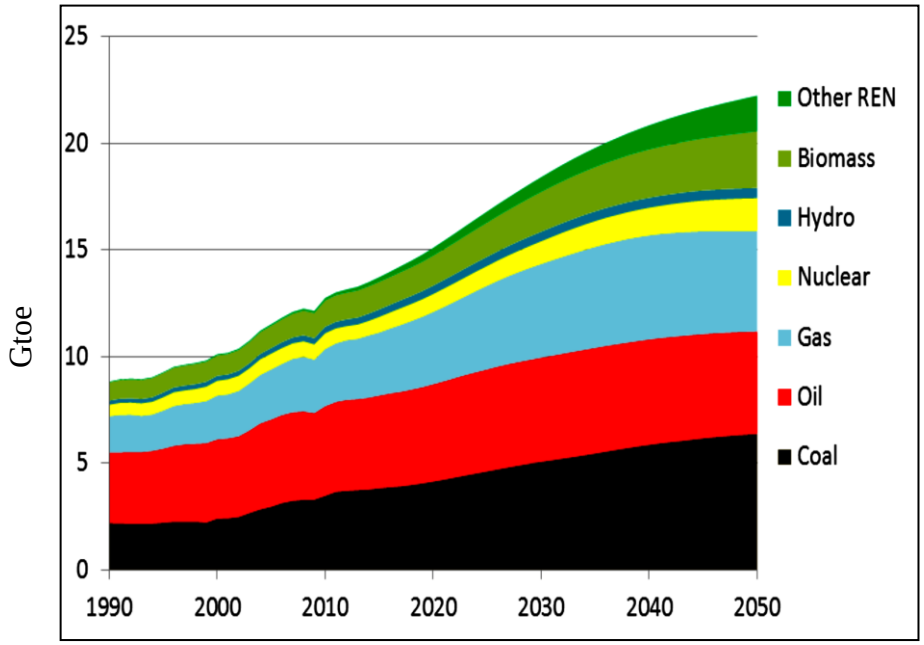

Figure 1-2 World energy demand, Baseline scenario (Source: GECO 2015 by European commission)

World final energy consumption per sector remains fairly constant over time: industry represents around 40% of the total, transport 25-30% and buildings 30-35% (Fig. 1-3). While it keeps increasing in the Baseline, final energy demand slows down significantly from 2020 onwards in the Global Mitigation scenario, stabilizing slightly above 10 Gtoe [3].

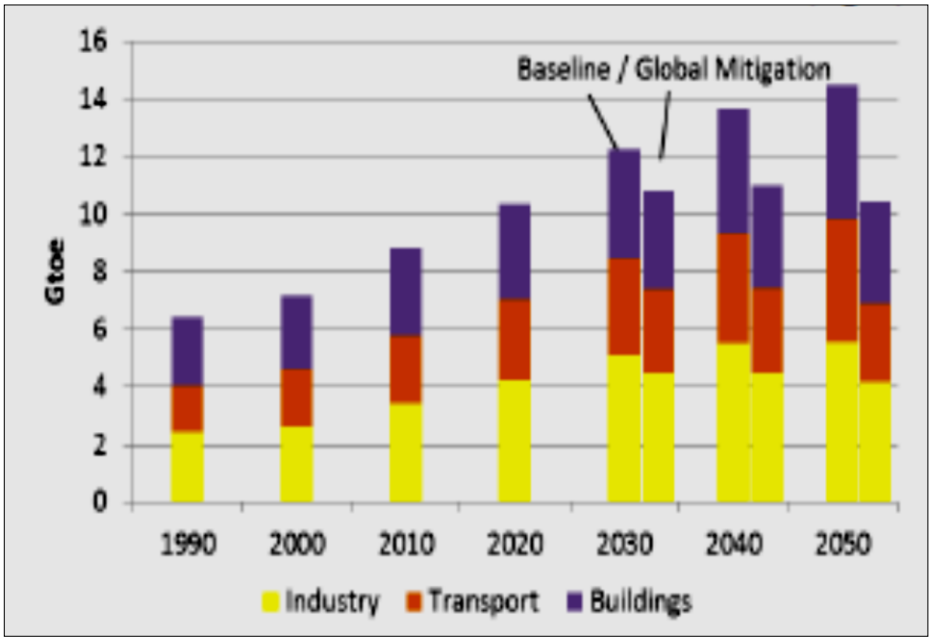

Figure 1-3 World final energy demand by sector, Baseline and Global Mitigation scenario (Source: GECO 2015 by European commission)

Since past few decades global energy landscape is in transition phase and energy market has been influenced by the fluctuating oil prices, energy deregulation, dwindling supply of conventional fuels and concerns about greenhouse gas emissions. The restricted supply of conventional energy resources have gradually become the bottleneck for economic development, while the greenhouse gas emission is another issue associated with conventional energy sources.

There are also concerns on other types of alternative energy resources. For instance, the recent nuclear accident in Japan has triggered intensive public scrutiny on nuclear energy developments which has been slowed down. Germany will shut down all nuclear power plants by 2022 and Switzerland will abandon plans to build new nuclear reactors and phase out nuclear power in the future [4].

All these factors urge the immediate measures to be taken at the international levels in order to relieve pressure on energy supply as well as considering the environment conservation. In this hour of need, international policies and mitigation plans like Kyoto protocol, UN Framework Convention on Climate Change (UNFCCC), Paris agreement, etc. are implemented to tackle the climate change through deployment of clean energy resources, energy savings, decarbonising the power sector with renewables and efficient technologies, and Carbon Capture and Storage (CCS). These regulations are framed in order to achieve the sustainable development goals without compromising the growth potential of developing countries in particular [5].

"Hold the increase in the global average temperature well below 2 °C above pre-industrial levels and pursuing efforts to limit the temperature increase to 1.5 °C above pre-industrial levels."

Paris climate change agreement, December 2016 [6].

1.2 Future of Power Generation: Clean and Efficient Energy Systems

The anticipated worldwide increase in energy demand and concern regarding environmental problems is fostering the utilization of more efficient technologies, in relevant applications. Global electricity markets are adopting clean and efficient energy production systems to mitigate the environmental deterioration caused by fossil fuel power plants, as well as to ensure affordable and reliable energy supply. This is supported by the continuing shift to less carbon-intensive energy for power generation and increased energy efficiency [7]. In this scenario, novel concepts like small-scale distributed generation (DG) systems, and hybrid systems based on renewables like concentrated solar power (CSP) and conventional fuels are expected to play a vital role in present and future power infrastructure.

1.2.1 Distributed Generation

Electricity transmission from generation site to the end user with minimum losses, and secure energy supply requires the transformation of conventional electricity transmission and distribution grid into an interactive and unified power supply network. Distributed generation (DG) will play a key role in this novel concept.

There is no common, clear consensus about the definition of DG, several definitions have been used in the scientific literature to distinguish DG from the central, large power Generation:

- The International Council on Large Electricity Systems (CIGRE) defines DG unit as a generation unit that is not centrally planned, not centrally dispatched, usually connected to the distribution network and smaller than 50-100 MW [8].
- The International Energy Agency (IEA) defines DG as generating plant serving a customer onsite or providing support to a distribution network, connected to the grid at distribution-level voltages [9].
- The Institute of Electrical and Electronics Engineers Inc. (IEEE) defines the DG as generation of electricity by facilities sufficiently smaller than central plants, usually 10 MW or less, so as to allow interconnection at nearly any point in the power system [10].

In general, DG covers a broad range of technologies: renewable energy systems supplying small scale power at sites close to the users, combined heat and power (CHP) units, back-up and peak load systems to increase the capacity. From the viewpoint of economic feasibility, the costs of installing the generators and producing the electricity can be comparatively inexpensive using the DG systems. Furthermore, combined generation of heat and power through small decentralized CHP plants enable the waste heat recovery from exhaust gases, thus significantly reduce the peak demand (peak shaving) of electricity and improves the overall system efficiency [11].

Hence, DG system is a novel concept for energy generation and delivery with minimum losses, in comparison with traditional central plant model. Figure 1.4 compares the traditional power network approach with distributed generation network. Decentralized power generation also provides advantages to those customers with sizeable heat loads through the operation of CHP units, and those who have access to low-cost fuels like biogas, bio-methane or local biofuels or have favourable climatic conditions; they can exploit renewable- based CHP units.

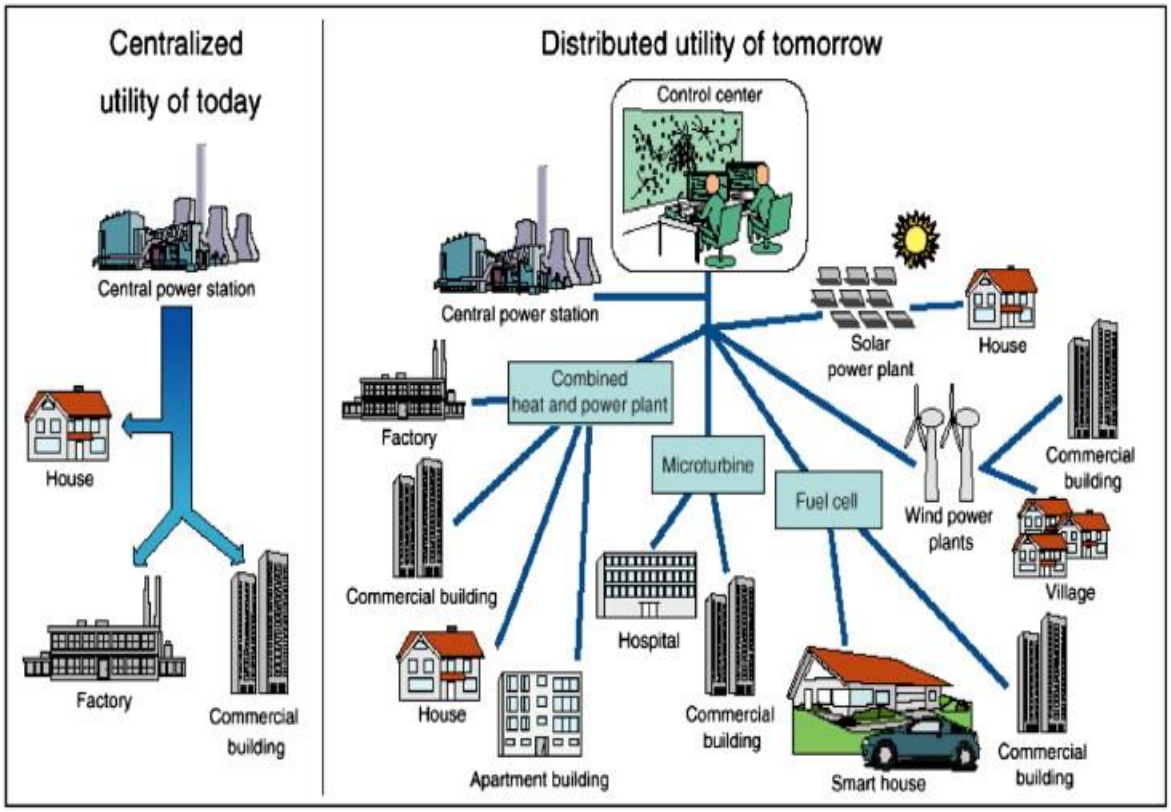

Figure 1-4 Central power station vs. Distributed generation network [12]

Governments are also encouraging CHP systems in order to achieve ambitious targets for energy efficiency and zero energy/emission buildings (ZEB). Ribarov et al. [13, 14] have quantified the economic potential for small-scale (micro grid) integrated CHP systems suitable for groups of buildings with aggregate electric loads in the 15-120 kW range. Technologies are evaluated for community building groups (CBGs) consisting of aggregation of pure residential entities and combined residential and light commercial entities. This research is focused on determination of the minimum load size (i.e., the smallest electric and thermal load for a given CBG that is supplied with electric, heating, cooling power from a CHP) for which a micro grid CHP system presents a technically and economically viable solution. These results suggest that micro grid CHP systems have the potential to be economically viable with relative independence of geographic location if adequately sized to match the specific load requirements.

To conclude, distributed generation (DG) reduces energy transmission losses, facilitates the integration of renewable energy sources, improves the system efficiency via CHP units, and assures the power quality and reliability.

1.2.2 Renewable Energy Sources (RES)

Renewable energy is critical to achieve number of high-level goals, including global climate change mitigation, energy security, and economic development. In the last decades, rising energy demand together with a growing awareness of environmental conservation has driven to the significant development of energy saving technologies and production from renewable sources, as they help to mitigate the tension between the energy demands and public concerns on environmental conservation [15]. Decarbonisation of energy systems is critical to accomplish the goals of green economy and energy security as well.

However, significant barriers to renewable energy market penetration still exist in the areas of cost competitiveness and technical advancement. So, vast improvements in energy and resource efficiency (for example through hybrid cycles) are needed before we can experience significant expansion of renewable electricity in both on-grid and off-grid systems.

Along with technological advancements, the policy makers need to expand thinking on approaches to facilitate the renewable energy market penetration, considering shifts in energy markets, political and economic situations. Pooling efforts can increase the odds of success at barrier removal worldwide, contribute to economic recovery, and create parallel collaboration pathways for industry, transportation, agriculture, forestry, waste, and water sectors.

Concentrated solar power (CSP) is one of the promising and rapidly expanding renewable energy technologies, owing to its features like wide availability, readiness for hybridization with conventional fuels and cost effectiveness. However, like other renewable energy sources solar energy is not only characterized by discontinuous availability but is also affected by random variations due to local weather conditions. In this scenario, the availability of energy storage is indispensable to overcome the intermittent energy supply and allowing a large number of solutions and combination of different technologies from already existing power generation systems [16].

1.2.3 CSP-Conventional Fuels Hybrid Systems

Hybridization with conventional fuels is one of the potential ways to overcome the intermittency of sunlight and thus increasing the CSP utilization in power generation. Hybrid power generation schemes can be grouped as follows:

1.2.3.1 Hybrid Solar Gas Turbines Systems (HSGT)

The solarized gas turbine systems use a CSP system to preheat the compressed air (to a high temperature—around 1070 K) before it enters the combustion chamber (Fig.1.5). Higher temperature of the compressed air results in reduction of the fuel consumption hence, reduction of exergy losses in the combustion chamber. Consequently, this integration scheme can yield higher efficiencies —up to 30% when utilizing solarized gas turbines in a combined cycle.

The most common and mature CSP technology for hybrid gas turbines is central receiver system or solar tower, which have been both modeled and built with different heat transfer fluids for the preheating process. The higher temperatures achievable with solar tower system makes it a more attractive option for hybridization, as the solar to electric efficiency would be higher; however, turbine modifications are required for steady operation [17]. Dynamic analysis have been performed to overcome the technical challenges and for optimization of solar hybridization schemes of gas turbines.

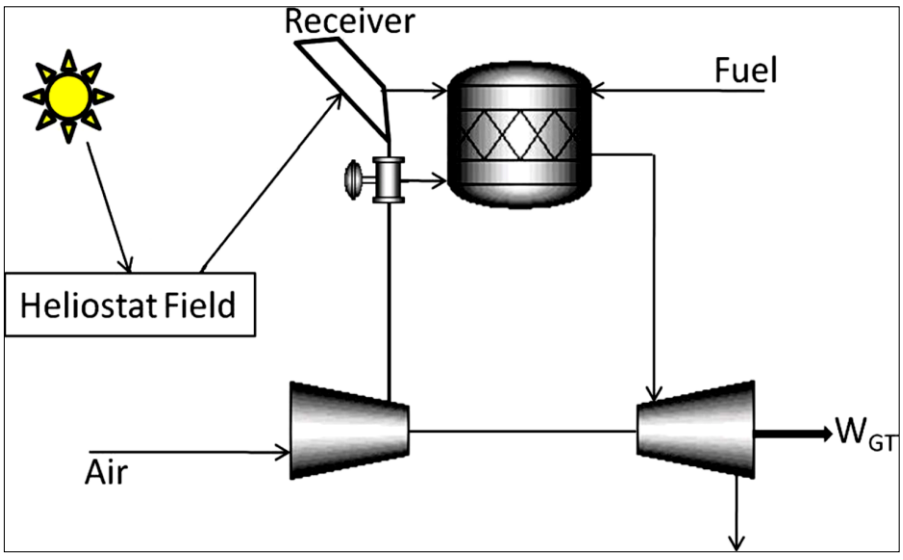

Figure 1-5 Example of hybrid solar–fossil fuel gas turbine [18]

1.2.3.2 Hybrid Combined Cycles

Hybrid solar–fossil fuel combined cycles have higher thermal efficiencies in comparison with either Brayton or Rankine cycles. Higher thermal efficiencies result in less receiver/heliostat area required for the same system size, and hence lower capital costs for the integration of the solar application. Solar energy is typically incorporated into a combined cycle in two configurations: in the top gas turbine cycle (similar to HSGT), or as supplemental solar heat to the bottoming Rankine cycle (Fig.1.6).

here are many different solar integration configurations for the bottoming cycle, and some of the most studied methods for this type of integration in literature include: preheating the steam, extracting steam from the HRSG for reheating, and increasing the flow rate of hot gas into the HRSG by supplementing the flue gas from the gas turbine with air heated by the solar application. A few hybrid solar–fossil fuel combined cycles are also currently being built in Egypt, Algeria, and Morocco [18, 19].

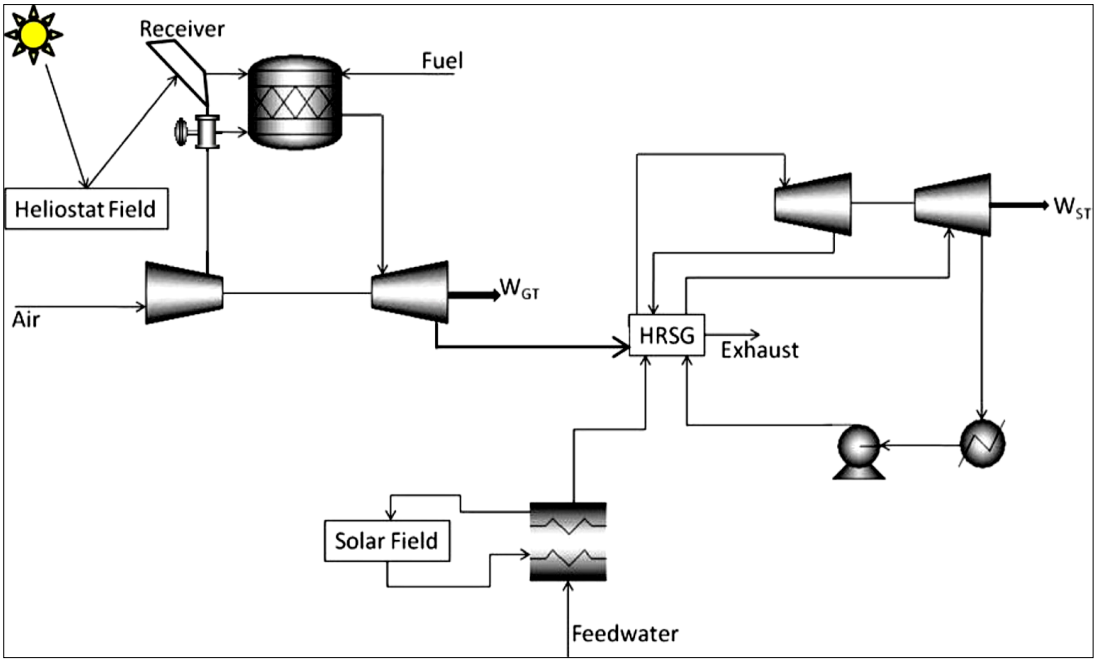

Figure 1-6 Possible solar integration methods in a combined cycle: solar heat can be added to the top cycle, the bottoming cycle (preheating the feed water), or both [18]

1.3 Thermal Energy Storage Integration in CSP Systems

One of the CSP strengths is the integration of thermal energy storage (TES) which not only reduces the mismatch between supply and demand by controlling the flow of intermittent energy supply but also improves the performance and reliability of the overall power plant. CSP systems combined with TES offer grid security by enabling such plants to supply dispatchable power. The energy storage could also be used to offset the temporary decreases of production from conventional energy sources, allowing a reduction of the peak and efficiency improvement which result in fuel savings [20]. Therefore, energy storage is a crucial factor to become the renewable energy a completely reliable source.

According to the principle of energy storage, thermal energy storage systems can be classified as sensible, latent and thermochemical heat storage (Fig.1.7). A brief overview of each storage system is presented below, while Chap.4 and Chap 5 will cover details of sensible and thermochemical heat storage systems, respectively.

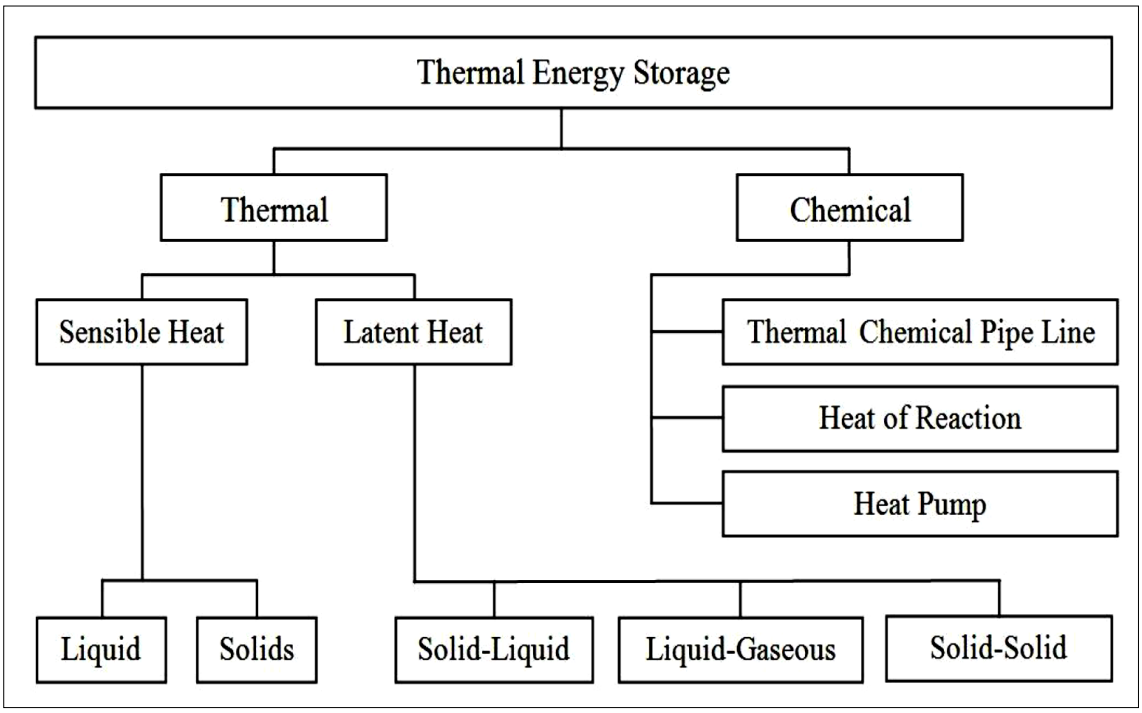

Figure 1-7 Methods of thermal energy storage

1.3.1 Sensible Heat Storage

In sensible heat storage systems (SHSS), thermal energy is stored by raising the temperature of a solid or liquid media, thus increasing its energy content. The sensible heat stored is dependent on heat capacity of the medium (C_p), mass of the storage material m as well as the temperature difference of the storage medium between its initial and final states ΔT. The amount of energy stored (Q) is given by the relation:

$$\mathbf{Q} = \int_{\mathbf{T_i}}^{\mathbf{T_f}} \mathbf{m}.\mathbf{C_p}.\Delta\mathbf{T} \qquad (1.1)$$

Where T_i and T_f are the initial and final temperature of the storage, respectively. Sensible heat storage is by far the most developed and common method for heat storage. Some common materials used for sensible heat storage include clay, concrete, aluminum, glass, water, etc [21].

1.3.2 Latent Heat Storage

Latent heat storage (LHS) is based on the heat absorption and release when a storage material undergoes phase change (e.g. melting, evaporating and crystallization) at a constant temperature. Based on the specific heat and the high enthalpy change, the latent heat storage can store 5–14 times more heat per unit volume than sensible heat storage materials such as water, masonry, or rock. . Phase change can occur in different forms: solid–solid, solid–liquid, solid–gas, and liquid–gas. Solid–liquid transitions are an economically attractive option for use in thermal energy storage systems. The storage capacity of the LHS system with a solid-liquid process is given by:

$$\mathbf{Q} = \mathbf{m}.\left[\int_{\mathbf{T_i}}^{\mathbf{T_m}} \mathbf{C_{p,s}}.\Delta\mathbf{T} + \boldsymbol{\lambda} + \int_{\mathbf{T_m}}^{\mathbf{T_f}} \mathbf{C_{p,l}}.\Delta\mathbf{T}\right] \qquad (1.2)$$

The first term of the second member is the sensible heat of the solid phase, λ represents the specific latent heat and, finally, the third term is the sensible heat of the liquid phase. $C_{p,}$ and $C_{p,}$ are specific heat of solid and liquid phase, respectively and Tm is the melting temperature of the material [21].

1.3.3 Thermochemical Heat Storage

Thermochemical heat storage involves the reversible chemical reactions where heat is stored during the endothermic reaction and released during the exothermic one. The thermochemical heat stored is linked to the reaction enthalpy. During the charging step, endothermic reaction takes place and thermal energy is used to dissociate a chemical reactant A into products B and C. During the discharging step, the products of the endothermic reaction (B and C) react to form the initial reactant (A), and this is exothermic reaction.

$$\mathbf{A} + \Delta\mathbf{H_r} \leftrightarrow \mathbf{B} + \mathbf{C} \tag{1.3}$$

The heat stored is given by:

$$\mathbf{Q} = \mathbf{a_r}.\,\mathbf{m}.\,\Delta\mathbf{H_r} \tag{1.4}$$

where a is the extent of conversion, m is the mass of storage material and ΔHr is the reaction enthalpy. Thermochemical heat storage systems store sensible as well as chemical energy, thus providing higher energy densities relative to latent and sensible TES. However, complexity and high cost limit the commercial applications of thermochemical energy storage systems, and they are still at development phase [22].

1.4 Objective and Scope of the Thesis

The preceding review on the importance of clean and efficient energy systems with particular focus on the concepts of: distributed generation, CHP systems and CSP hybrid gas turbines systems, have assessed the potential of TES technology for CSP hybrid systems. However, very few case studies featuring the TES in solar hybrid gas turbine systems particularly micro gas turbines (mGT) have been investigated so far. In order to achieve a better understanding of the behavior of TES coupled with solar hybrid gas turbine systems, a comprehensive analysis of both mGT cycle and TES should be undertaken. The present work intends to contribute towards this analysis. For this purpose, the present study is divided in two main parts: first section deals with TURBEC T100 modeling and fault diagnostics in the T100 cycle; the second part focuses on the dynamic analysis of TES system, which is part of the T100-based HSGT facility, developed at the University of Genova, followed by experimental validation of the developed models.

In addition to the sensible TES system, ThermoChemical Energy Storage (TCES) based on the redox cycle of Cobalt oxides has also been analyzed to provide insight and guidance for designing the real TCES system.

Overall this work aims to give as much as possible design parameters and performances analysis in order to pave the way for designing and optimization of the HSGT plants coupled with TES systems. However, this thesis is limited by the analysis of the complete HSGT system integrated with TES, as it analyzed the T100 cycle and TES systems independently. Hence, future work will involve merging the knowledge and modelling capabilities developed for mGT cycle and TES systems in this study to design a single simulation tool, which will be useful to analyze the performance, at design, off-design and transient conditions of the mGT-based CSP hybrid systems.

1.4.1 Thesis overview

This Thesis is structured in five main chapters and a concluding chapter subdivided in paragraphs for each topic. A brief description of each chapter is given as following:

Chapter 2: model development for steady-state simulation of T100 mGT within the collaboration between University of Genova (Unige) and Ansaldo Energia, validation against the reference models, tuning and model application in real operating conditions at the Ansaldo Energia test rig (AE-T100), is presented. Furthermore, diagnostic applications of the model for whole mGT cycle are discussed with the help of two case studies.

Chapter 3: This chapter is focused on diagnostics of Micro Humid Air Turbine (mHAT) system located at Vrije Universiteit Brussels (VUB), through the application of AE-T100 model. After the validation of modified AE-T100 model in real operating conditions of VUB-mHAT cycle, it has been used for monitoring the recuperator performance degradation, as first diagnostic application of the AE-T100 tool, in dry operation.

Chapter 4: Dynamic modeling and experimental validation of a TES system at laboratory scale, which is part of the hybrid solar gas turbine (HSGT) system developed at the University of Genova, is presented. TES is a sensible heat storage system, modeled using two

different approaches to study the thermal stratification inside TES during charging/discharging cycle: CFD model based on ANSYS-FLUENT code and a reduced-order model using transient simulation tool TRANSEO. The numerical results are compared with an experimental data in order to validate the accuracy of both models. Finally, modeling capability to present the state of charge (SoC) and thermal stratification of the storage, and scope of each model is discussed.

Chapter 5: The potential of ThermoChemical energy Storage (TCS) based on metallic oxides is discussed. Overall thermochemical process based on redox cycle of cobalt oxides Co3O4\Coo is modeled using the relations for the mass and energy conservation and reaction kinetics. This mathematical model is then used for the parametric study to optimize the storage parameters.

Chapter 6: The main conclusions and the possible future development of this research are discussed.

Bibliography

1. BP Statistical Review of World Energy, London, United Kingdom, June 2016.
2. International Energy Agency, Energy Balances of Non-OECD Countries, Paris, France, 2016.
3. Labat, A., Kitous, A., Perry, M., Saveyn, B., Vandyck, T., and Vrontisi, Z. 2015. GECO2015. Global Energy and Climate Outlook. Road to Paris. JRC Scientific and Policy Reports, EUR 27239 EN. JRC9589, ISBN 978-92-79-48233-5, ISSN 1831-9424, doi: 10.2791/198028.
4. Dempsey, J., Ewing, J., 2011. Germany, in reversal, will close nuclear plants by 2022. N.Y.Times.http://www.nytimes.com/2011/05/31/world/europe/31germany.html?_r=2&, last access 08/12/2017.
5. GCEC (2015). The Global Commission on the Economy and Climate - Milan Brahmbhatt (World Resources Institute) and Rajat Kathuria (ICRIER) - India: Pathways to Sustaining Rapid Development in a New Climate Economy. http://static.newclimateeconomy.report/wp-content/uploads/2014/11/India-pathways-to-newclimate-economy_conference-draft_web.pdf, last access 08/12/2017.
6. IEA: International Energy Agency, World Energy Outlook 2016, Paris, France, November 2016.
7. Panwar, N.L., Kaushik, S.C., Kothari, S., 2011. Role of renewable energy sources in environmental protection: A review. Renew. Sustain. Energy Rev. 15, 1513–1524. doi: http://dx.doi.org/10.1016/j.rser.2010.11.037, last access 05/12/2017
8. V.Giordano, S.Bossart, "Assessing Smart Grid Benefits and Impacts: EU and U.S. Initiatives Joint Report EC JRC – US DOE", 2012, European Commission, Joint Research Centre (JRC), Institute for Energy and Transport (IET).
9. IEA, "Technology Roadmap - Smart Grids", 2011.
10. EPRI (Electric Power Research Institute), 2011. "Estimating the Costs and Benefits of the Smart Grid - A Preliminary Estimate of the Investment Requirements and the Resultant Benefits of a Fully Functioning Smart Grid", EPRI report.
11. Auer, J., Berger, S., Just, T., 2008. Combined heat and power. A pillar of Germanys integrated energy and climate program (Research No. Current issue), Energy and Climate Change. Deutsche Bank Research, Germany.

12. Viral, D., Khatod, D.K., 2012. “Optimal planning of distributed generation systems in distribution system: A review”. Renewable and Sustainable Energy Reviews,16(7), pp: 5146-5165.

13. Ribarov, L. A., and Liscinsky, D. S., 2007. “Microgrid Viability for Small-Scale Cooling, Heating, and Power,” Journal of Energy Resources Technology, 129(1), pp. 71-78.

14. Fisher, S., 2004. “Assessing the Value of CHP Systems,” ASHRAE Journal, 46 (6), pp. 12-17.

15. Al-Badi, A.H., Albadi, M.H., 2012. Domestic solar water heating system in Oman: Current status and future prospects. Renew. Sustain. Energy Rev. 16, 5727–5731. doi :http://dx.doi.org/10.1016/j.rser.2012.06.007.

16. Gil A, Medrano M, Martorell I, Lázaro A, Dolado P, Zalba B and Cabeza L F 2010 State of the art on high temperature thermal energy storage for power generation. Part 1Concepts, materials and modellization Renew. Sustain. Energy Rev. 14 31–55.

17. Fisher, F., Sugarmen, C., Ring, A., Sinai, J., 2004. “Gas Turbine “Solarization”-Modifications for Solar/Fuel Hybrid Operation”. Journal of Solar Energy Engineering 126(3)·

18. Ahmad A. Eter, Esmail M. A. Mokheimer, Mohamed A. Habib, Amro Al-Qutub, 2012. “A Review of Hybrid Solar–Fossil Fuel Power Generation Systems and Performance Metrics”. Journal of Solar Energy Engineering, NOVEMBER 2012, Vol. 134.

19. Ugolini, D., Zachary, J., and Park, J., 2009, “Options for Hybrid Solar and Conventional Fossil Plants,” Bechtel Corporation, Technical Report.

20. Medrano M, Gil A, Martorell I, Potau X and Cabeza L F 2010 State of the art on high temperature thermal energy storage for power generation. Part 2—Case studies Renew. Sustain. Energy Rev. 14 56–72.

21. Dincer, I., and Rosen, M. A., 2002, Thermal Energy Storage: Systems and Applications, UK: Wiley.

22. Cabeza L F 2014 Advances in Thermal Energy Storage Systems_ Methods and Applications (Woodhead Publishing Series in Energy).

Section 1: AE-T100 Micro Gas Turbine Modeling

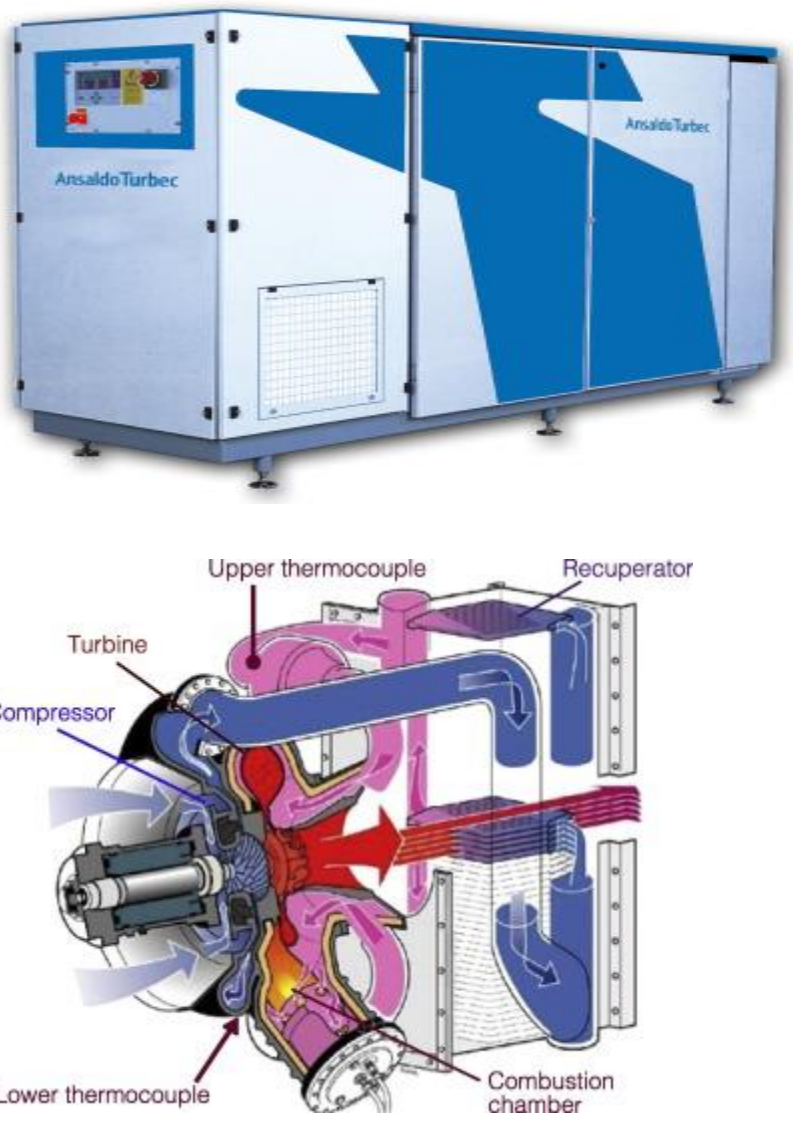

Figure 1-8 ANSALDO ENERGIA T100 test rig: Whole unit (top), inside view (bottom)

2 Micro Gas Turbine Modeling and Model Based Diagnostics

Scope of this chapter is to present the modeling of T100 mGT cycle, validation against the reference models, tuning and model application in real operating conditions at the Ansaldo Energia test rig (AE-T100). The validated model is used for fault diagnostics of the whole mGT cycle with the help of two case studies measured at AE-T100 test rig, to highlight the diagnostic capability of the AE-T100 tool.

In past few decades, fluctuating oil prices in global energy market, dwindling supply of conventional fuels and concerns about greenhouse gas emissions have led to the development of more efficient and clean energy systems. Hence, global electricity market is shifting towards more efficient energy production systems to cope with the stringent fuel supply, deregulated energy markets and also to mitigate the environmental deterioration caused by fossil fuel consumption [1].

In this scenario small-scale distributed generation (DG) systems are expected to play a vital role in present and future power infrastructure. From the viewpoint of economic feasibility, the costs of installing the generators and producing the electricity can be comparatively inexpensive using the DG systems. Furthermore, to improve the electrical or thermal efficiency through waste heat recovery, combined generation of heat and power (CHP) with small decentralized CHP plants is an emerging technology in the modern power industry [2,3].

2.1. Micro Gas Turbine: A Potential Power Generation Source in DG Systems

Micro gas turbines (mGT) are small gas turbines systems range from 30 to 400 kilowatts while conventional gas turbines range from 500 kW to more than 300 MW. They generally have lower electrical efficiencies in comparison with reciprocating engines of similar size. Without a recuperator the overall efficiency of a microturbine is 15 to 17%, whereas with an 85% effective recuperator the efficiency can be as high as 33 % [4]. They offer promising features like high rate of exhaust heat recovery in CHP mode, compact size, high fuel flexibility and low emissions levels. Additional features of lower maintenance requirement, higher reliability, reduced noise and vibration, and lower operational cost give mGTs an edge over the internal combustion engines [5]. Hence, micro gas turbine (mGT) is becoming an attractive power generation source in DG systems.

2.1.1 Basic Process of a mGT cycle

The basic components of an mGT system are: compressor, turbine, recuperator, high-speed generator and power electronics interfacing. Micro turbines, like large gas turbines operate based on the thermodynamic cycle i.e Brayton cycle. The process starts from the inlet air compression in a radial (centrifugal) compressor, which is then preheated in the recuperator using heat from the turbine exhaust. Heated air from the recuperator is mixed with fuel in the combustor and burned. The hot combustion gas is then expanded in the turbine, producing rotating mechanical power to drive the compressor and the electric generator, mounted on the same shaft (single-shaft design). Two-shaft models use one turbine to drive the compressor and a second turbine to drive the generator, with exhaust from the compressor turbine powering the generator turbine.

In a typical micro turbine air to gas heat exchanger called recuperator is added to increase the overall efficiency, which uses the heat energy available in the turbine's hot exhaust gas to preheat the compressed air before the compressed air goes into the combustion chamber thereby reducing the fuel needed during the combustion process. In single-shaft models, a single expansion turbine turns both the compressor and the generator, while two-shaft models use one turbine to drive the compressor and a second turbine to drive the generator, with

exhaust from the compressor turbine powering the generator turbine. The power turbine's exhaust is then used in the recuperator to preheat the air from the compressor. Figure 2.1 shows the schematic diagram of a single-shaft micro turbine based generation system.

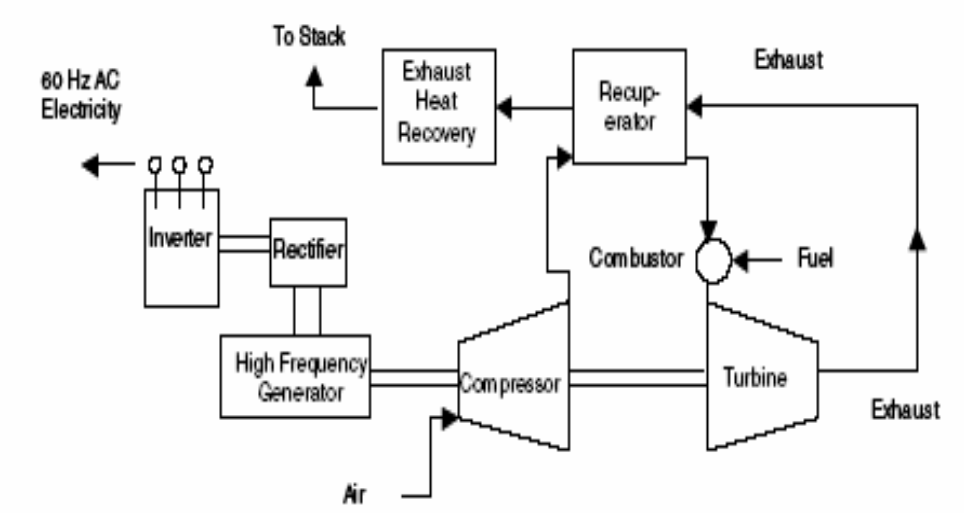

Figure 2-1 Micro turbine-based CHP system (single-shaft design)

Single-shaft micro turbines feature digital power controllers to convert the high frequency AC power produced by the generator into commercially usable electricity. This power conditioning involves rectifying the high frequency AC to DC and then inverting the DC to 60 Hz (or 50 Hz) AC. Power electronic interfacing is a critical component in the single-shaft design and is generally designed to handle transient and voltage spikes [6].

2.1.2 Numerical modelling of the mGT Systems- A short review

Due to the apparent penetration of mGT in modern power industry in past few decades, considerable research activities have been carried out particularly in the field of numerical modeling and simulation of mGT cycles, to have in-depth knowledge of machine functions and to overcome their scientific and engineering challenges. These mGT models can also be applied for novel system designing and optimizing the machine performance [11, 12].

The efficiency of mGTs can also be improved and their environmental impacts can be reduced further by the advanced systems. Zabihian et al. [8] have developed a steady-state model to evaluate the performance of a micro gas turbine fueled by the blends of biodiesel and petro-diesel. The concentration of inlet biodiesel to the model was 10%, 20%, and 30%.

The developed model was validated against the experimental data obtained from a micro gas turbine unit. The results indicate that most parameters like pressure, temperatures, and flow rates at various locations as well as output power, and ambient conditions are influenced, to some degree, by changes in the fuel composition. This indicates that although most mGTs can be potentially operated by a high concentration of biodiesel blends, before this fuel switching can be implemented, the system operational parameters should be evaluated by the system modeling to predict possible negative impacts of biodiesel in the inlet fuel on the engine.

Larosa et al. [9] have analyzed the dynamic behavior of a hybrid system emulator. This system developed by LG Fuel Cell Systems (LGFCS) consists of a recuperated micro gas turbine (mGT) coupled with a large volume, called "emulator" [Fig.2-2].

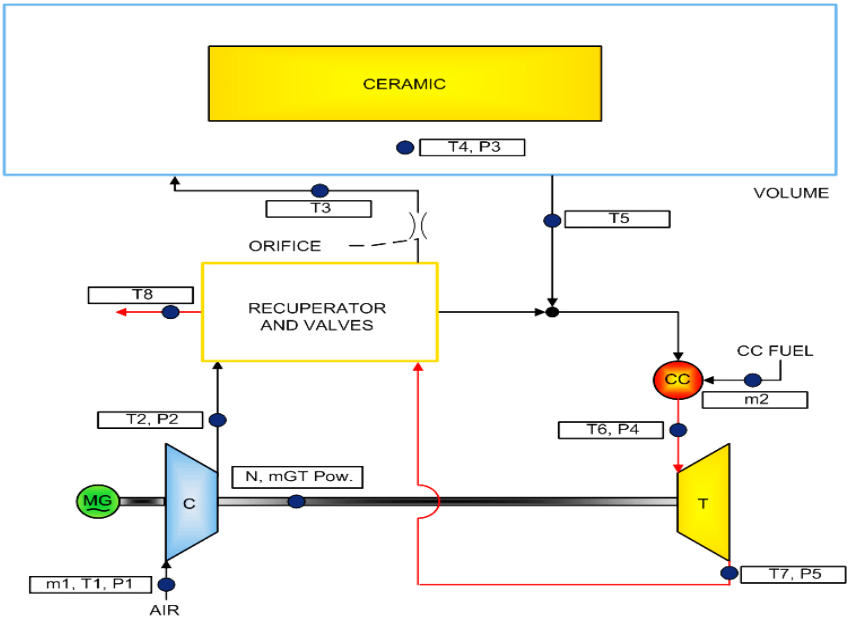

Figure 2-2. – Simplified LGFCS hybrid system emulator scheme [9]

The purpose of this emulator is to analyze the behavior of the mGT coupled with the vessel and to test the control strategies, before testing the full scale Fuel Cell –mGT hybrid system. The tests, carried out by LGFCS, aimed both at understanding the dynamic behavior of the system and validating the dynamic model based on the original simulation tool TRANSEO, which has been developed by The Thermochemical Power Group (TPG) at the University of Genoa in 2000s. TRANSEO has been used to build a physical and modular model of the LGFCS emulator system. The model was used to characterize the mGT

performance and identify the performance gap in the expander by upgrading and substituting the machine. Final results have validated that model is capable to predict the overall transient behavior of the system accurately.

Part load performance of a small scale (100 kWe) CHP plant based on a modified regenerative mGT, fired by natural gas (NG) and solid biomass to serve a residential energy demand, has been analyzed by Camporeale et al. [10]. In this cycle compressed air exiting from recuperator is externally heated by the hot gases produced in a biomass furnace; then the air is conveyed to combustion chamber which is fueled with NG. The hot gas expands in the turbine and then feeds the recuperator, while the biomass combustion flue gases are used for preheating the combustion air that feeds the furnace [Fig. 2-3].

Different biomass/NG energy input ratios are also modeled, in order to assess the trade-offs between: lower energy conversion efficiency and higher investment cost when increasing the biomass input rate, higher primary energy savings (PESs) and revenues from feed-in tariff available for biomass electricity fed into the grid. The results show that the variable rotational speed operation allows high the part load efficiency, mainly due to constant maximum cycle temperature.

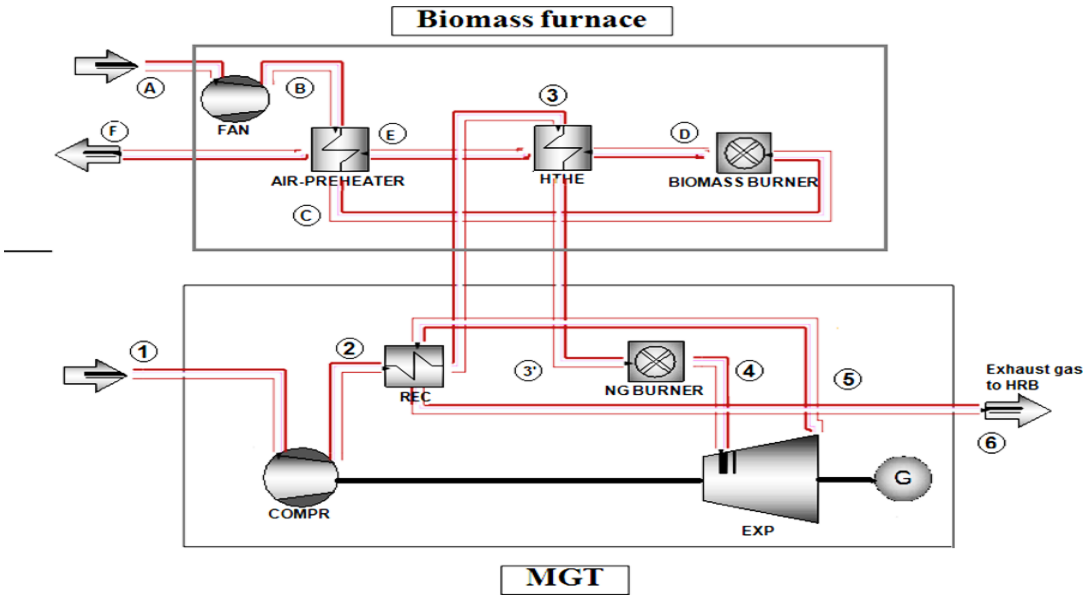

Figure 2-3 Natural gas-biomass duel fueled mGT system [10]

In order to further improve the performance of basic mGT cycles, future research will be highly focused on the concepts of novel systems and different fuel combinations. Reale et al. [7] have investigated the combustion efficiency and the gaseous emission of a 100 kWe mGT, designed for working with natural gas but fueled with hydrogen and methane blends. CFD results from the combustor analysis have been validated with experimental data. This analysis proved that addition of 10% of hydrogen to pure methane doesn't affect the behavior of the micro gas turbine either in terms of NO or CO emissions. From a practical point of view, the possibility of using fuels with a similar Wobbe index was also confirmed.

Lee et al. [13] have developed a simulation program for power generation gas turbines and its application to an IGCC gas turbine has also been explained. Due to its modular nature and both the stage-level and entire component-level models were adopted, the program can be easily extended to other applied cycles such as recuperated and reheated cycles. Influences of major system integration parameters on the operating conditions of the compressor and turbine as well as on engine performance were analyzed.

Sun et al. [14] have presented a steady-state numerical simulation of the entire gas turbine with wet compression in order to evaluate the effects on the gas turbine performance. Compared with the dry case, the results of wet cases demonstrated the increased values of the compression ratios, turbine expansion ratios, intake mass flow rates, and engine thrusts including decreased specific fuel consumption, and reduced NOx production in the combustor.

Guo et al. [15] have adopted the method of modularized modeling, creating an electro-mechanic simulation model for a Micro turbine Generation System (MTGS), including the micro-turbine, permanent magnetic synchronous generator, rectifier and inverter. In this paper, control strategy for grid-connected and islanding operations of a micro-turbine generation system is researched. Micro-turbine discussed in the paper is the single-shaft heavy duty one. The control system is made up of speed control, temperature control and acceleration control, as shown in Figure.2-4. A new control strategy to regulate the output power of MTGS based on the combination of decoupled control of output voltage and hysteresis current control is also introduced, and simulations results have proved the feasibility of the strategy.

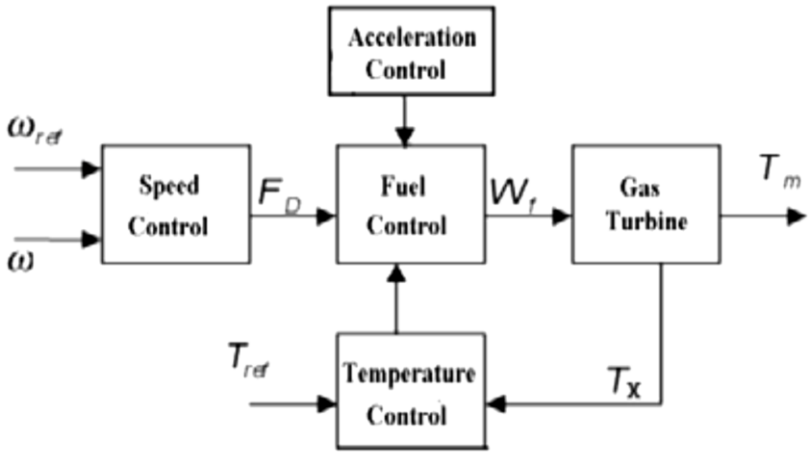

Figure 2-4. Microturbine control system architecture [15]

In the scenario where power generation using mGTs is getting more and more attention, externally fired micro-gas turbine (EFmGT) is preferred among small-scale distributed generators, mainly due to high fuel flexibility, high overall efficiency, environmental benefits, and low maintenance requirement. A typical EFmGT consists of compressor, recuperator, turbine, combustor, exhaust heat recovery boiler, high-speed generator, and power electronics to feed power to electrical loads (Fig.2-5).

The working principle of EFmGT is also based on the Brayton cycle similar to that of conventional large-scale gas turbines. However, the main difference lies in the combustor position: combustor is located after the turbine instead of before the turbine. As a result, recuperator is used for heat addition to the working fluid that is done by the combustor in a Brayton cycle. The heated air is then expanded through the turbine and mixed with the high-temperature combustion product from the combustor. After the mixer, the flue gas is then passed through the recuperator gas side.

Rahman et al. [16] have evaluated the performance of an EFmGT-based standalone poly-generation system with the help of a dynamic model. The proposed poly-generation system consists of EFMGT unit, electrical and thermal storage, and membrane distillation unit to fulfill the electricity, thermal, and drinking water demand of the user in a standalone mode [Fig.2-6]. The dynamic model is accomplished by integrating a thermodynamic model with a mechanical model of the rotor and a transfer function based control system model. The entire poly-generation system is modeled and simulated in Matlab/Simulink environment. The

developed model is suitable for analyzing the system performance particularly from thermodynamic and control point of view.

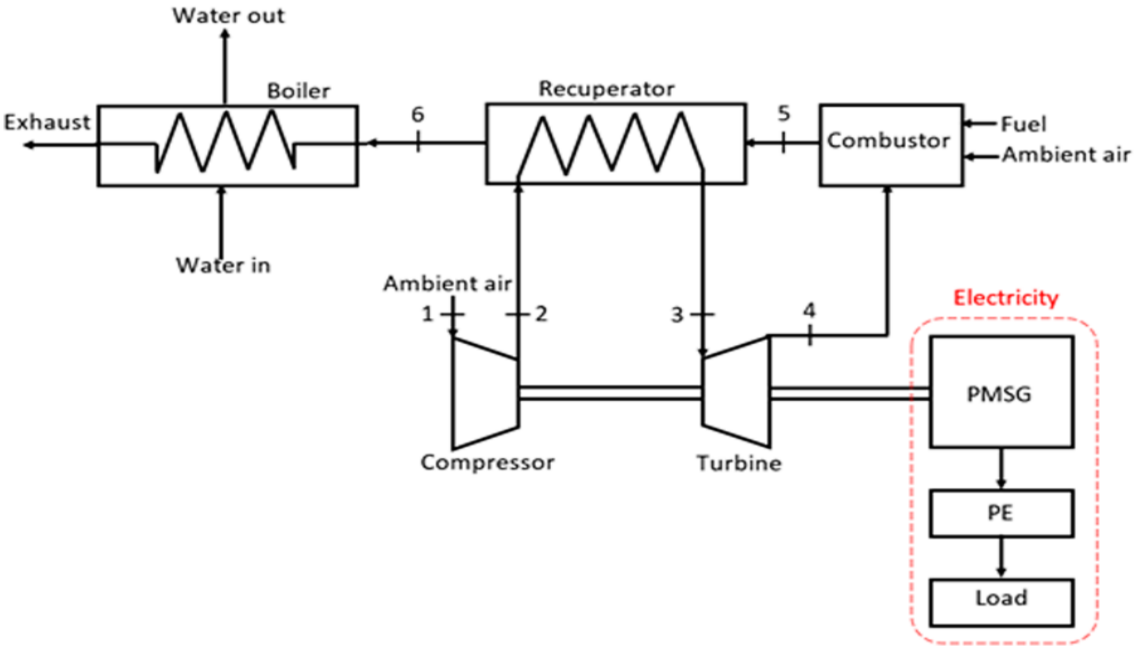

Figure 2-5. Externally fired microturbine CHP system [16]

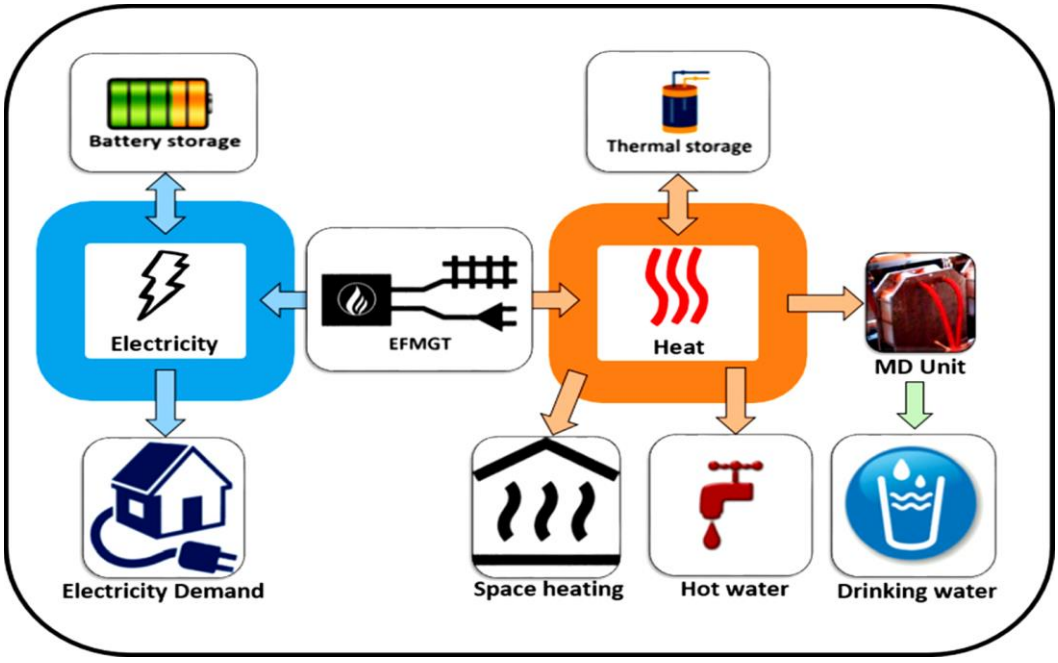

Figure 2-6. Block diagram of the poly-generation system based on EFMGT [16]

Traverso et al. [17] have presented the steady-state and transient performance obtained by an EFmGT demonstration plant, which is based on a recuperated 80 kW micro-gas turbine (Elliott TA-80R) integrated with the externally fired cycle. The schematic layout of the plant installed at the ARI (Ansaldo Ricerche) laboratories, is illustrated in Fig.2-7 with the main control valves. This work tested the feasibility of a control strategy for the externally fired gas turbines at laboratory scale, and assessed the off-design and dynamic behavior of the cycle. In addition to the experimental analysis, the TRANSEO model of the EFmGT has also been validated in off-design and transient conditions. This work provides good basis for the future improvement in the performance of EFmGT test rig and extending its application to larger size externally fired gas turbine cycles.

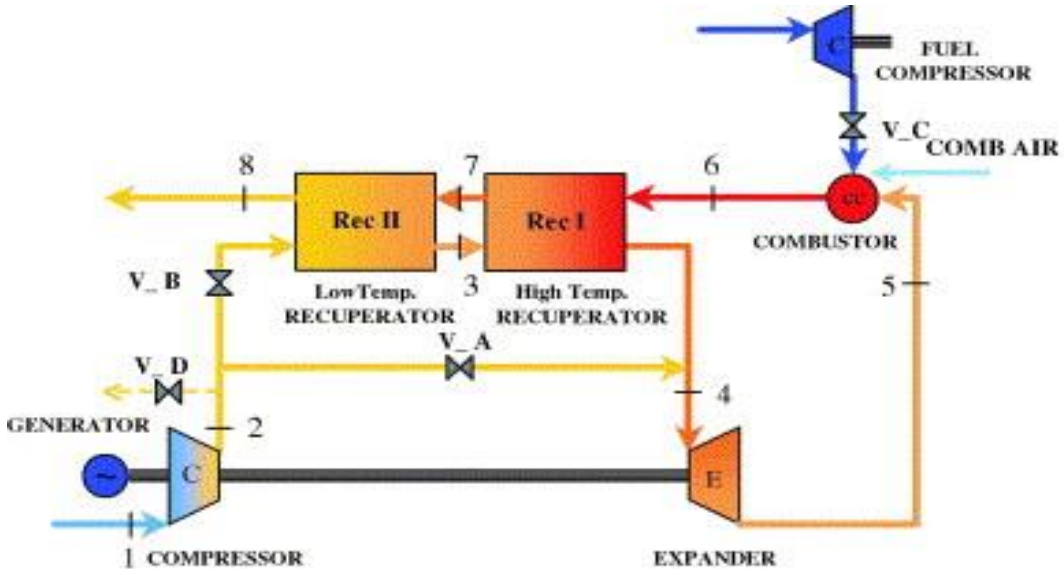

Figure 2-7. Schematics of the externally fired microturbine cycle (EFmGT) installed at the ARI laboratories [17]

Thermo-economic assessment of mGT (100 kWe) fed by natural gas (NG) and biomass has also been carried out by Traverso et al. [18]. The plant is based on a modified regenerative mGT, where compressed air exiting from recuperator is externally heated by the hot gases produced in a biomass furnace; then the air is conveyed to combustion chamber where a conventional internal combustion with NG takes place, reaching the maximum cycle temperature allowed by the turbine blades. This study has concluded that dual fuel mGT is an interesting option to increase the efficiency, flexibility, and plant reliability at low cost in

comparison to only biomass systems, as well as facilitating the integration of renewable and fossil fuel systems.

The Thermochemical Power Group (TPG) at the University of Genoa has also developed simulation tools like TRANSEO, for the performance simulation of mGT cycles. The TRANSEO code is apt for the transient and dynamic simulations of energy systems. Even if this software was specifically developed for analyzing mGT-based cycles, potentially, any cycle layout and size can be modeled. TRANSEO is based on MATLAB-Simulink environment, but it merely exploits the visual interface and time machine, retaining the management of several fundamental calculations outside, in original dynamic-link libraries. Several component models are ready to be used, just picking them up from a specific library, "TPG library", putting them into the cycle model and making the proper connections. Thus, the cycle is modularly defined by an ensemble of components, using a standard interface between subsequent components [18, 19].

Carrero et.al [20] have modeled the dynamic behavior of Turbec T100 machine, which has been modified into micro Humid Air Turbine mHAT (Fig.2-8), with the help of the TRANSEO tool. The model was successfully validated in the steady-state dry operation mode, with absolute errors for the main cycle parameters below 1.5%. In addition, the model results for transient operation are also in good agreement with the experimental data.

Thereafter, TRANSEO model has been used for the mHAT cycle in order to predict the effect of water injection on the performance of the unit. This study is aimed at modeling the dynamic behavior of such a complex system in order to protect the components during transient operation and simulating the cycle performance in case of load fluctuations. According to the results of the model, it is possible to vary the demanded power output during water injection tests without risk of surge and without modifying the controller of the T100 mHAT.

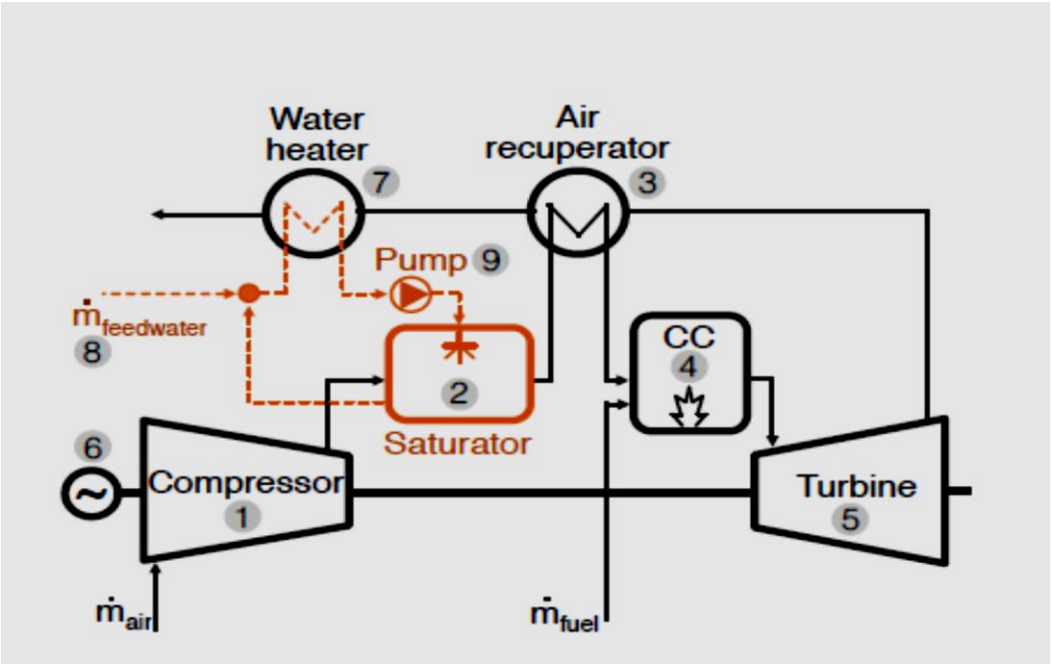

Figure 2-8 Layout of the mHAT installed at Vrije Universiteit Brussel(VUB).

Numerical simulation, off-design modeling and diagnostic tools are also essential for mGT cycle optimization and prediction of performance degradation. Monitoring and fault diagnostics tools reduce the overall operating and maintenance costs of the plant and increase the component and engine life [21]. AE-T100 model is a MATLAB simulation tool for steady state analysis for T100 cycle, which has been developed within collaboration between the TPG at the University of Genoa (Unige) and Ansaldo Energia.

The Ansaldo Energia T100 (AE-T100) mGT is a typical recuperated mGT manufactured by Turbec, assembled as a CHP unit: exhaust heat- due to the uncompleted conversion of all the energy to shaft power- is used to produce hot water by means of the exhaust gas heat-exchanger or economizer, while the shaft power is used to produce electricity. Hence, it works as a small cogeneration plant and produces 100 kW nominal power and around 150 kW in hot water. It is a recuperated turbine with an electrical efficiency around 33% (30% net), a firing level of 950°C and the pressure ratio of about 4.5:1.

Figure 2-9 describes the basic T100 cycle. The air is first compressed in a variable speed radial compressor (1-2). By preheating the compressed air in a recuperator using the hot exhaust gases (2-3), high efficiency can be achieved. The compressed air is heated further in

the combustion chamber (3-4) by burning the natural gas. The hot compressed air is then expanded over the turbine (4-5) to deliver the necessary power to drive the compressor. The remaining power on the shaft is converted into electrical power by a variable speed generator. After leaving the recuperator (5-6), the remaining heat in the exhaust gases is converted into thermal power by heating water for heating purpose through a heat exchanger (8-9).

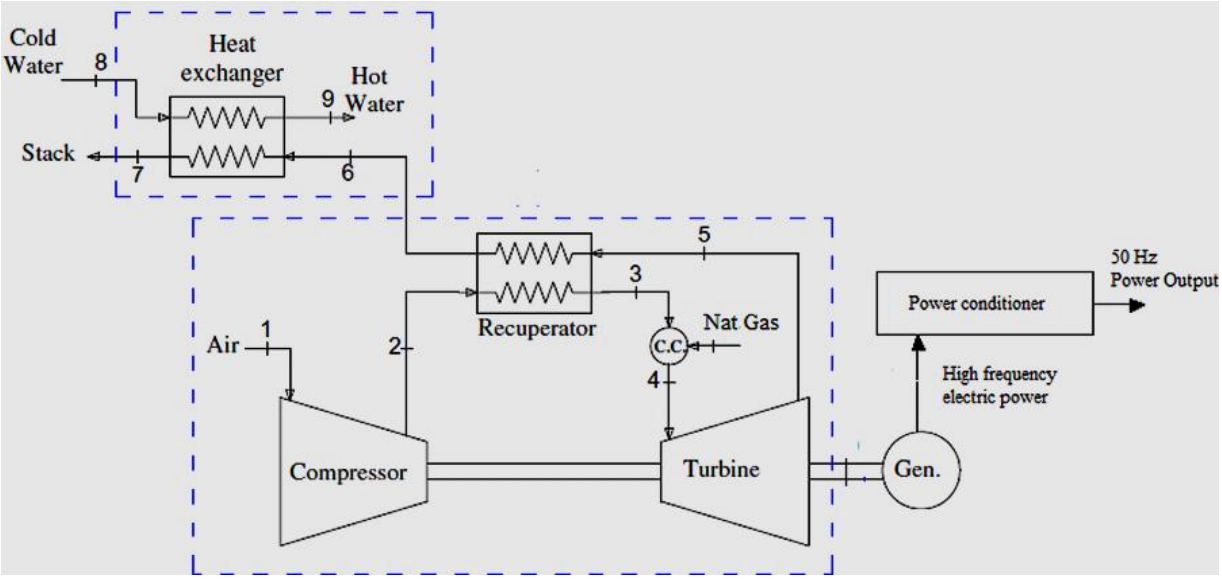

Figure 2-9.The T100 mGT cycle

Starting from a model available at Ansaldo Energia, for steady state simulation of mGT T100 cycles based on user requirements, a new more comprehensive simulation tool AE-T100 has been developed [22]. The following sections of this chapter are dedicated to the AE-T100 model development, model verification against a reference model Dynamic System Analyzer (DSA), sensitivity analysis, tuning, first phase of validation through the Ansaldo Energia test rig AE-T100 and diagnostic applications of the model.

2.2 Model Development for Ansaldo Energia Test Rig (AE-T100)

2.2.1 Brief Overview of the BT-100 Model

BT-100 is a steady state simulation tool for the T100 cycle, available at Ansaldo Energia [21]. It is based on the Dynamic System Analyzer (DSA) model. This DSA tool which has been originally developed by VOLVO, provides the design conditions according to the operating point of the real machine, which is different from the ISO conditions. Thermodynamic equations for each component in the BT-100 model are solved in the MATLAB environment, based on the design conditions and inputs provided by the user through Graphical User Interface (GUI) (Annex-1).

The BT-100 program uses a sub program to decide state properties of the working fluid in the turbine cycle. The program is called state.m and it is constructed by Magnus Genrup and Ivan Carlsson at Lund University. Straight forward mathematical solution for the equations in mGT cycle is not possible due to complex behavior of some component relations. Hence, matrix solver technique based on the Newton-Raphson theory is used inside the MATLAB code.

The iterative process starts with the initial guesses of the variables, with these guesses the gas turbine can be fully determined, and calculated values throughout the gas turbine are achieved. The calculated values are then compared with their respective guesses to check the error. This loop is continued until the defined criterion of the Root Mean Square Error (RMSE) is satisfied. Mainly the program calculates total pressure, total temperature, total enthalpy and mass flow on all the prominent points of the T100 cycle indicated in Figure 2-10.

The thermodynamic equations for each component in the T100 cycle, way of calculation and characteristic maps of the turbine and compressor cannot be shown here explicitly due to the confidentiality. From the GUI of BT-100 model user can define the inlet conditions, shaft speed, fuel parameters and TOT/TIT for the machine. The results are presented in this window in the form of graphical plots and tables for thermodynamic parameters like mass flow, pressure and temperature, and turbine and compressor maps are also shown to indicate

the operating point (Annex 2, 3). Fig. 2-11 shows the basic BT-100 model layout; components and flow numbers correspond to the model calculations inside the code.

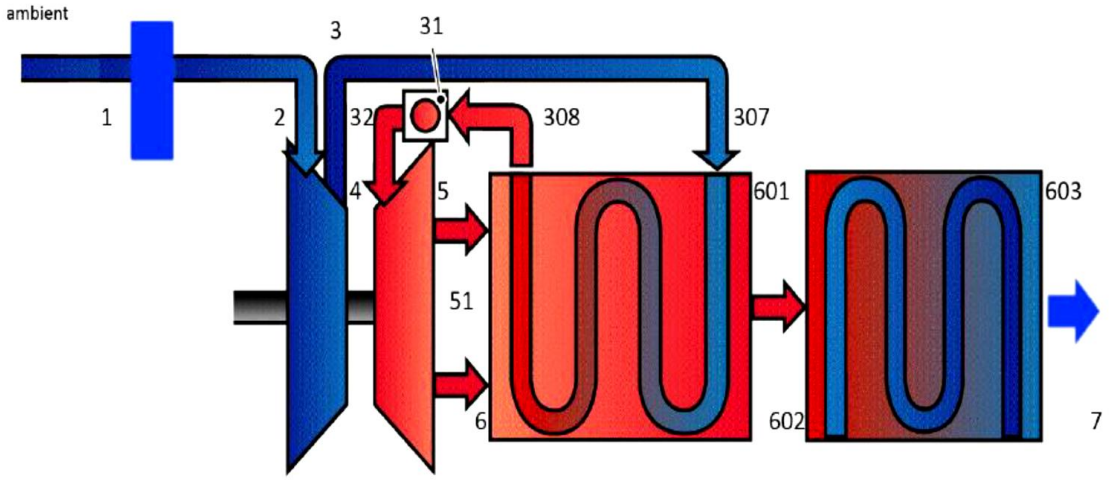

Figure 2-10.T100 cycle with station numbering throughout the turbine.

The AE-T100 model development, as explained in the following section, involved upgrading of the basic BT-100 model to make it a more comprehensive and detailed simulation tool.

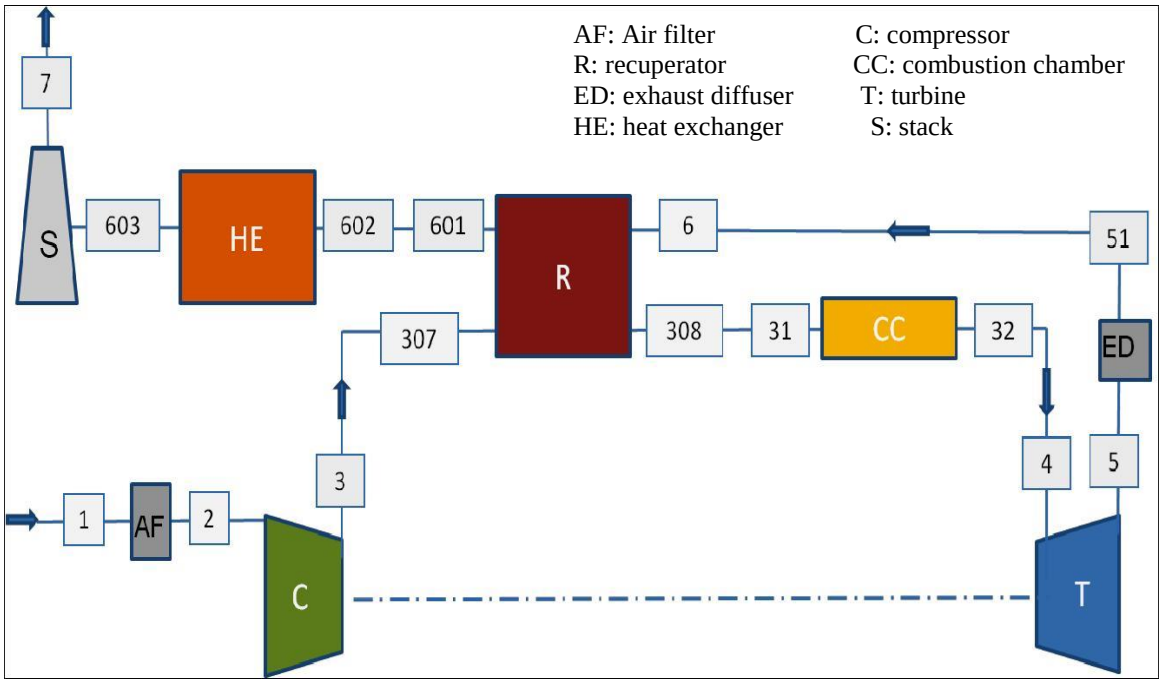

Figure 2-11 BT-100 model layout

2.2.2 New Components and Leakage Modelling

The existing model available at Ansaldo Energia BT-100 was a simplified version of the reference model DSA, and was not able to provide a detailed description of each leakage flow. The main aim of this work was the modeling of missing leakage points as well as power electronics details with respect to the existing model BT-100. So, an extensive thermodynamic analysis of both existing and reference models has been carried out to understand how to integrate new components like mixers, ducts and splitters in the existing model.

2.2.2.1 Mixers

Gas mixers in mGT cycle mix gas streams from different sources to produce a homogenous mixture that is fed to the following component. From mass conservation the mass outflow is the sum of inlet streams, while from energy conservation the enthalpy of outflow stream is the weighted average of inflow streams:

$$h_{out} = \frac{m_{in,1} . h_{in,1} + m_{in,2} . h_{in,2}}{m_{out}} \quad (2.1)$$

No pressure drop is assumed over the gas mixer. A total of five mixers have been added in the upgraded model.

2.2.2.2 Splitters

Splitters in mGT cycle split the inlet streams to leaks, bleed or main stream discharge to the next component. Total four splitters are being used in the upgraded model. From mass conservation the inlet mass flow to the splitter is the sum of all outlet flows. Thermodynamic characteristics like temperature and pressure of all leaks are same as of inlet stream to the splitter. A total of four splitters have been added in the upgrade model.

2.2.2.3 Ducts/pipes

In addition to the air inlet duct, there are five more ducts being simulated in the new model. These ducts just transmit the gas streams from one component to another in turbine cycle. Temperature and mass flow of inlet streams are not affected, but small pressure loss

occurs due to the fluid friction against the duct walls. The pressure drop depends on the inlet conditions and empirical coefficients which have been derived from the design case, where all the variables are known, including the pressure drop.

Figure 2-12shows the new upgraded model AE-T100 layout; components and flow numbers correspond to the model calculations in the code, while blue and red color indicate the cold and hot streams, respectively.

Legend
S: splitter
D: duct
M: mixer
ED: exhaust diffuser
HE: heat exchanger
G: generator
BU: burner
C: compressor
T: turbine
S: stack
R: recuperator

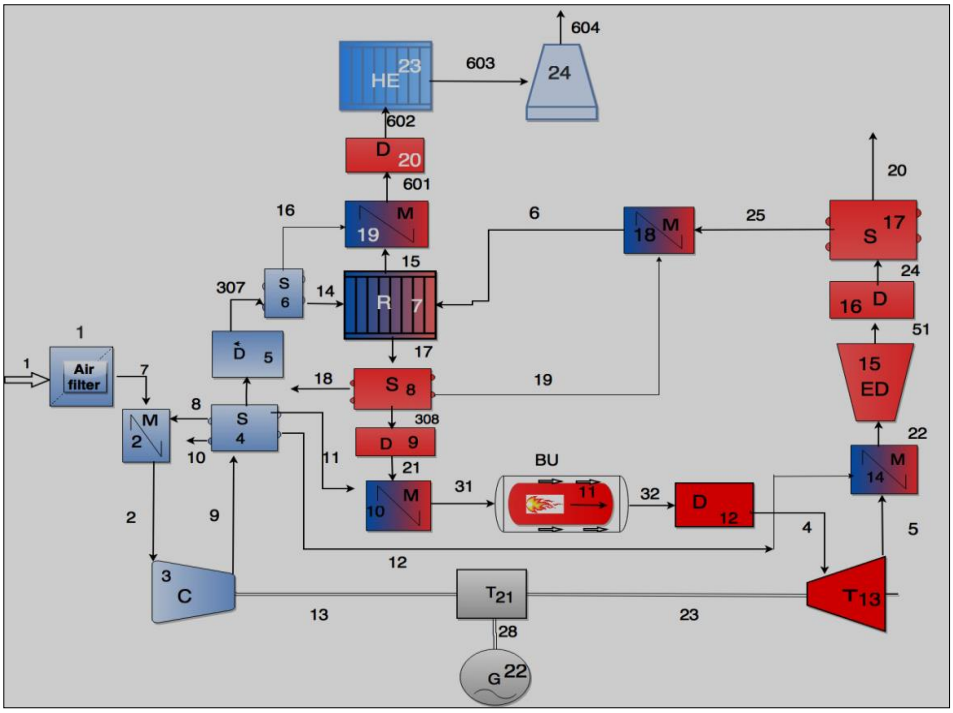

Figure 2-12. AE-T100 model layout: legend on the left shows the component symbols

The existing model lacks some leakage points, so the additional leaks have been considered in the new model and some have been omitted to match exactly the air flow paths of the reference model. Table 2-1 shows the comparison among the existing and new leakage points. (The leak numbers correspond to the numbers of air flow paths shown in the respective model layouts, Figure 2-11and 2-12).

Table 2.1 Comparison among leakages in existing model BT-100 and new model AE-T100

BT-100 Model		**AE-T100 Model**	
Not considered		Leak8	Leakage from compressor outlet to inlet for recirculation with incoming air stream
Bleed	Leak flow from the bleed point in the compressor to ambient	Leak10	Leak flow from the bleed point in the compressor to ambient
Not considered		Leak11	Leakage from compressor outlet to combustor inlet
Not considered		Leak12	Leakage from compressor outlet for turbine cooling
Leak307	Leakage at compressor discharge and recuperator inlet to the ambient	Leak16	Leakage at compressor discharge and recuperator inlet to the ambient
Leak31	Leakage at recuperator outlet and combustor inlet to ambient	Leak18	Leakage at recuperator outlet and combustor inlet to ambient
Leak4	Leakage at combustor outlet and turbine inlet to ambient	This has been considered in leak 18	
Not considered		Leak19	Leakage from recuperator cold outlet for recirculation
Leak6	Leakage at turbine exit to the ambient	Leak20	Leakage at turbine exit to the ambient
Leak602	Leakage at heat exchanger inlet to ambient	Not considered in order to match the reference case	
Leak7	Leakage at additional heat exchanger and stack to ambient	Not considered in order to match the reference case	

2.2.3 Power Electronics Implementation

The existing model has been extended by including the power electronics scheme. Thus, AE-T100 model takes into account the power consumption from auxiliary components like fans, pumps, bearings, switch board, etc. and also the power losses in inverter and generator. The following flow chart (Fig.2-13) illustrates the breakdown of power electronics scheme that has been applied in the new model.

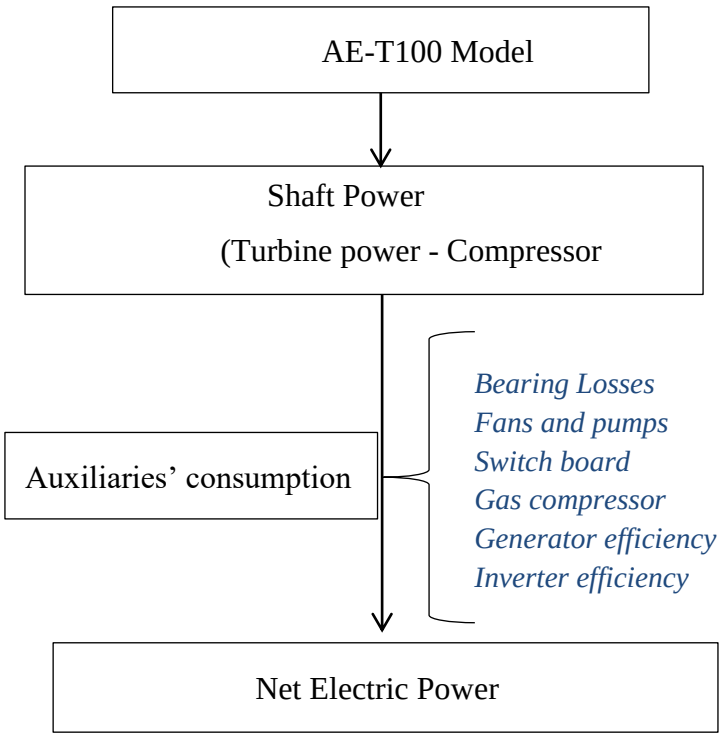

Figure 2-13 Power electronics scheme in AE-T100 model

2.2.4 Features of the new AE-T100 Model

Overall, the resulting model AE-T100 considers every minor leak/ bleed and provides more user flexibility. This modified model incorporates features of both models BT-100 and DSA model. Complete features of new model are summarized below:

- More user friendly interface: parameters like pressure drop across the air filter, heat exchanger and stack pressure are added in the GUI.
- More detailed mathematical approach (more residuals to estimate the new variables) to model new leakages and components

- Additional components like mixers, ducts and splitters to model more leakage points/path flows.
- Power electronics has been improved considering all the auxiliary equipment and power consumptions.
- Sensitivity analysis option in the GUI allows the user to analyze the effect of ambient and operating conditions on overall performance of the mGT.

2.3 AE-T100 Model Validation

The developed model AE-T100 has been verified against the reference DSA model. The verification process is based on the comparison among DSA and the new model results, at different shaft speeds. ISO conditions about ambient have been considered, TOT has been set to 645 °C and a fuel 50% methane and 50% ethane has been used, to be consistent with the original DSA model assumptions. Power is modified by changing the rotational speed at constant TOT.

Table 2.2 Simulation conditions for comparison between DSA and AE-T100 model

T_{amb}	**15 °C**
P_{amb}	**1.013 bar**
TOT	**645 °C**
Fuel	**Standard fuel (50% methane and 50% ethane, LHV: 47.2 MJ/kg)**

The parameter chosen for the validation is the average relative percent error ($\overline{e_{rel}}$)of various parameters like pressure, temperature and mass flow in the whole mGT cycle, with respect to the DSA values, as shown in Eq. 2.2

$$\overline{e_{rel}} = \frac{1}{N}\sum_{i=1}^{N}\left(\frac{x_{i,DSA}-x_{i,AE-T100}}{x_{DSA}}\right)\times 100 \qquad (2.2)$$

where N is the total number of comparison points in the whole mGT cycle, and $x_{i,,DSA}$ and $x_{i,AE\text{-}T100}$ denote the DSA and AE-T100 model results of a parameter x, respectively, at point i in the cycle. The relative percent error of the pressure, temperature and mass flow calculated by the above relation at different shaft speeds, is reported in Table 2.3.

Table 2.3 Comparison of AE-T100 model results with DSA results

Speed [rpm]	Average relative error [%]		
	Pressures	Temperatures	Mass flow rates
50000	0.12	0.21	0.06
55000	0.03	0.31	0.07
60000	0.13	0.34	0.08
65000	0.07	0.23	0.06
67500	0.01	0.25	0.03
70000	0.05	0.27	0.09

As evident from the above results, average percentage error of all the parameters with respect to the DSA results, is globally less than 0.5%. Thus, this comparison against the reference model verifies the new AE-T100 model, and proves its result quality.

2.4 Sensitivity Analysis

Sensitivity analysis in numerical steady-state simulations is an important feature to understand and optimize the mGT cycles [24]. The new AE-T100 model incorporates such a feature, to analyze the impact of ambient and operating conditions like temperature, pressure drop, speed, leakages, etc. on overall performance of the mGT cycle. This feature has been added in the GUI of AE-T100 model.

In general, the ambient conditions like inlet air temperature greatly influence the net power output and efficiency of the gas turbines. Higher temperature leads to reduced air mass flow rate (density of the air declines as temperature rises), which results in reduced power output. Net efficiency is also reduced by increasing the inlet air temperature; as compressor requires more power to compress the hot air [25]. The effect of variation in the ambient temperature on net electric power and net efficiency of the T100 cycle has been presented and quantified here (Fig.2-14 and Fig.2-15).

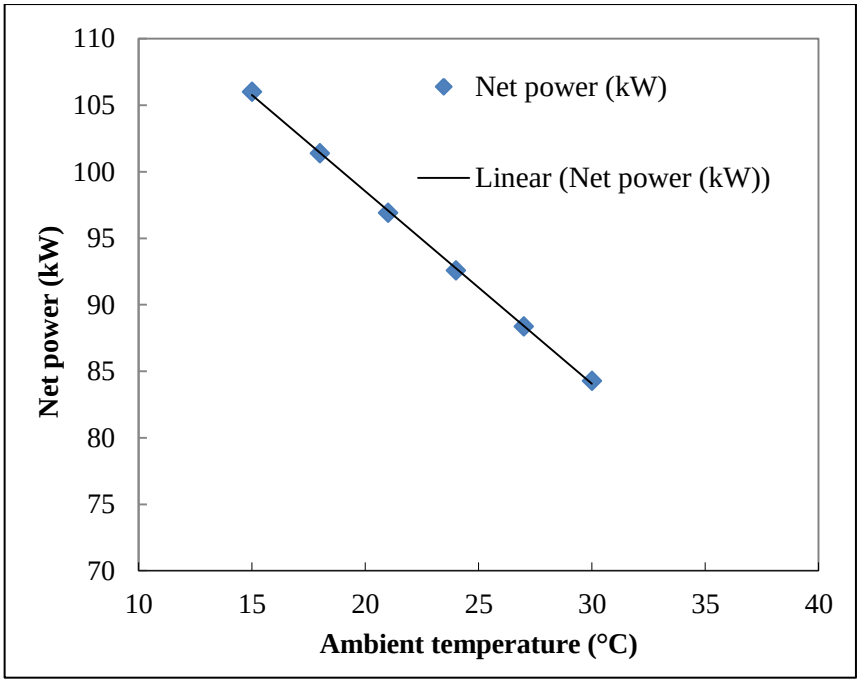

Figure 2-14 variation of net power with ambient temperature

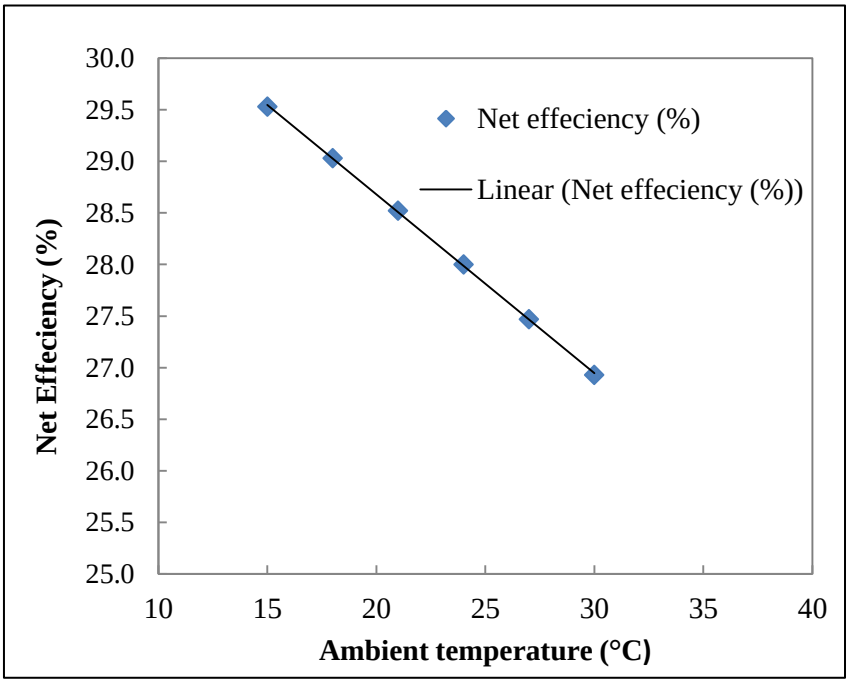

Figure 2-15 Variation of net efficiency with ambient temperature

These results show that increase in ambient temperature has more significant impact on net power: 1% decrease in net power and about 0.1 % decrease in net efficiency per each °C rise in the ambient temperature. All the simulations have been carried out at constant TOT and nominal turbine speed (100%).

The feature of sensitivity analysis has also been utilized to analyze the impact of different leakages on T100 performance (Fig 2-16).

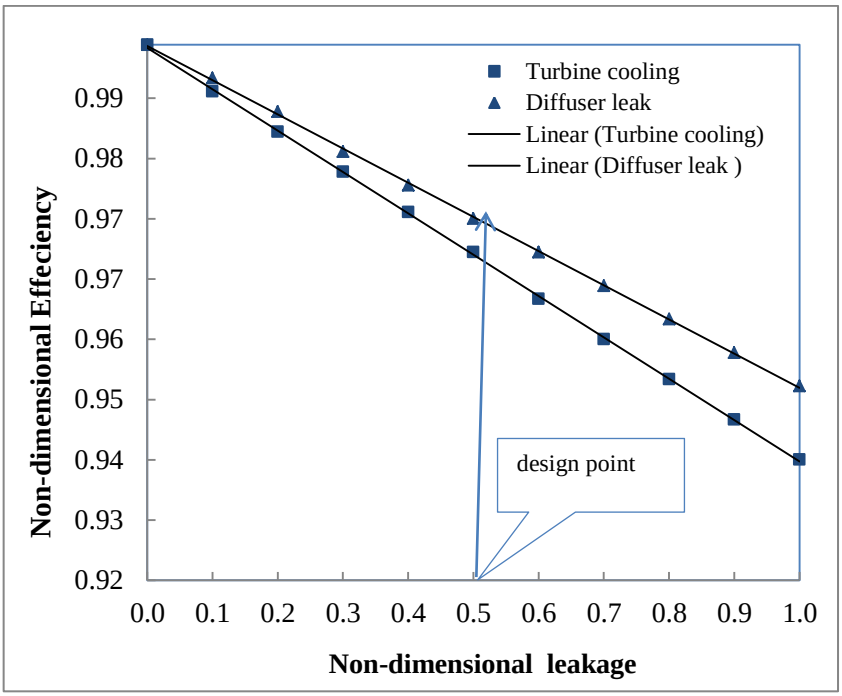

Figure 2-16 Variation of non-dimensional efficiency with non-dimensional leakage

In general all leakages like compressor bleed, turbine cooling and diffuser leak influence the mGT efficiency: as they reduce the flux entering the combustion chamber and turbine. But the impact of turbine cooling and diffuser leak is most significant. Fig. 2-16 illustrates the variation of net efficiency with these leakages. All the leakage values have been reported in non-dimensional form, since actual values cannot be mentioned due to confidentiality. Non-dimensional leakage is the actual leak against the upper leak bound (reference case). And non-dimensional efficiency is the actual efficiency against the ideal efficiency (when all leaks are assumed to be zero).

2.5 Model Based Diagnostics in Real Operating Conditions

The numerical modeling assumes the ideal performance of whole system, referring to initial or non-degraded mGT. Thus in order to model the real machine functioning, the developed model requires proper tuning at those specific operating conditions. Therefore, model tuning of AE-T100 corresponding to real operating conditions is the first step for diagnostics of the mGT cycle. Fig. 2-17 represents the process flow for model based diagnostics. The parameters involved in the tuning are mainly the recuperator design effectiveness and marginally the leakage values.

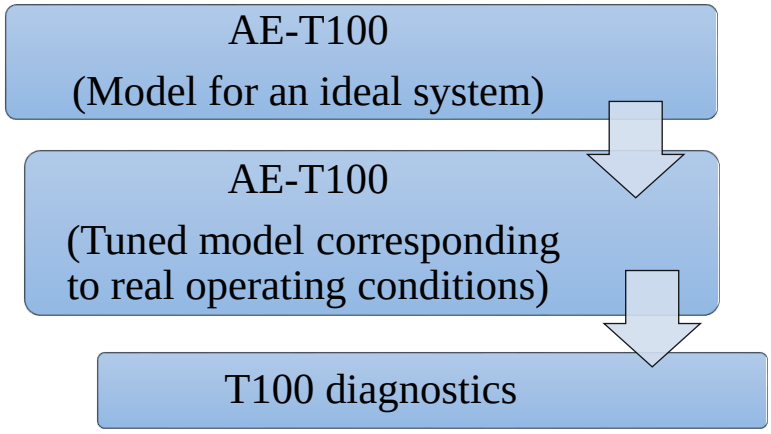

Figure 2-17 Process flow for model based diagnostics

2.5.1 Experimental Conditions

Field data has been obtained from AE-T100 test rig, installed at Ansaldo Energia. The mGT performance has been assessed for different power levels, starting from 102 kW (nominal power) to 60 kW and then back to 95 kW. The first power decrease has been from nominal power to 100 kW, then 10 kW steps have been used. Due to machine instability at 60 kW, the output power was set to 65 kW after few minutes, and then from 70 kW same trend was followed with increment of 10 kW till 90 kW. In the last step the power was set to 95 kW instead of 100 kW. The two tests at 100 kW operating conditions have been carried out with two different ambient temperatures: 20°C and 25°C, respectively. Measuring instruments used in the actual test are mentioned in Table 2-4.

Important parameters of investigation include absolute pressure, net power, differential pressure and temperature at different nodes of the machine (parameters are mentioned in Table 2-5). The experimental data have been acquired under stable operating conditions of the machine, considering the recuperator cold outlet temperature as the stability indicator. Figure 2-18 represents the load variation over the entire experiment, with ambient temperature varying from 20^{o}C at the start in morning, to 25^{o}C till the end of experiment in the afternoon.

Table 2.4 Instruments specifications

Parameter	Instrument	Range	Uncertainty
Temperature	RTD PT100 Class AEN60751	-200 to 600°C	0.1% F.S.
	T class 1EN60584	-40 to 350°C	
	J class 1 EN60584	-40 to 750°C	
Absolute pressure	SITRANS P DS III	0.16-16 bar	0.075% F.S.
Differential pressure	SITRANS P DS III	2.5-250 mbar	0.075% F.S.

2.5.2 Steady-State Functioning

Steady-state operation of mGT is defined based on the stability of recuperator cold outlet temperature. Every time the power is set to another value, the stability conditions for all the thermodynamic parameters involved are obtained when the recuperator cold outlet temperature is at steady-state. Fig.2-19 shows the recuperator cold outlet temperature variation with time, during the power shift from 100 kW to 90 kW. The initial temperature corresponding to 100 kW was 583 °C. After a transition of almost one minute, the stability of the recuperator cold outlet temperature is reached after 4-5 minutes from the power variation. The final temperature corresponding to 90 kW was 579.5 °C.

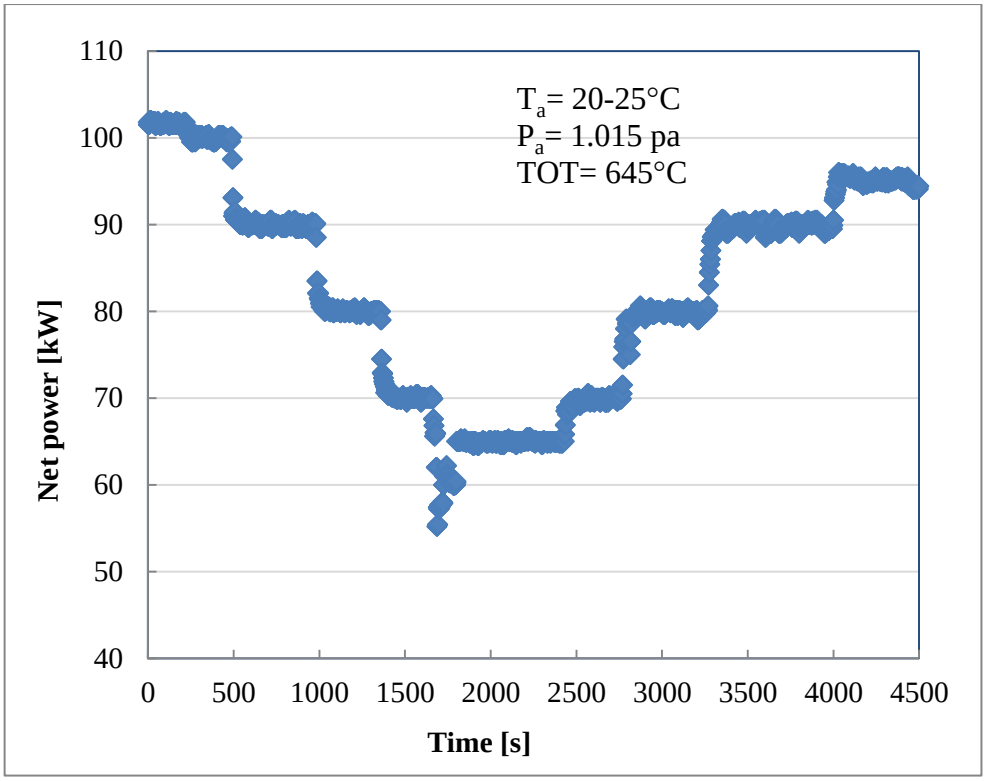

Figure 2-18 Variation of net electrical power with time during the experiment at AE-T100 test rig

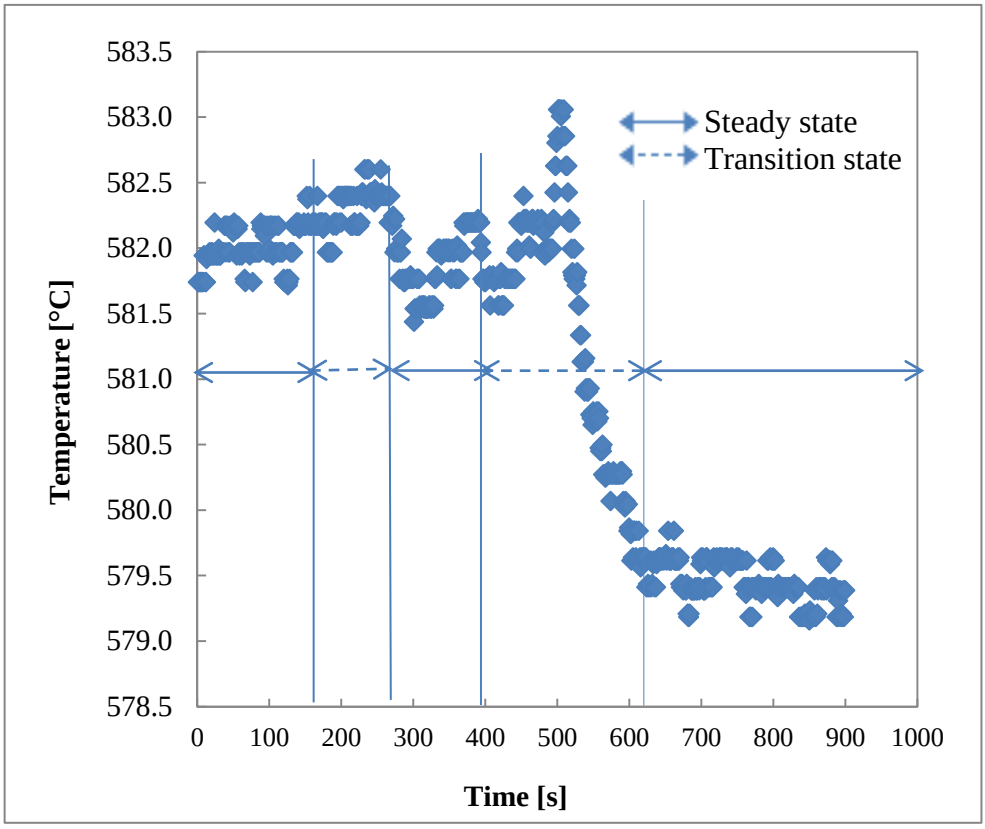

Figure 2-19Variation of recuperator cold outlet temperature with time during the experiment at AE-T100 test rig

2.5.3 AE-T100 Model Tuning

The numerical modeling assumes ideal performance of the whole system, referring to the initial or non-degraded mGT. Due to experimental activities over time, machine performance degrades, and so the design conditions also change. After a certain time period, the machine performs on a different set of design conditions than initial ones. In order to model the real machine functioning, the AE-T100 model requires proper tuning of the design parameters at the specific operating conditions, to get the corresponding off-design conditions. Therefore, model tuning is the first step for real time application of the AE-T100 tool.

For this study, the AE-T100 model has been tuned according to the field data obtained from AE-T100 test rig under steady state conditions, at different power levels. Model tuning is aimed at estimating the recuperator effectiveness for different loads, so that the whole model simulates the actual machine performance, with the minimum percentage error of all the thermodynamic parameters. Thus tuning is based on mainly the recuperator design effectiveness and marginally the leakage values. And if the model has to be applied for another machine, the tuning process needs to be repeated. The relative percentage error $e_{rel,i}$ of tuned model results with respect to the experimental ones is calculated according to Eq. 2.3.

$$e_{rel,i} = \frac{(x_{field,i} - x_{tuned,i})}{x_{field,i}} \times 100 \qquad (2.3)$$

Where $x_{tuned,i}$ denotes the tuned model value, and $x_{field,i}$ denotes the actual field value of the ith parameter. Table 2-5 shows the results of comparison among the tuned model values and experimental values of certain parameters in the mGT cycle.

Table 2.5 Comparison of tuned model values with experimental values at 100 kW

Parameter	Field value	Tuned model value	Relative percent error (%)
Compressor outlet pressure (barg).	3.37	3.32	1.48
Recuperator cold side outlet pressure (barg).	3.30	3.25	1.51
Turbine outlet pressure (barg)	0.05	0.05	0
Pressure drop over the recuperator cold side (bar)	0.06	0.06	0
Pressure Drop Over The Recuperator Hot Side (bar)	0.06	0.06	0
Recuperator Hot Outlet Temperature (°C)	285.43	290.87	-1.90
Air Temperature After Air Filter (°C)	20.54	20.41	0.63
Air Temperature At Compressor Inlet (°C)	23.12	20.60	10.90*
Recuperator Cold Inlet Temperature (°C)	214.47	212.34	0.99
Air Temperature At Combustor Inlet (°C)	581.56	581.75	-0.03
Net Electric Power (kW)	100	99.52	0.48

*Since the measurement is taken inside the test rig, it is affected by high temperature of machine surroundings. Thus, measured value of air temperature at compressor inlet is always higher than the simulated value.

As previously mentioned, parameters involved in the tuning are mainly the recuperator design effectiveness and marginally the leakage values. Hence, as a result of model tuning at different power levels, the actual/off-design recuperator effectiveness has been estimated,

which depends on the actual and design mass flow through the recuperator (m_{in} and $m_{in,des}$,respectively) and design effectiveness

$$\eta_{rec} = 1 - \left[\frac{m_{in}}{m_{in,des}}\right] \times \left[1 - \eta_{rec,des}\right] \qquad (2.4)$$

Recuperator design effectiveness $\eta_{rec,des}$ value is provided by the supplier or calculated through design data of temperatures of hot and cold streams. The actual/off-design recuperator effectiveness is decreasing with increasing net power (Fig. 2-20), since at higher power levels the mass flow through the recuperator also increases which results in low temperature out. The results are presented in the form of non-dimensional recuperator effectiveness:

$$\eta^*_{rec} = \frac{\eta_{rec}}{\eta_{rec,des}} \qquad (2.5)$$

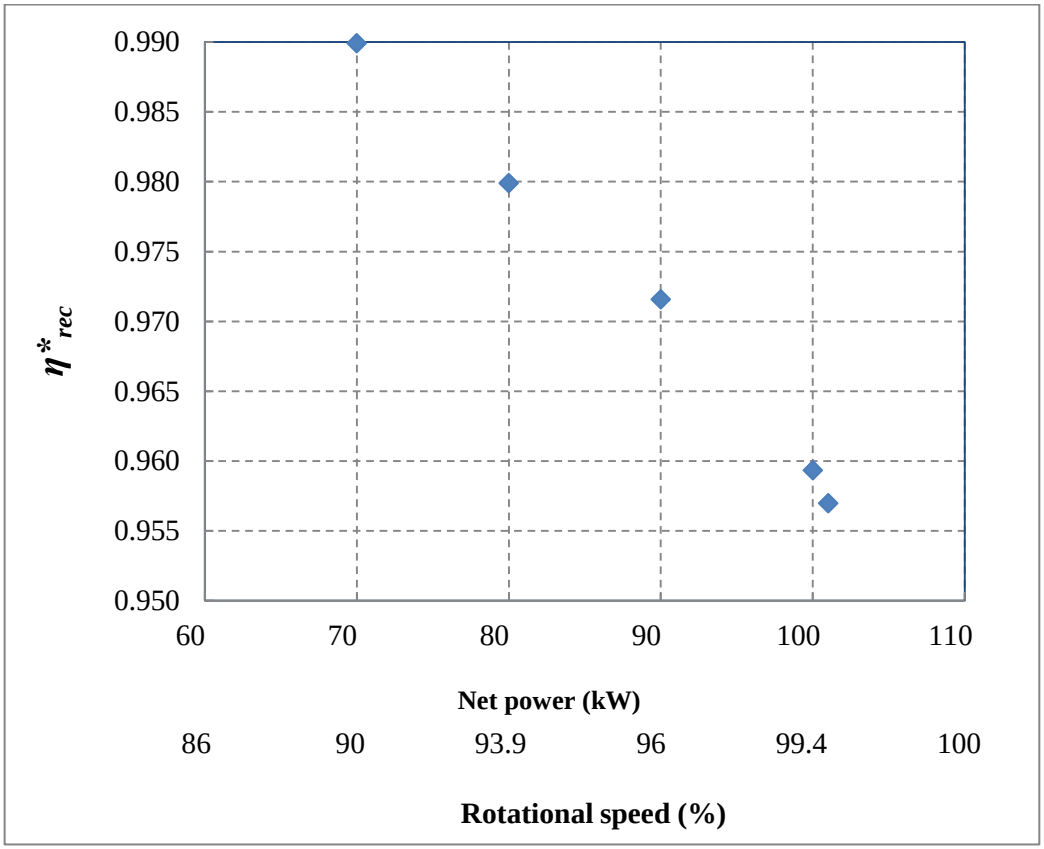

Figure 2-20 Non-dimensional recuperator effectiveness trend at different loads

2.5.4 Diagnostics Application of AE-T100 Model: Case Study 1

After the tuning according to real operating conditions, AE-T100 model has been used for diagnostic aims of the whole mGT cycle. To carry out this activity, the tuned model was applied to a special AE-T100 mGT equipped with an on-purpose damaged recuperator (Details about the recuperator damage cannot be explained here explicitly due to confidentiality). The comparison of the simulation results with field data (calculated by Eq.2.3) highlighted a high deviation in the pressure drop over the recuperator hot side and recuperator hot outlet temperature at different power levels, as shown in Table 2-6.

Table 2.6 Comparison of simulated recuperator performance with filed data

Net power (kW)	Pressure drop across the recuperator hot side	Recuperator hot outlet temperature
	Relative error [%]	Relative error [%]
100	66.7	-2.2
90	60.4	-0.2
80	62	1.2
70	63.6	2.7

The high deviations of model results from the field data, particularly in pressure drop across the recuperator hot side, indicate the performance degradation of the recuperator in the test rig. Hence, this case study gives the evidence that the AE-T100 model can be successfully applied for the mGT diagnostics.

2.6 Diagnostics Application of AE-T100 Model: Case Study 2

After the AE-T100 model development, tuning, first phase of validation through the Ansaldo Enegia test rig (AE-T100) and diagnostic application of the model, the following section deals with further utilization of the diagnostic capability of the AE-T100 model for mGT cycles.

This involves the model tuning through real operating conditions of a test (test 1) at AET100 test rig, followed by model application for the diagnostic aim of an unexpected machine behavior during another test (test 2), which was conducted after some time at the same test rig. The model results justified the diagnostic capability of the AE-T100 tool. Afterwards, based on the experimental observation of some problem in the burner in the same test rig, AE-T100 model was also applied to model its impact on the machine performance. Finally, the compressor map analysis of the experiment conducted on the same test rig after the leakage repair, and its comparison with the previous test has been explained in [26].

2.6.1 AE-T100 Model Tuning

As mentioned previously, model tuning corresponding to real operating conditions is the first step for diagnostics of the mGT cycle. Hence, AE-T100 model has been tuned according to the operating conditions of the test 1, which was carried out at the AE-T100 test rig and experimental data was acquired under stable operation of the machine. Experimental conditions for the test 1 are presented in Table 2-7.

Table 2.7 Operating conditions of test 1 at AE-T100 test rig

Parameter	Experimental value
Ambient pressure (bar)	1.015
Ambient relative humidity (%)	53
Inlet temperature (^{o}C)	23.5
Inlet pressure drop (mbar)	4.60
TOT (^{o}C)	645
LHV (MJ/kg)	46.44

Similar to the previous case, the parameters involved in the tuning are mainly the recuperator design effectiveness and, marginally, the leakage values. Table 2- 8 presents the results of the comparison among the tuned model and experimental values in terms of relative percentage error, which has been calculated according to Eq.2.3.

Table 2.8 Comparison of tuned model values with experimental values of test 1

Parameter	**Experimental value**	**Tuned model value**	**Relative percent error (%)**
Compressor outlet temperature (^{o}C)	219.49	219.59	-0.04
Compressor outlet pressure (barg)	3.33	3.28	1.32
Recuperator air outlet temperature (^{o}C)	589.36	588.44	0.15
Recuperator air outlet pressure (barg)	3.26	3.17	2.75
Recuperator air side pressure losses (mbar)	67.48	66.35	1.66
Net electrical power (kW)	102.61	101.56	1.01
Net efficiency (%)	29.30	29.50	-0.66
Fuel flow rate (g/s)	7.54	7.50	0.53

Since the relative percent error between the model results and field data is less than 3% globally, this proves that AE-T100 model can simulate the actual machine performance of AE-T100 test rig with reasonable accuracy.

2.6.2 Fault Detection in AE-T100 Test Rig - Model Application

Another test (test 2) was conducted after some time at the same test rig AE-T100. During this test, unexpected low performance was observed, so the AE-T100 model was applied in these operating conditions for the diagnostic purpose. Experimental conditions for the test 2 are presented in Table 2-9.

Table 2.9 Operating conditions of test 2 at AE-T100 test rig

Parameter	Experimental value
Ambient pressure (bar)	1.023
Ambient relative humidity (%)	74
Inlet temperature (^{o}C)	17.2
Inlet pressure drop (mbar)	4.97
TOT (^{o}C)	645
LHV (MJ/kg)	46.44

The results of comparison between tuned model and experimental values in terms of relative percentage error calculated according to Eq.2.3 are presented in Table 2-10.

Table 2.10 Comparison of tuned model values with experimental values of test 2

Parameter	Experimental value	Tuned model value	Relative Percent error (%)
Compressor outlet temperature (^{o}C)	215.87	214.04	0.84
Compressor outlet pressure (barg)	3.39	3.41	-0.60
Recuperator air outlet temperature (^{o}C)	585.81	586.12	-0.05

Recuperator air outlet pressure (barg)	3.33	3.32	0.30
Recuperator air side pressure losses (mbar)	67.72	68.45	-1.08
Net electrical power (kW)	106.20	105.15	0.99
Net efficiency (%)	27.50	30.1	-9.45
Fuel flow rate (g/s)	8.35	7.51	10.06

It is evident from the above comparison that model simulation has resulted in high deviation in terms of net efficiency and fuel flow. We can observe that the tool estimated 9.45% higher efficiency than the one evaluated from test data and the fuel flow from experimental test was 10% higher than the one estimated with the tool. Based on these deviations in fuel flow and net efficiency, we can understand that machine performance is not normal and this behavior is also captured by the AE-T100 model. Hence, it justified the diagnostic capability of the AE-T100 tool.

2.6.3 Fault Detection in AE-T100 Test Rig - Experimental Observation

Afterwards, the physical examination of the AE-T100 test rig by Ansaldo Energia personnel has discovered the presence of some holes at the combustor inlet. Due to lot of past tests conducted on the same machine, volute ovalization at the combustor inlet began to appear and hence, the volute was not perfectly joined with the combustor. So, it was suspected that these crevices at the volute-combustor joint are responsible for some bypass leakage from the combustor. This leak can have following impacts:

- The bypass leakage can reduce the airflow entering the primary zone of the combustor or equivalently there is more secondary air (this can also be explained by a short description of the combustion chamber in the following section).
- This leakage may cause local hot spots or pollutant emissions; however, it was assumed that it should marginally affect the cycle performance, because the mGT is controlled based on TOT, which should not vary significantly. On the other hand, performance may vary mainly because of different combustor pressure losses.

AE-T100 model was used to verify these assumptions about the leakage impact.

2.6.4 Bypass Leakage Modelling - Sensitivity Analysis with AE-T100 Model

Based on the experimental observation of bypass leakage from the combustor inlet, we tried to model this phenomenon with the help of following parameters and carried out the sensitivity analysis using AE-T100 tool. The variations between simulation results and experimental data ($e_{rel,i}$) of test 2 have been presented in terms of RMS error:

- RMS-1for variations in different thermodynamic parameters of machine performance and
- RMS-2 for variations in net electric power and efficiency.

The thermodynamic parameters considered for RMS-1include: compressor outlet temperature and pressure, recuperator outlet temperature and pressure (cold side) and fuel flow rate. General formula for RMS error is shown by Eq 2.6.

$$RMS = \sqrt{\frac{\sum_{i=1}^{N}(e_{rel,i})^2}{N}} \qquad (2.6)$$

Where N is total number of parameters

All the results of sensitivity analysis in the following section will follow this pattern.

2.6.4.1 Air split ratio

The combustion chamber is the part of the mGT where one inserts the energy, liquid or gasified fuel is injected to the stream of hot air that recently left the recuperator and the composition ignites with the help of a spark plug (Fig.2-20). The chamber is designed for a premixed flame; fuel and air is mixed at almost stoichiometric conditions and then sprayed into the chamber were it is combusted. The velocity of the fuel/air mix is higher than the flame propagation front and it makes the flame "hoover" at a certain length from the injector.

A premixed flame burns with a lean mixture, this condition makes it delicate and quite easy to extinguish. To prevent this to happen, so-called flame out, there is a smaller diffusion flame called pilot flame that constantly burns in the bottom of the combustion chamber. A diffusion flame always burns with stoichiometric mixture somewhere and this makes it more stable than a premixed flame. There is much more air entering the combustion chamber than required to make a stoichiometric mixture, therefore the air is split into two directions; one part to be mixed with fuel (red arrows in Fig.2-21), and the other part through dilution holes to cool the newly combusted mixture (blue arrows in Fig.2-21). The ratio between these two air flows is called Air split (AS).

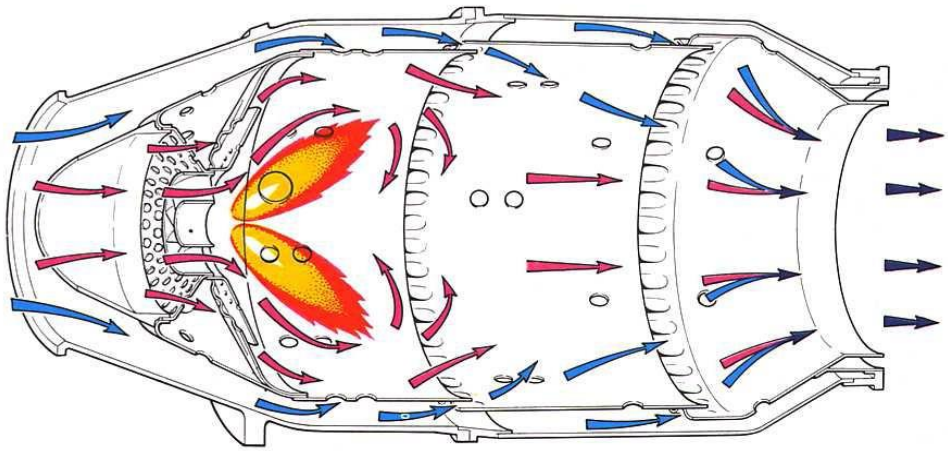

Figure 2-21. Air flow through the combustion chamber

For thermodynamic view, the combustion chamber is seen like a box where power from the air and the fuel enters and a mass flow of combustion gases leave at a much higher power. In the chamber the inlet air is divided into two directions with the variable AS: it is defined as the fraction of air that goes to the combustion zone (primary zone).

Hence, a leak at the combustor inlet, which was the case of AE-T100 test rig under study, can affect the stoichiometric ratio of the primary and secondary air, which in turn has an impact on the combustion efficiency and overall machine performance. In order to verify this supposition, simulations were carried out with decreasing values of AS ratio from the standard value, in the AE-T100 model. Figure.2-22 shows the result of sensitivity analysis with AS ratio. It is evident that both RMS errors for all the simulation results with different AS ratio are high, which indicates high deviations from the experimental data, and errors remain constant with varying AS ratio. Hence, variation in AS parameter cannot model the actual impact of this leakage on the machine performance, which we have experienced in test 2.

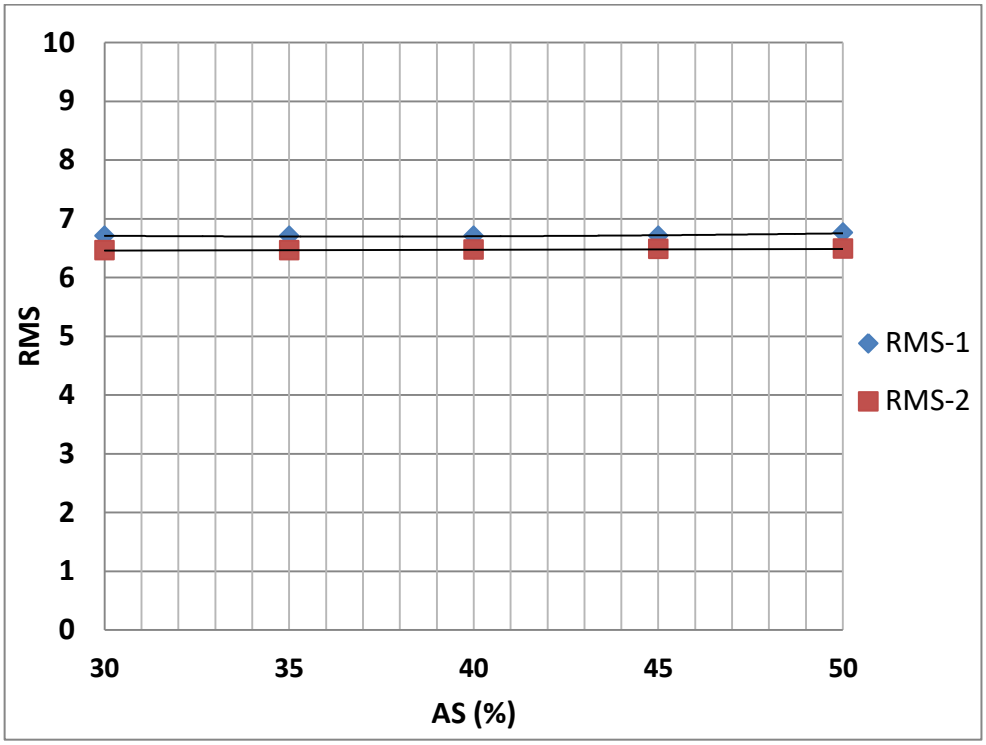

Figure 2-22 Sensitivity analysis with AS ratio

2.6.4.2 Leak to the ambient

In order to model the bypass leakage from combustor inlet, a leakage fraction from the recuperator cold outlet to the ambient was simulated in the AE-T100 model. Results of sensitivity analysis with different leak fractions are presented in Fig.2-23. Similar to the case with AS ratio, high RMS values for all the leakage fractions specify that this leakage modeling is not able to provide results close to the experimental data of test 2.

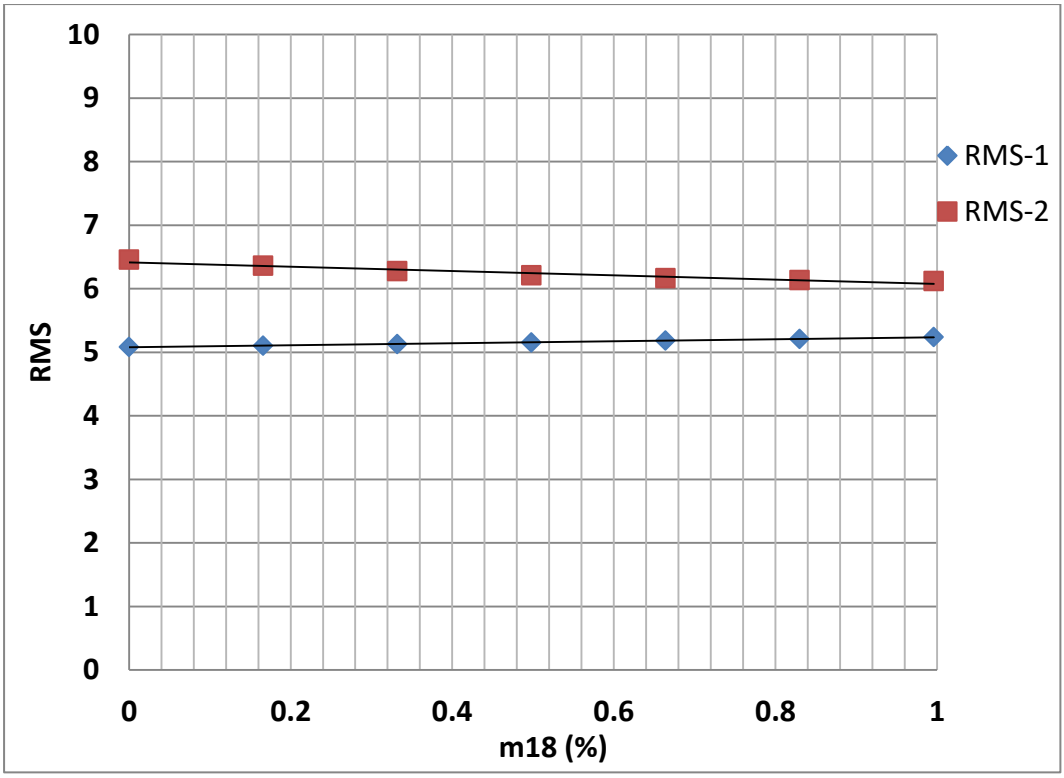

Figure 2-23 Sensitivity analysis with leak from recuperator cold outlet to the ambient

2.6.4.3 Pressure drop across the combustor

The pressure drop over the combustion chamber occurs due to the narrow passages and fluid heat increases as the compressed air travels between the housing and the flame tube it absorbs heat from the tube i.e. cools it down. Since the bypass leak from the combustor inlet reduces the air fraction entering the combustion chamber, which in turn can affect the pressure drop across the combustor. Thus, simulations were carried out changing the combustor pressure drop by a factor from the design value in the AE-T100 model (Fig. 2-24).

It is evident from Fig.2-24 that RMS error for net power and efficiency between simulation and experimental results (RMS-2) decreases with increase in combustor pressure drop, while RMS error for thermodynamic parameters (RMS-1) shows the opposite behavior. However, still high deviation of all the parameters from the experimental data verifies that change in combustor pressure drop cannot model the actual machine behavior in case of bypass leak from the combustor.

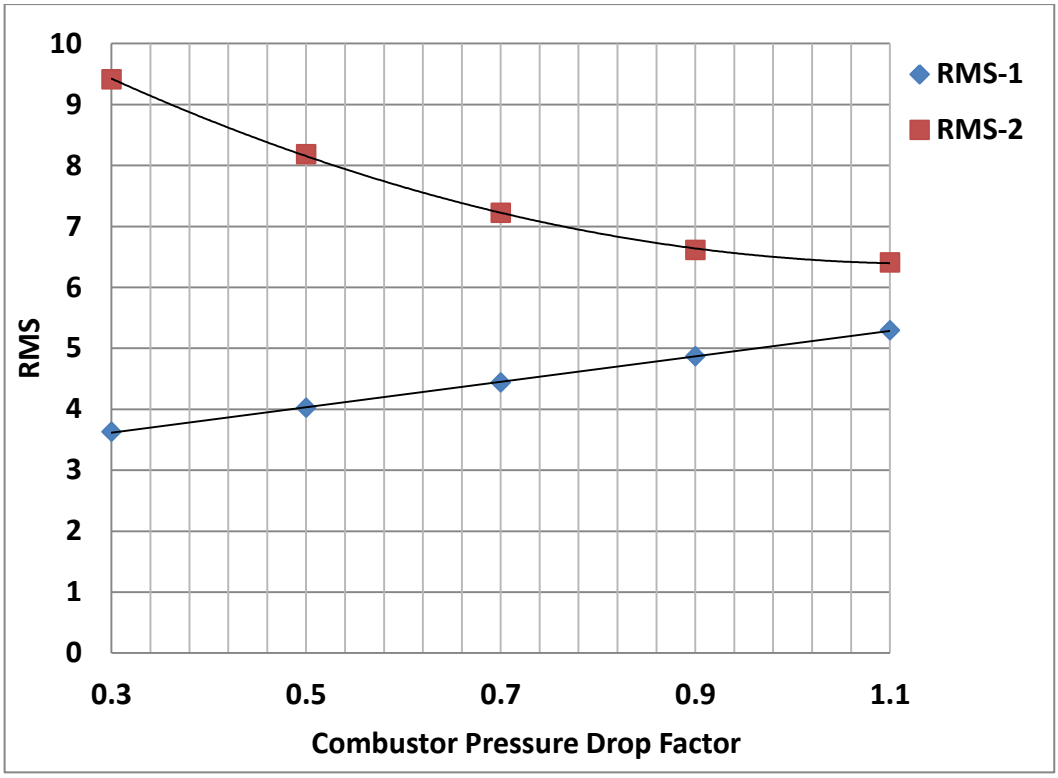

Figure 2-24 Sensitivity analysis with combustor pressure drop

2.6.4.4 Turbine section modification

In the efforts to model the machine behavior with bypass leak from the combustor (test 2), effect of turbine section modification was also analyzed. For this purpose simulations were carried out changing the turbine outlet area by a small fraction from the reference value in AE-T100 model. And results of the sensitivity analysis with turbine area modification have been presented in terms of the non-dimensional values of turbine outlet area with respect to the reference area for AE-T100 machine. Fig.2-25 shows that this parameter is also not able to model the machine performance in test 2.

Hence, above sensitivity analysis highlight that parameters like AS ratio, leak to the ambient, combustor pressure drop and turbine outlet area in the AE-T100 model are not able to capture the impact of the bypass leakage from the burner on overall machine performance experienced in the test 2. Therefore, some other analysis like compressor operating map must explain such a performance deviation in case of leakage.

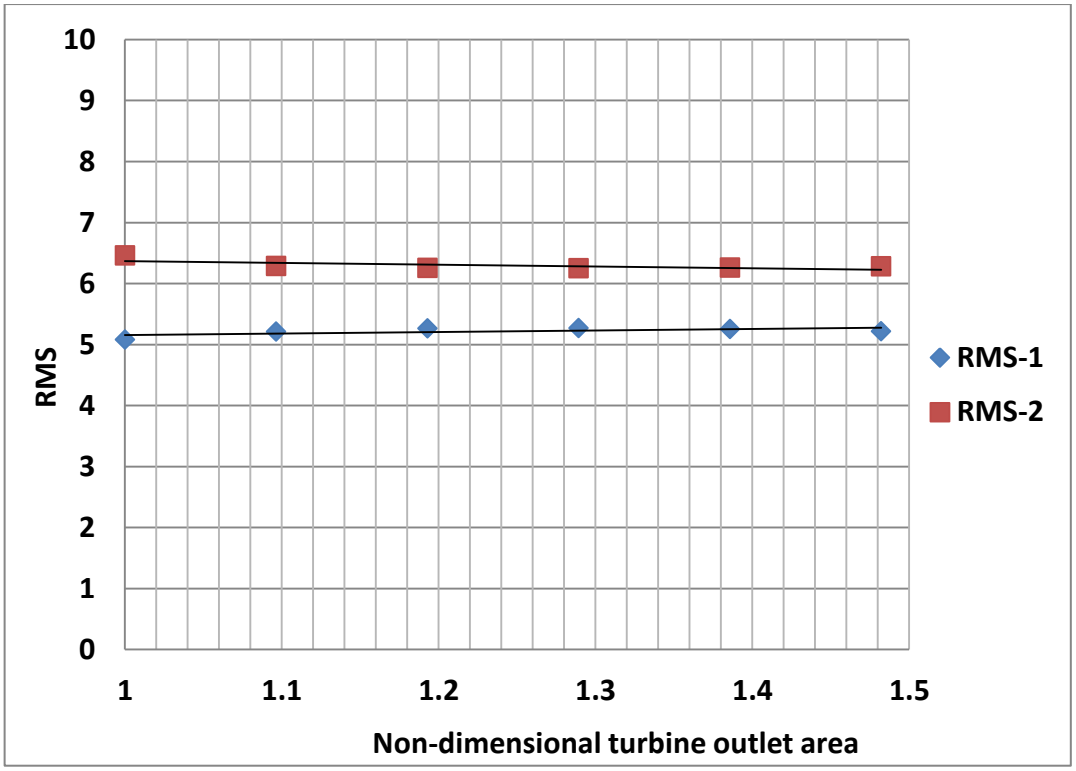

Figure 2-25 Sensitivity analysis with turbine area modification

2.6.5 Experiment at AE-T100 Test Rig after Volute Modification and Result Analysis

Afterwards, the volute-combustor joint was fixed in AE-T100 test rig through the volute modification at the Ansaldo Energia facility, and another test (test 3) was carried out to assess the machine performance. The result analysis based on the correction curves available for AET100 test rig highlighted that volute modification has resulted in improvement of the machine performance in comparison with test 2 when we had problem of bypass from burner:

- **Higher net power (about 4 kW more than that of test 2)**
- **Higher net efficiency (about 2% more than that of the test2)**

In order to understand the increased power, we focused on the compressor behavior in both cases. A detail study of the compressor maps resulted from the operating conditions of both tests revealed the change in its operating point: compressor was operating more efficiently in case of perfect joint between the volute and combustor (i.e absence of bypass leakage). The compressor performance has been compared in both cases (Table. 2.11).

Table 2.11 Compressor performance in tests with combustor leak (test 2) and after leak repairing (test 3)

Parameter	Test 2	Test 3
Isentropic efficiency (%)	78.1	78.4
Surge margin (%)	21	18
Mass flow rate (kg/s)	0.795	0.735

The shift in compressor operating point is shown by a general compressor map, remarking that actual compressor map for AE-T100 test rig cannot be shown because of confidentiality (Fig. 2-26). Shift in the compressor operating point is shown by hypothetical points 1 & 2. These results highlight that compressor is more efficient after the volute modification: higher isentropic efficiency, less air flow and thus less power consumption. Thus, efficient compression has resulted in higher net power of the machine. The other probable explanation is related to a better overall fluid dynamics in the machine due to the volute modification, which probably allows a more efficient functioning.

Hence, we can state that this leakage from the burner inlet due to the volute ovalization, have an impact on the compressor performance, which in turn affects the overall machine performance. However, this impact can only be explained by analyzing the compressor maps of both cases.

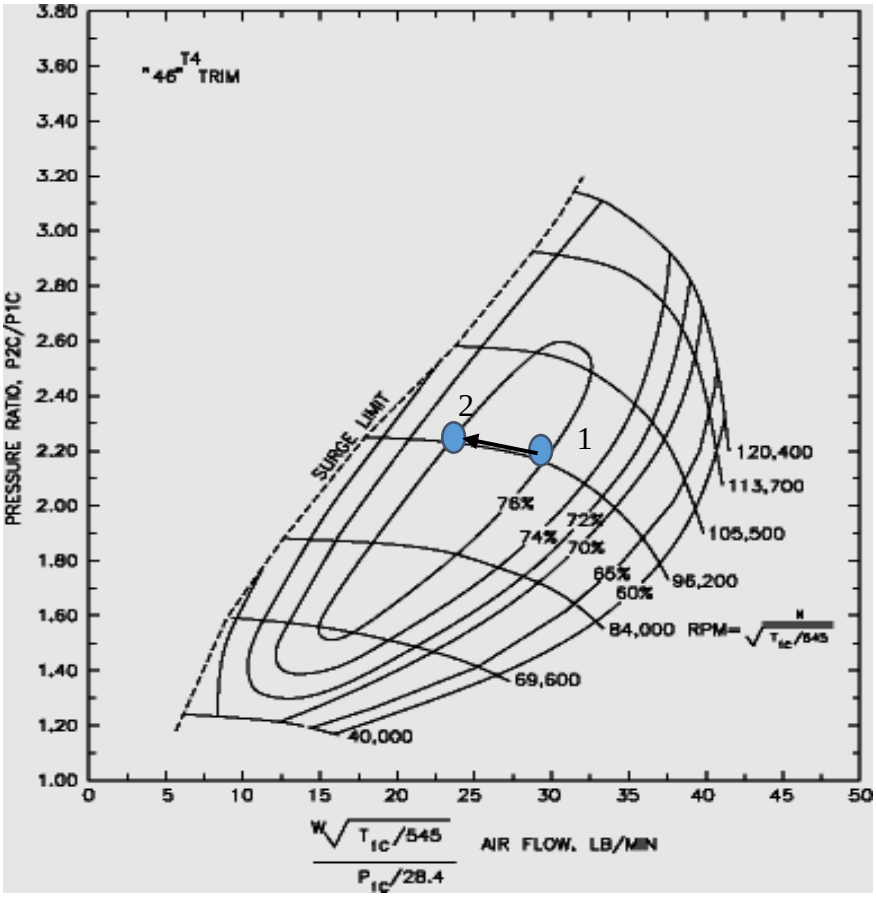

Figure 2-26 General compressor map showing shift in operating point from position 1 to 2 (hypothetical points) (Source: Garrett Turbo Maps. www.turbobygarrett.com/turbobygarrett/compressor_maps)

2.7 Final Remarks

The AE-T100 model is an upgraded steady-state simulation tool to model the mGT cycles taking into account a variety of small leakage flows, mixers, splitters and ducts, as well as a detailed analysis of auxiliary consumptions, generator and inverter efficiencies. Verification process against the reference model DSA developed by VOLVO, has proved the result quality of AE-T100 simulation. Then, the AE-T100 model was used to carry out a sensitivity analysis in order to fully characterize the mGT behavior under different ambient temperatures and loads. The effect of variation in ambient temperature on net electric power and total efficiency has been presented in this chapter.

After verification, AE-T100 model was used in real operating conditions through the Ansaldo Energia test rig AE-T100. The data have been acquired under the stable operating conditions at different power levels from 100-60 kW, considering the recuperator cold outlet

temperature as the stability indicator. After the model tuning according to real machine functioning at those operating conditions, the recuperator effectiveness has been estimated at different power levels.

Finally the AE-T100 model has been used for diagnostic aims of the whole mGT cycle with the help of two case studies from AE-T100 test rig. First case study involves the model application in real operating conditions obtained from a special AE-T100 mGT equipped with an on-purpose damaged recuperator. Comparison of the simulation results with real values indicated high deviation in the recuperator performance, and hence, proved the successful application of AE-T100 model as a diagnostic tool for T100 mGT cycles.

Second case study involved further application of AE-T100 model to simulate a real test conducted at AE-T100 test rig, during which some unexpected behavior in the machine performance was observed. The model results have indicated high deviation from the actual field data in terms of fuel flow and efficiency and hence, verified the diagnostic capability of the AE-T100 tool.

Afterwards, the experimental investigation of the test rig has discovered the presence of some crevices at the volute - combustor joint due to the volute ovalization. So it was suspected that these holes are responsible for some bypass leakage from the combustor inlet. Based on this observation, AE-T100 model was applied in order to model this leakage with the variation of AS ratio, leakage from the recuperator outlet to the ambient, combustor pressure drop and turbine section modification. But AE-T100 tool was not able to model the impact of this by-pass leak on the T100 cycle. Afterwards, the experimental data was obtained from another test which was carried out on the same test rig, after repair of the leakage through volute modification. The comparative study of compressor maps generated from the operating conditions of both tests has highlighted the change in compressor operating point and thus, more efficient compressor functioning in the absence of bypass leakage, which in turn has resulted in higher net power and efficiency from the machine, as compared to the test conducted on the same machine with bypass leak.

Hence, we can state that, although the current model AE-T100 has not the capacity to identify the exact fault in mGT cycle in some cases, however it can be effectively used to monitor the mGT operation and detect any unexpected performance.

Bibliography

1. Cochran, J., Bird, L., Heeter, J., and Arent, J.D., 2012. “Integrating Variable Renewable Energy in Electric Power Markets: Best Practices from International Experience”. Available at: NREL/TP-6A00-53732, https://www.nrel.gov/docs/fy12osti/53732.pdf, last access 08/12/2017.
2. Abdollahi, S. E., and Vahedi, A., 2005. “Dynamic Modeling of Micro-Turbine Generation Systems Using Matlab/Simulink”. The Renewable Energy & Power Quality Journal, 1 (3).
3. Ribarov, L. A., and Liscinsky, D. S., 2007. “Microgrid Viability for Small-Scale Cooling, Heating, and Power,” Journal of Energy Resources Technology, 129(1), pp. 71-78.
4. Ofualagba, G., 2012. “The Modeling and Simulation of a Micro turbine Generation System”. International Journal of Scientific & Engineering Research, 2(2), ISSN 2229-5518.
5. Paope, D.W., Carrero, M.M., Bram, S., and Contino, F., 2015. “T100 Micro Gas Turbine Converted To Full Humid Air Operation–A Thermodynamic Performance Analysis”. ASME paper GT2015-43267.
6. Goldstein, L., Hedman, B., Knowles, D., Freedman, S. I., Woods, R., and Schweizer, T., 2003. “Gas-Fired Distributed Energy Resource Technology Characterizations,” National Renewable Energy Laboratory, NREL/TP-620-34783, Nov.2003.
7. Reale, F., Calabria, R., Chiariello, F., Pagliara, R., and Massoli, P.,2012. "A Micro Gas Turbine Fueled By Methane Hydrogen Blends", Applied Mechanics and Materials, 232, pp. 792-796.
8. Zabihian, F., Fung, A.S, and D. Chiang, H.W., 2011. “Modeling of Biodiesel Fueled Micro Gas Turbine”. ASME Paper GT2011-46655.
9. Larosa, L., Traverso, A., and Massardo, A.F., 2016. “Dynamic Analysis of A Recuperated mGT Cycle For Fuel Cell Hybrid Systems”. ASME Paper GT2016-57312.
10. Camporeale, S.M., Fortunato, B., Torresi, M., Turi, F., Pantaleo, A.M., and Pellerano, A., 2015. “Part Load Performance and Operating Strategies of a Natural Gas-Biomass Dual Fueled Micro turbine for Combined Heat and Power Generation”, Journal of Engineering for Gas Turbines and Power.137 (12), pp. 121401:1-13.
11. Arnold, S., and Schatz, M., 2014. “Exploiting Waste Heat In Small And Medium-Sized Combined Heat And Power Plants Using Steam Injection”. ASME paper, GT2014-25222.

12. Duwig, C., Nyberg, B., and Thern, M., 2012. “Efficient Operation Of A Gas Turbine On Methanol Using Chemical Recuperation”. ASME paper GT2012-69032.
13. Lee, J. J., Kim, Y. S., Kim, T. S., Sohn, J. L., and Joo, Y. J., 2010. “A Gas Turbine Performance Simulation Program and Its Application to an IGCC Gas Turbine”. ASME paper GT2010-23198.
14. Sun, L., Zheng, Q., Li, Y., Luo, M., and Bhargava, R.K., 2012. “Numerical Simulation of a Complete Gas Turbine Engine with Wet Compression”. Journal of Engineering for Gas Turbines and Power, 135(1), pp. 012002:1-9.
15. Guo, X., Guo, H., 2011. “Simulation and Control Strategy of a Micro-Turbine Generation System for Grid Connected and Islanding Operations”. Energy Procedia, 12, pp. 368 – 376.
16. Rahman, M., and Malmquist, A., 2016. “Modeling and Simulation of an Externally Fired Micro-Gas Turbine for Standalone Polygeneration Application”. Journal of Engineering for Gas Turbines and Power, 138(11), pp. 112301:1-15.
17. Traverso, A., Massardo, A.F., and Scarpellini, R., 2006. “Externally Fired micro-Gas Turbine: Modelling and Experimental Performance”. Applied Thermal Engineering **26(16), pp: 1935-1941.**
18. Traverso, A. 2005. "TRANSEO Code for the Dynamic Performance Simulation of Micro Gas Turbine Cycles", ASME Paper GT2005-68101.
19. Galanti, L., Massardo, A.F., 2011. “Micro Gas Turbine Thermodynamic and Economic Analysis up to 500 kWe Size”. Applied Energy 88 (12), pp. 4795–4802.
20. Carrero, M. M., Ferrari, M.L., Paepe, W.D., Parente, A., Bram, S., and Contino, F., 2015, “Transient Simulations of A T100 Micro Gas Turbine Converted Into A Micro Humid Air Turbine”. ASME Paper GT2015-43277.
21. Aslanidou, I., Zaccaria, V., Rahman, M., Oostveen, M., Olsson, T., and Kyprianidis, K.G., 2018. “Towards an Integrated Approach for Micro Gas Turbine Fleet Monitoring, Control, and Diagnostics”. Proceedings of GPPS Forum 18, Global Power and Propulsion Society.
22. Mahmood, M., Martini, A., Traverso, A., Bianchi, E., 2016. “Model Based Diagnostics of AE-T100 Micro Gas Turbine”, ASME Paper GT2016-57671.
23. Leandri, M., 2011. “Bio-Fuels in the T-100 Gas Turbine -Simulation of Behavior Using a Matlab Program”. Department of Energy Sciences, Lund University, Sweden.

24. Henke, M., Klempp, N., Hohloch , M., Monz, T., and Aigner, M., 2015. “Validation of A T100 Micro Gas Turbine Steady-State Simulation Tool”. ASME paper GT2015-42090.
25. Farouk,N., Sheng, L., and Hayat, Q.,2013. “Effect of Ambient Temperature on the Performance of Gas Turbines Power Plant”. International Journal of Computer Science Issues, 10(1).
26. Mahmood, M., Martini, A., Traverso, A., 2017. “Fault Detection through Model Based Diagnostics of AE-T100 Micro Gas Turbine”. ASME Paper GT2017- 64619.

3 Model Based Diagnostics of AE-T100 Micro Humid Air Turbine Cycle

This chapter presents the real-time application of the AE-T100 model for an actual micro Humid Air Turbine (mHAT) plant located at Vrije Universiteit Brussel (VUB), Belgium. Modification to the basic AE-T100 model according to the VUB plant configuration, validation against the experimental data, and monitoring the recuperator performance over a certain time period of experimental activity on the VUB-mHAT system are presented.

3.1 Steam Injection or Humid Air Turbine Cycles - More Efficient CHP Production System

In the current scenario of changes in the global electricity market (as discussed in the previous chapter),small-scale Distributed Generation (DG) systems are expected to play a vital role in present and future power infrastructure. In addition to the economic feasibility offered by DG systems, combined generation of heat and power (CHP) with small decentralized CHP units, is an emerging technology. CHP systems have the potential of realizing considerable energy savings in comparison with traditional separate production systems, with net efficiency up to 80% [1-4]. However, feasibility of a CHP unit is strongly linked to the continuous heat production: when there is no or low heat demand during summers (particularly for residential cases), the exhaust heat from the co-generation facility has to be rejected. Hence, the net efficiency of the CHP production systems drops down to the electrical efficiency [5].

The Micro Gas Turbines (mGT) are attractive power generation source in the DG systems, with their promising features like high rate of exhaust heat recovery in CHP mode, compact size, high fuel flexibility, cleaner exhausts and low maintenance and operational cost. However, mGTs still have lower electrical efficiencies than similarly sized reciprocating engine generators (with 85% effective recuperator the efficiency can be as high as 30 to 33%) [6]. Hence, curtailed heat demand will lead to the mGT running at part load or even to a shutdown of the unit due to lower electric efficiency and not competitive with electricity from the grid. Thus, a finite number of running hours per year negatively affects the overall feasibility of a CHP project and results in lower investment payback [7].

Several alternative routes have been researched to improve the mGT performance and enhance the heat recovery like compressed air humidification [8-10] and water and steam injection [11-13]. These wet mGT cycles introduce flexibility in the operation of CHP plants, as they are able to achieve variable power-to-heat ratio and turbine can still operate at full electric load while covering the lower heat demand [14].

Stathopoulos et.al [15] has analyzed the thermodynamic performance of a retrofitted micro gas turbine for wet operation, in a residential building in Berlin, Germany. The study presumes the existence of a micro gas turbine and analyzes the results of its adaptation for wet operation (Fig. 3-1).

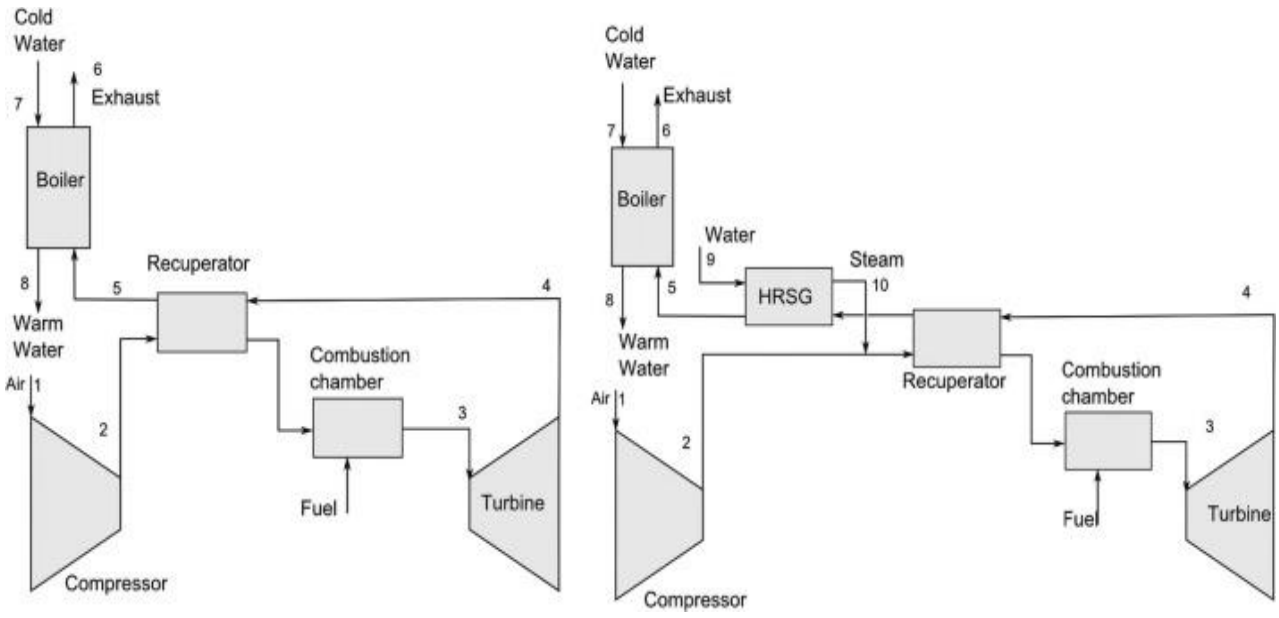

Figure 3-1. Schematic layout of the commercial (left) and the wet recuperated mGT cycle(right) [15].

The environmental and economic performance of the new system is compared to that of its commercial counterpart. It is shown that the retrofitted turbine has longer annual operation time and higher electrical energy generation. The retrofit also proves to be an attractive investment for the German CHP market with internal rates of return reaching almost 20%.

The micro Humid Air Turbine (mHAT) cycle is one of these novel cycles to increase the electrical efficiency of the mGT: exhaust gas is utilized to heat up the water and then inject back into the cycle to humidify the compressed air. Thus, air humidification improves the overall cycle performance by efficient utilization of waste heat and avoids system shutdown during hotter periods with reduced heat demand [16-18].

Starting form model development, several experimental campaigns have been carried out for thermodynamic performance analysis and optimizing the waste heat recovery through steam injection in a typical recuperated mGT cycle [19, 20], as well as to study the impact of steam rich mass flow rate on mGT behavior in the hybrid systems [21]. These experiments have proved the beneficial impact of steam injection on mGT performance: by injection of steam, auto raised with the available heat in the turbine exhaust, the fuel consumption can be reduced during hotter periods with reduced heat demand.

The injection of steam increases electric efficiency of the unit and hence avoids the shutdown of the unit. This increases the engine running hours, which has a positive impact on the net present value, resulting in a more interesting CHP investment project. This experimental work has also demonstrated the capability of the T100 to handle the compressed air humidification. Figure 3-2 shows the mGT layout used for the steam injection experiments by De Paepe et al. [19,20]: this is a typical T100 mGT equipped with low pressure steam generator, The boiler will produce saturated steam at a specific pressure. This boiler is preferred over the Heat Recovery Steam Generator (HRSG) due to lower installation cost, more flexibility and stability in the steam injection.

Considerable research activities have also been carried out in the field of experimental characterization [22], and numerical modeling of mHAT cycle. Montero Carrero et.al [23] have modeled the dynamic behavior of a Turbec T100 machine, which has been modified into mHAT cycle, with the help of the TRANSEO tool: a simulation tool which has been developed by Thermochemical Power Group (TPG) at the University of Genova, for real time

and transient analysis of complex energy systems [24]. This study is aimed at modeling the dynamic behavior of such a complex system in order to protect the components during transient operation and simulating the cycle performance in case of load fluctuations.

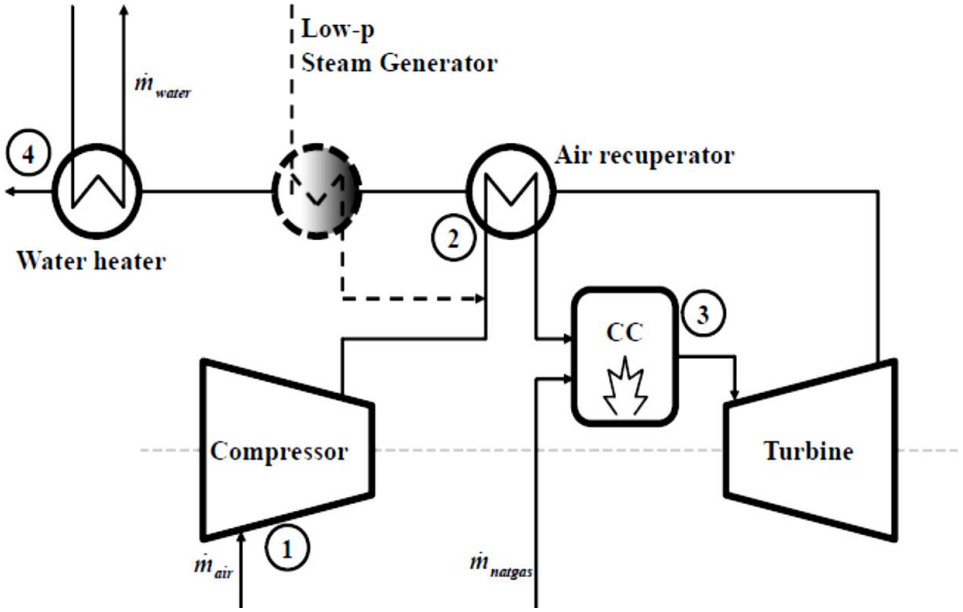

Figure 3-2 Steam injection in T100 mGT [18]

In the study conducted by De Paepe et al. [25], several advanced humidified gas turbine concepts have been applied to the mGT cycle to study their potential for waste heat recovery from the stack (Fig.3-3). The different selected cycles included: mHAT-plus, Advanced Humid Air Turbine (AHAT) and the Regeneration EVAPoration cycle (REVAP®).The results of this analysis clearly indicated that the cycle which is capable of reducing the stack temperature the most, has the highest waste heat recovery from the exhaust gasses, resulting in the highest electrical efficiency. The key for optimal waste heat recovery lies in the possibility to recover the evaporation heat from the condensing water in the stack. However, to recover this additional waste heat, a much more complex cycle layout is necessary. The optimal heat recovery can be accomplished using the REVAP® cycle concept. Within this concept, the stack can be lowered the most (up to 55.3°C), resulting in a final electrical power output of 128.7 kWe and an electrical efficiency of 42.0% (increase of 6.9% compared to the dry cycle).

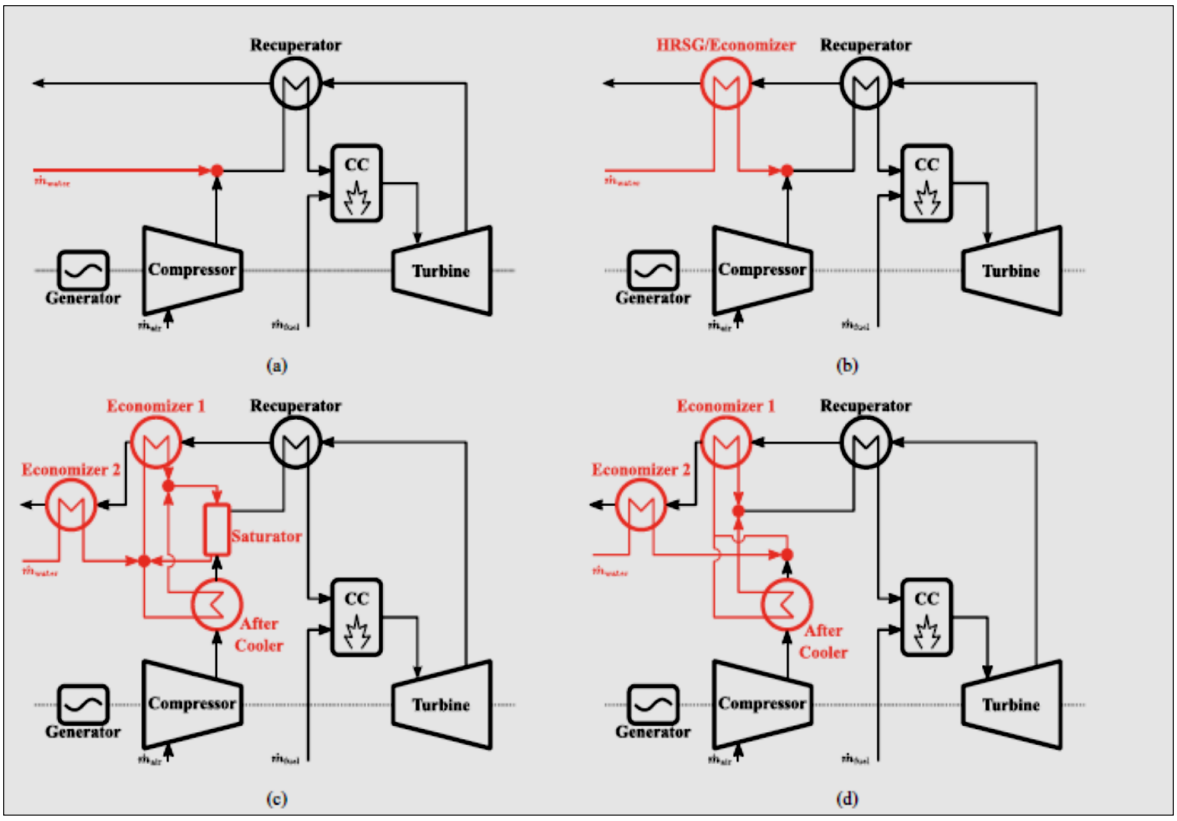

Figure 3-3.Advanced humidified mGT cycles :(a)direct water injection, (b) injection of preheated water or steam, (c) mHAT (no after cooling) or mHAT-plus (with after cooling, (d)the REVAP® cycle. The red color indicates newly introduced part necessary for the humidification (reproduced from [25)]

In addition to the overall system analysis of the mHAT cycle, component modeling and thermodynamic assessment of the humidifier has also been in focus. Parente et.al [26] have performed the thermodynamic analysis and a preliminary cost evaluation for a packed bed humidifier with two different approaches: the full integration of the mass-energy balance and mass transfer equations (called SAT model), and an atmospheric cooling tower-based model (called CT model). Two simulation cases are discussed: a test case, with experimental results from the pilot-plant of the University of Lund, and a case study of the saturators for the optimized HAT cycles of a plant with a 50 MW power output.

Pedemonte et.al [27, 28] has performed the experimental analysis of pressurized humidification tower with structured internal packing for HAT cycle, which provides relatively small pressure drop along the saturator height (Figure.3-4).

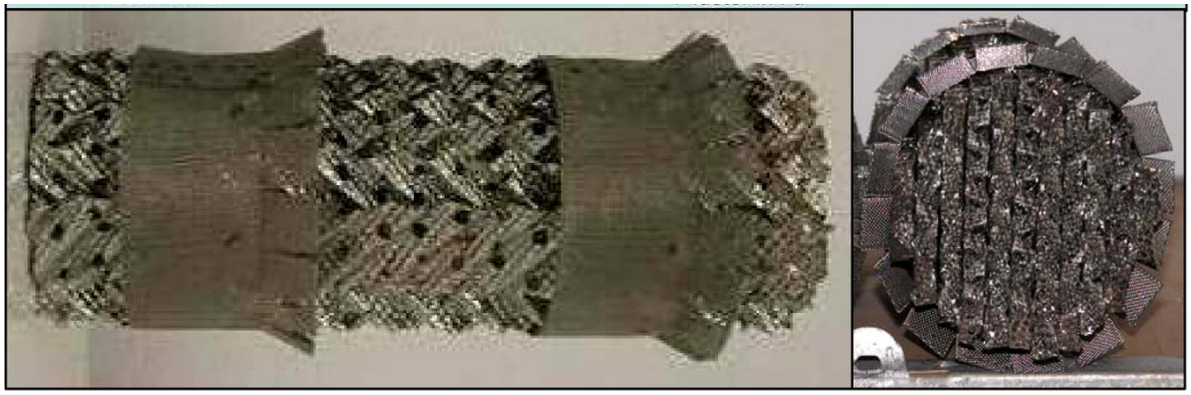

Figure 3-4 Module of structured internal packing of saturation tower (reproduced from [27, 28])

This experimental campaign carried out over 162 working points, covering a relatively wide range of possible operating conditions. Figure.3-5 illustrates the rig and shows the control panel (Labview 7.1 software) for the associated control and data acquisition system.

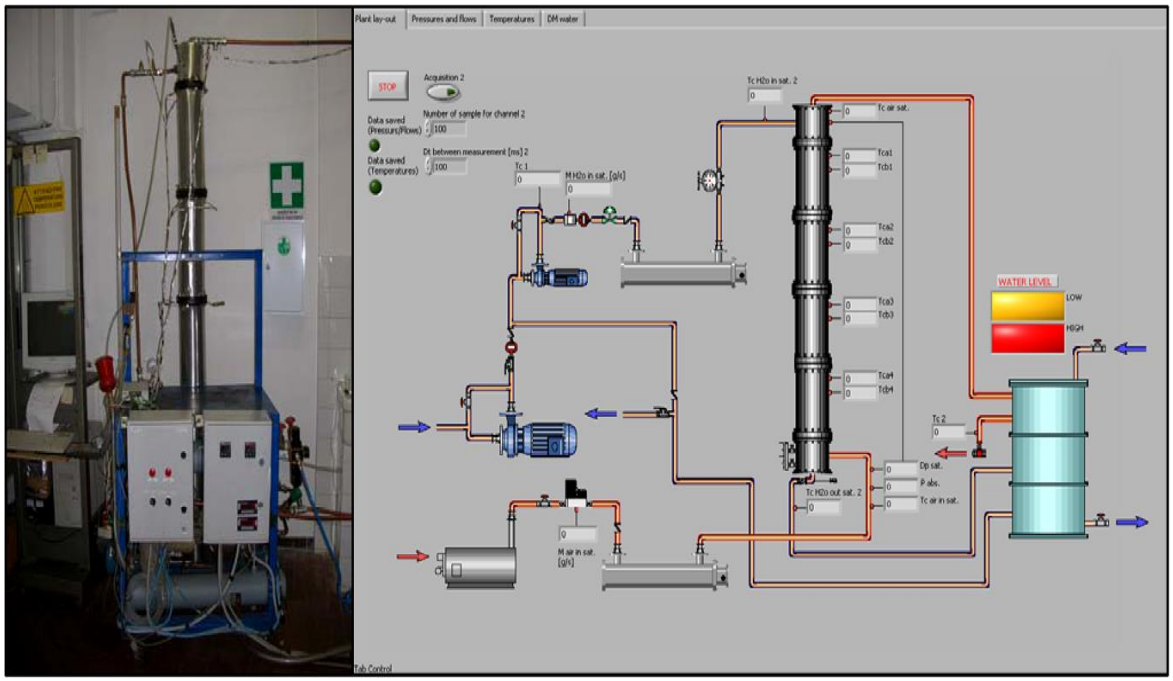

Figure 3-5. Test rig and related control panel (reproduced from [27, 28])

In the subsequent study, authors have correlated all the data points collected previously, based on two different approaches: polynomial correlation and second using a set of new non-dimensional groups, and compared these correlations to represent the data. These correlations are useful for describing the off-design behavior of the pressurized saturation

tower. The overall thermodynamic analysis showed the relation of the saturator's performance (in terms of air outlet humidity and temperature) with inlet water temperature, the inlet water over inlet dry air mass flow ratio and the inlet air temperature.

Air humidification has proven to be a very efficient of waste heat recovery. De Paepe et al. [29, 30] have presented the test rig evaluation and thermodynamic performance analysis based on the initial tests conducted on T100 mHAT system. Experimental characterization of the mHAT at full load have demonstrated the patent benefits of water injection on the mGT performance: power output of mHAT increases by more than 30% with respect to the dry operation, and electrical efficiency increases by up to 4.2% absolute points [29].

However, water injection can introduce additional pressure losses in the mGT cycle due to humidification unit and added piping, which may lead to compressor surge as surge margin is reduced [16,17]. Air humidification may also affect the recuperator performance in the long run due to corrosion, especially on the hot side. Given that this component is the most expensive of the cycle amounting up to 30% of the total capital cost [31]—the lifetime of the recuperator determines the lifetime of the mGT. Water injection significantly reduces the lifetime of the recuperator [32].

Hence, the correct assessment of the lifetime reduction during wet operation as a result of the faster degradation of the recuperator is essential for the economic feasibility of this novel cycle. The existing economic analyses showing the potential of humidified cycles like the STIG and mHAT use the classical lifetime of mGTs and consider constant cycle performance. The validity of these models depends on the correct estimation of the performance degradation and the unit lifetime. Since the humidification of mGT cycles is a rather novel concept and limited full operational test rigs and experimental data is available, hence, numerical simulation and diagnostic tools are essential for cycle optimization of the mHAT and prediction of performance degradation to allow for the correct economical assessment.

The present work intends to contribute towards this analysis. The work starts with modeling the mHAT system located at Vrije Universiteit Brussel (VUB), through the application of the AE-T100 model. As previously described, AE-T100 model is a MATLAB simulation tool, which has been developed within collaboration between the TPG at the

University of Genova (Unige) and Ansaldo Energia. The AE-T100 model is a steady state simulation tool for mGT in off-design conditions and it also possesses the diagnostic capability of mGT cycles [34, 35]. Model development, basic structure, tuning, first phase of validation through the Ansaldo Energia test rig (AE-T100) and diagnostic applications of the model have been presented in the chapter 2 of this thesis.

In this study, the basic AE-T100 model has been modified to simulate the humidified cycle according to the VUB plant layout. The modified AE-T100 model has been validated against the experimental data obtained from the mHAT unit, and recuperator performance has been analyzed at nominal and part load, under wet and dry operation. Since the mHAT cycle under study is a novel cycle of its kind, which is still under development, and there is not yet enough experimental data available of wet operation to do full diagnostics. Hence, the AE-T100 tool is applied to analyze the recuperator performance degradation in the VUB- mHAT system over the past five years, based on several sets of experimental data. The recuperator actual design effectiveness, determined based on the new set of design conditions, is compared with the initial value provided by the supplier. This comparison determines the recuperator performance degradation since the start of experimental activities on the mHAT system, in dry mode.

3.2 Plant Layout of VUB-mHAT System

The VUB-mHAT system is based on the natural gas-fired mGT Turbec T100 (version 2), which is a typical Brayton cycle with regeneration. The Turbec T100 present at Vrije Universiteit Brussel (VUB) has been converted into a mHAT following the layout shown in Fig.3-6. In grey, the elements correspond to a typical recuperated mGT, and the components that have been added to transform the unit into an mHAT have been marked with orange color. In the current configuration, the incoming air is compressed in the radial compressor (1) and subsequently humidified in the saturation tower (2), where hot water at around 80°C is sprayed. Thereafter, the saturated air is preheated by the exhaust gases in the recuperator (3) before entering the combustion chamber (4), where natural gas is burnt until reaching a Turbine Inlet Temperature (TIT) of 890°C corresponding to Turbine Outlet Temperature (TOT) of 645°C.

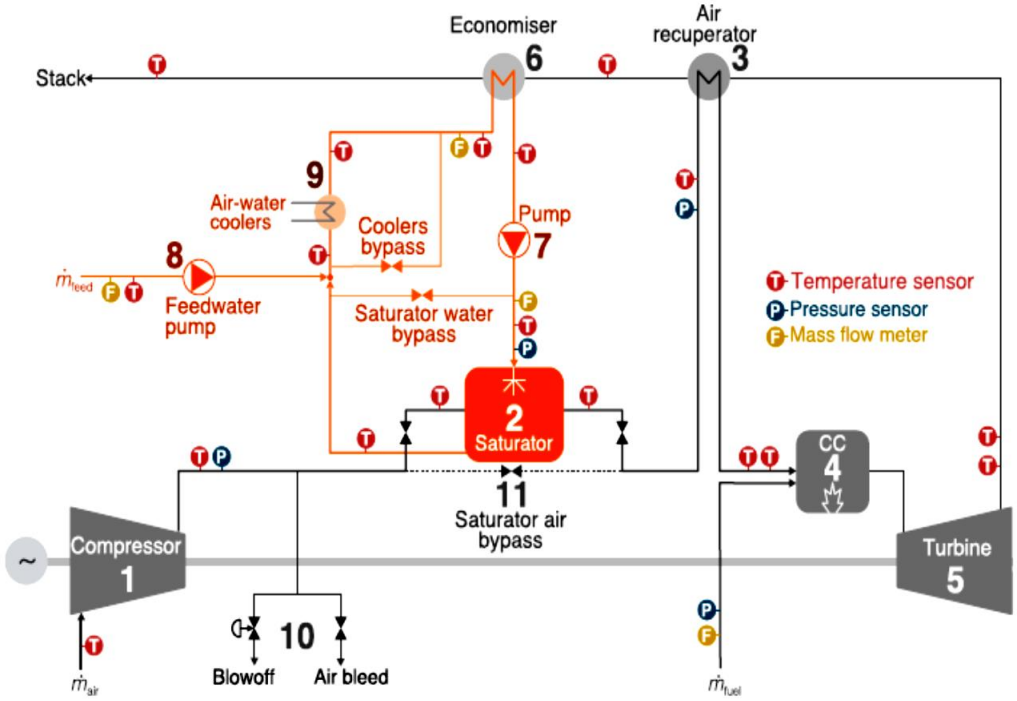

Figure 3-6. The schematic layout of the VUB- mHAT cycle along with all the sensors installed in the facility. In grey, the elements corresponding to a typical recuperated mGT. In orange, the components that have been added to transform the unit into a mHAT (reprinted from [31]).

The flue gas expands in the turbine (5), which drives the compressor through a single shaft while the extra shaft power is converted into electricity in a high speed generator [29]. Exhaust gases from the recuperator is used to warm up water in the economizer (6). This hot water is then routed towards the saturation tower. A variable speed pump (7) maintains the 2.5 kg/s of circulating water in the hot water circuit and controls the injection pressure of the nozzles in the saturation tower. In order to make up for the evaporated water, which amounts to 48 g/s at nominal power output (100 kW), feed-water is added to the system through a feed-water pump (8). Since the current facility is not connected to the heating system of the university, whenever necessary the water is cooled down in two air-water heat exchangers (9)[23].

For the VUB-mHAT test rig, a specific saturator, using a water spray instead of packing material to enlarge the contact area between water and air, and to enhance heat and mass transfer, has been developed and installed [34]. Figure 3-7 shows the saturation tower designed for the mHAT cycle and mGT integrated with humidification unit. The test rig has

been equipped with several sensors (as shown in Figure 3-6) to measure temperature, pressure and flow rates, enabling the assessment of the impact of cycle humidification on the mGT performance (a full description of the installed sensors can be found in [31]).

Figure 3-7. Saturator for VUB-mHAT system (left), T100 test rig modified to connect with humidification unit (right).

3.2.1 Experimental Data from VUB- mHAT System

Air humidification increases the vapor content of the air, and air enthalpy and air mass flow are also increased while the heat of evaporation is extracted from the circulating water below boiling temperature. In wet operation mode, the humidified flue gas has a higher heat capacity than in the dry T100. Therefore, for a certain requested power output, since TOT is fixed to 645°C, a lower TIT at 890 C than the corresponding to the one of the T100 (which amounts to 950 °C) is required at nominal conditions. In order to effectively characterize the effect of water injection in the mHAT unit, experiments are conducted at constant rotational speed instead of constant power output mode, as it limits the results obtained in dry operation. In addition, the process of water injection is optimized to ensure that the air is fully humidified at the outlet of the saturation tower [23].

The test results used for this study presented here were obtained following the test procedure described in [20]. This test procedure includes an initial dry run of the mGT to preheat the installation prior to water injection, followed by a wet run. Water injection is

initiated before the mGT is started, since direct injection during a dry run leads to sudden flameout of the mGT due to the sudden change in combustor inlet air temperature. At the end of each water injection test, a dry reference was captured, by performing a dry run. For the humidified tests with the VUB-mHAT test rig, the original mGT control system was slightly adapted. As described by Montero Carrero et.al [31], due to the rather high pressure losses induced by the saturator and the connecting piping, the requested power output could not be obtained during the dry reference run, which does not allow for a correct comparison of the mHAT performance with dry mGT operation. Therefore, both dry and wet experiments have been performed at constant rotational speed at the VUB-mHAT test rig.

Extensive experimental work has been carried out in dry mode, during past five years (from 2012 to 2017), at the speed ranging from nominal rotational speed of 70,000 rpm (100%) to part load (down to 86%). Figure 3-8 shows the speed range during all the dry tests: each point corresponds to a test. However, these tests are not uniformly distributed over the period of five years: maximum number of tests has been conducted during 2012, with very few tests conducted during 2017.

Since the VUB-mHAT system is still under development, hence few numbers of tests have been performed in the wet mode during the year 2015. Similar to the dry tests, wet tests are also not consistent over the period of one month: maximum number of test have been conducted during second half of September 2015. During the wet tests, the rotational speed was varied between nominal rotational speed (70,000 rpm) and partial rotational speed (down to 89% of the nominal speed, Figure 3-9).

Therefore, the mGT control system was adjusted from constant power output mode to constant rotational speed mode. The second control loop in the controller, being TOT control, was not changed during the wet experiments. Test results showed that without changing the control system, a constant TOT of 645°C could be obtained during wet runs at constant rotational speed, highlighting the stability of the control system [31]. Finally, to protect the compressor against surge during emergency shutdown, during all wet experiments, a small fraction of the compressor air flow rate was bled.

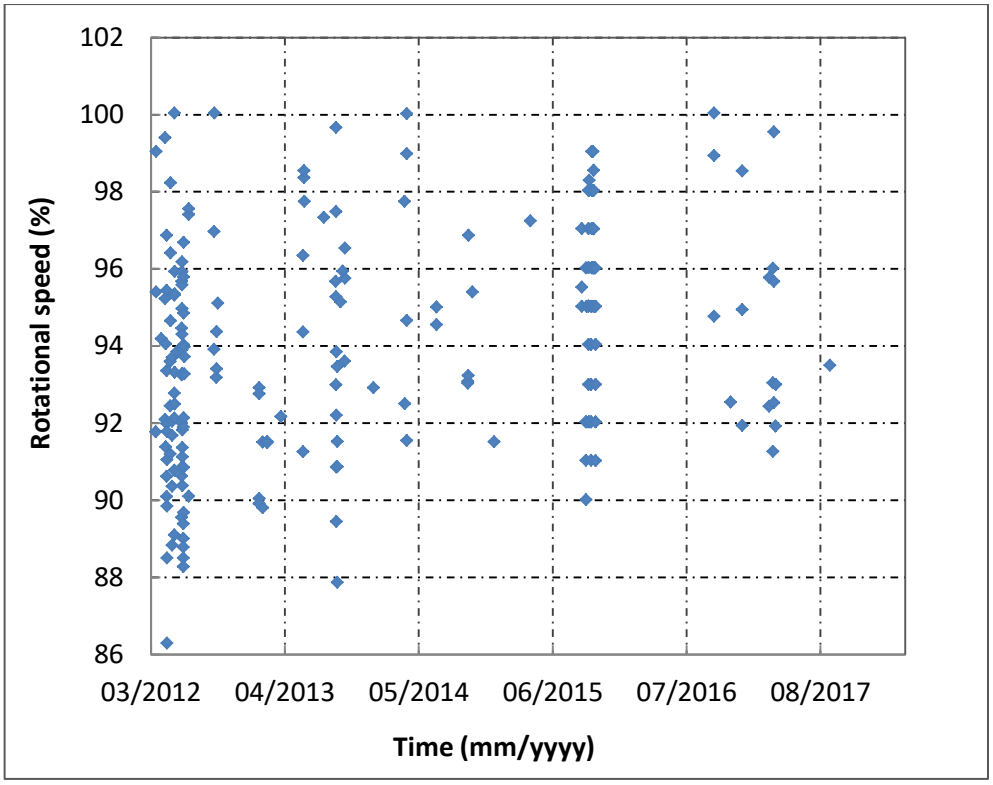

Figure 3-8.Tests conducted at VUB-mHAT test rig in dry mode.

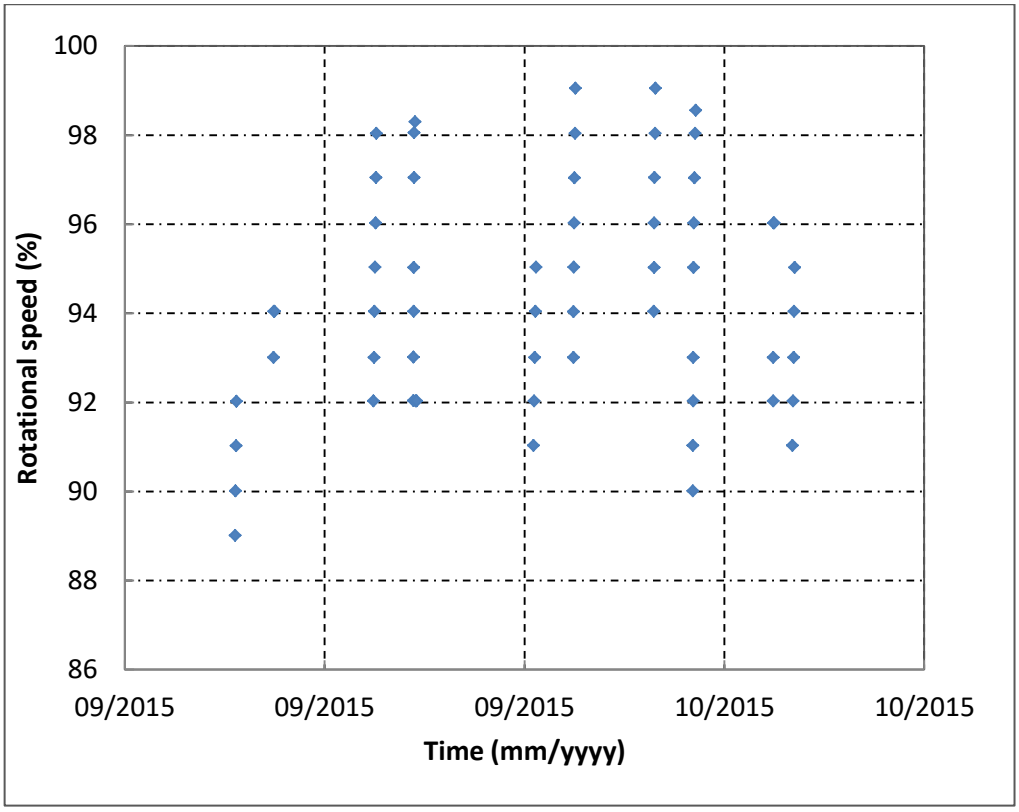

Figure 3-9.Tests conducted at VUB-mHAT test rig in wet model

3.3 Modelling the VUB-mHAT Cycle

As explained before, AE-T100 model is a steady state simulation tool for mGT in off design conditions, and it also possesses the diagnostic capability of mGT cycles. It is developed from BT-100 model available at Ansaldo Energia, and validated against a reference model Dynamic System Analyzer (DSA), which has been originally developed by VOLVO.

Thermodynamic equations for each component are solved in the MATLAB environment, based on the design conditions and inputs provided by the user through graphical user interface (GUI). Overall mathematical approach involves the iterative process inside the MATLAB code, to determine the mGT parameters. Model development, basic structure, tuning, first phase of validation through the Ansaldo Energia test rig (AE-T100) and diagnostic applications of the model have been presented in chapter 2 of this thesis.

3.3.1 Modifications to the Basic AE-T100 Model

In order to simulate the VUB-mHAT cycle, the basic AE-T100 model has been modified accordingly (red components in Figure 3-10). Considering the simple approach, this modification does not involve any saturator model, but it simply involves the addition of an additional Mixer (M) in the basic model and consequent changes in the thermodynamic parameters of the cycle. Thus, the saturation tower is modeled with the help of the Mixer, where a water stream at 80°C, heated by the exhaust gases, is mixed with compressed air. As a result, the outlet air of the saturator is fully humidified, having higher enthalpy, higher mass flow rate and higher specific heat capacity, which is then fed to the Recuperator (Rec). Afterwards, the mHAT cycle is modeled with the same approach as in the previous configuration of AE-T100 model. However, more detail on the mathematical approach and thermodynamic equations cannot be mentioned explicitly due to confidentiality. Figure.3-10 shows the modified AE-T100 model layout for VUB-mHAT cycle (basic AE-T100 model layout has been presented in Figure 2-10).

Legend	
S	Splitter
D	Duct
M	Mixer
ED	Exhaust Diffuser
HE	Heat Exchanger
G	Generator
CC	Combustion chamber
C	Compressor
Rec	Recuperator
T	Turbine
S	Stack
FWP	Feed Water Pump
S.T	Saturation Tower

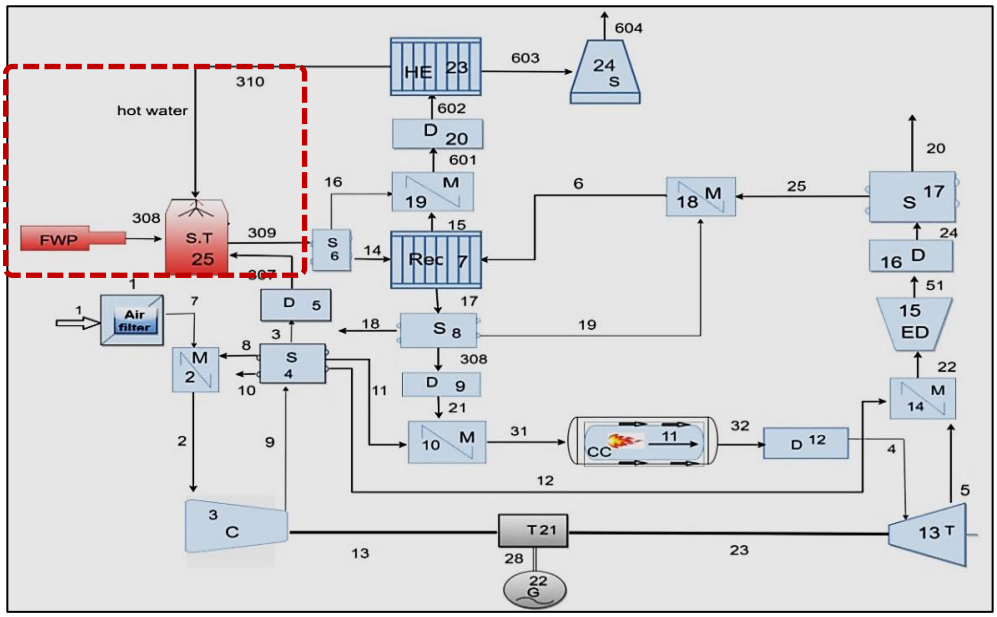

Figure 3-10 Modified AE-T100 model for VUB-mHAT cycle: legend on the left shows the component symbols. The components of the original dry model are presented in blue, while the newly integrated components to allow for the simulation of cycle humidification are presented in red.

3.3.2 Model Tuning Concept

The numerical modeling assumes ideal performance of the whole system, referring to the initial or non-degraded mGT. Due to experimental activities over time, machine performance degrades, and so the design conditions also change. After a certain time period, the machine performs on a different set of design conditions than initial ones. In order to model the real machine functioning, the AE-T100 model requires proper tuning of the design parameters at the specific operating conditions, to get the corresponding off-design conditions. Therefore, model tuning is the first step for real time application of the AE-T100 model.

For this study, the AE-T100 model is tuned according to the operating conditions of VUB-mHAT system, for which experimental data have been acquired under the stable operating conditions of the machine, (detail of experimental data have been mentioned in the previous section). In order to estimate the design conditions, the reverse problem technique is applied i.e estimation of design conditions based on the field results, using the DSA (Dynamic System Analyser) tool.

This DSA tool which has been developed by VOLVO, provides the design conditions according to the operating point of the real machine, which is different from the ISO conditions. The process starts with the AE-T100 model application to simulate the actual machine performance, and then model results are compared with the field data. The relative percentage error of the tuned model values with respect to the experimental ones for each parameter is calculated according to Eq.3.1, and then average value of all the errors i.e Root Mean Square Error (RMSE) value is calculated (Eq.3.2) Then RMSE is checked against a desired tolerance. If the RMSE value meets the defined criterion, it indicates the correct set of design conditions.

$$e_{rel,i} = \frac{(x_{field,i} - x_{tuned,i})}{x_{field,i}} \times 100 \qquad (3.1)$$

$$\boldsymbol{RMS} = \sqrt{\frac{\sum_{i=1}^{N}(e_{rel,i})^2}{N}} \qquad (3.2)$$

where N represents total number of parameters

In case when the RMSE value exceeds the defined limit, the DSA tool is applied with the different fuel and leakages. This tuning provides the new set of design conditions. Afterwards, the AE-T100 model is applied again with the design conditions obtained from the DSA tool, and compare the results with field data, and checked RMSE. This iterative process is continued until the defined criterion of RMSE is satisfied. This tuning practice provides the correct design conditions for the AE-T100 model, so that the whole model is able to simulate the actual machine performance in the off-design conditions, with the minimum percentage error of all thermodynamic parameters. Figure.3-11 represents the process flow for tuning of the design conditions of AE-T100 model at full load. Unlike manual tuning, this tuning algorithm has been implemented by an automatic routine in the model, so that we are able to tune the model with less computational effort.

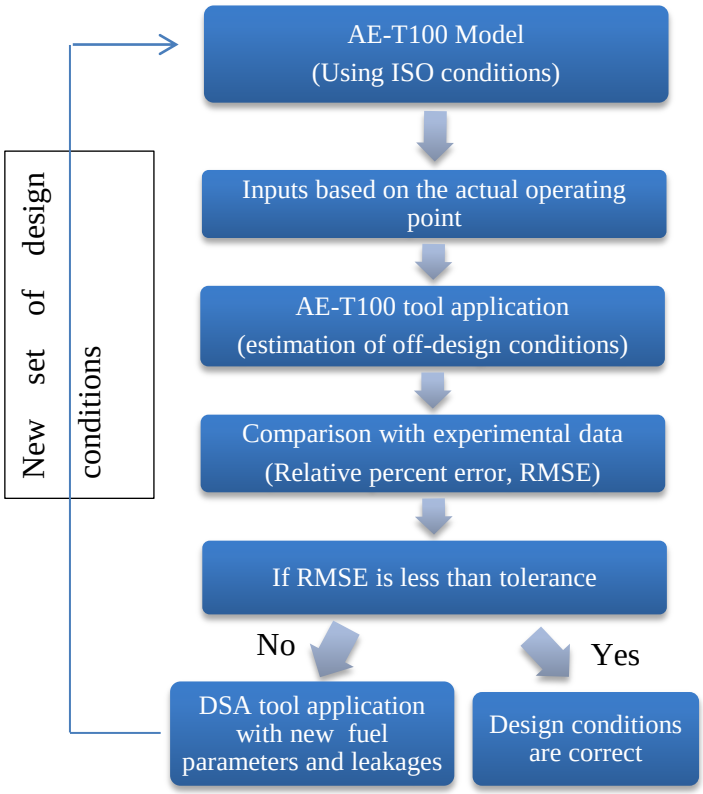

Figure 3-11 Process flow for AE-T100 model tuning

3.3.3 Model Validation in Real Operating Conditions

The new set of design conditions for test at nominal load in dry and wet mode have been estimated by the tuning routine explained in previous section (Figure 3-11). Table 3.1 presents the results of the comparison among tuned model and experimental values at full load condition, in dry operation of the mHAT rig.

Table 3.1. Comparison of tuned model values with experimental values at full load in dry mode

Parameter	x_{field}	x_{tuned}	e_{rel} **(%)**
Compressor outlet temperature (^{o}C)	219.75	224.45	-2.13
Compressor outlet pressure (barg)	3.37	3.43	-1.80

Recuperator inlet air pressure	3.26	3.20	1.87
Recuperator air outlet temperature (^{o}C)	598.45	602.55	-0.68
Turbine inlet temperature (^{o}C)	949.36	935.71	1.43
Net electrical power (kW)	91.57	94.11	-2.77
Fuel flow rate (g/s)	8.54	8.53	0.10
RMSE			**1.75**

In addition to the dry tests, the AE-T100 model has also been applied in real operating conditions of the VUB-mHAT cycle in the wet mode. For this purpose, the AE-T100 model has been tuned and validated against the field data in wet mode, following the same tuning routine as in the case of dry mode. Table 3.2 presents the results of the comparison among tuned model and experimental values at full load condition, in wet operation of the mHAT rig.

Table 3.2 Comparison of tuned model values with experimental values at full load in wet mode

Parameter	x_{field}	x_{tuned}	e_{rel} **(%)**
Compressor outlet temperature (^{o}C)	213.67	217.62	-1.84
Compressor outlet pressure (barg)	3.50	3.44	1.51
Recuperator inlet air pressure	3.26	3.21	1.51

Recuperator air outlet temperature (^{o}C)	582.64	588.00	-0.91
Turbine inlet temperature (^{o}C)	945.90	936.14	1.03
Net electrical power (kW)	96.96	96.15	0.83
Fuel flow rate (g/s)	8.96	8.95	0.11
		RMSE	**1.22**

Since, for both dry and wet conditions, RMSE is less than tolerance level (which was set at 5% considering the certain number of unknown parameters in the actual mHAT cycle, e.i. compressor air mass flow rate and bleed flow rate), this proves that the AE-T100 model is tuned to simulate the actual performance of the mHAT test rig, with reasonable accuracy at full load conditions.

3.4 Results and Discussion

As mentioned before, despite the potential benefits of mHAT cycle in terms of higher electrical efficiency and power output, water injection has also some negative effects on the mGT cycle: additional pressure losses in the cycle due to the humidification unit and performance degradation of the recuperator. Since air humidification also increases the water vapor content of air entering the recuperator, which may cause corrosion in the recuperator. Thus, the recuperator effectiveness can degrade over the time of experiments. Hence, current analysis is focused only on the recuperator performance in the mHAT cycle, in both dry and wet operation.

The new design conditions which have been estimated by tuning at full load are used:

- To estimate the off-design performance of the recuperator over the experimental data provided by VUB-mHAT facility in both dry and wet mode, most of which are conducted at part load operating conditions

- To estimate the new recuperator design effectiveness in order to analyse its degradation through the comparison with the initial design value provided by the supplier.

The off-design recuperator performance at variable loads is shown in Figure 3-12, in both wet and dry mode. All the values of recuperator effectiveness have been reported in non-dimensional form with respect to the standard value from the supplier, since actual values cannot be mentioned due to confidentiality.

When looking at the recuperator effectiveness, it is clear to see that the performance of the component increases when shifting from full load to part load, for the dry, as well as the wet case (Figure 3-12). This increase is evident, since at part load, the air flow rate passing through the compressor is lower and thus less air enters the recuperator cold side. At the same time, the air flow rate on the hot side is also reduced; however the contact area for heat exchanger remains constant, finally resulting in higher effectiveness when going from full to part load operation.

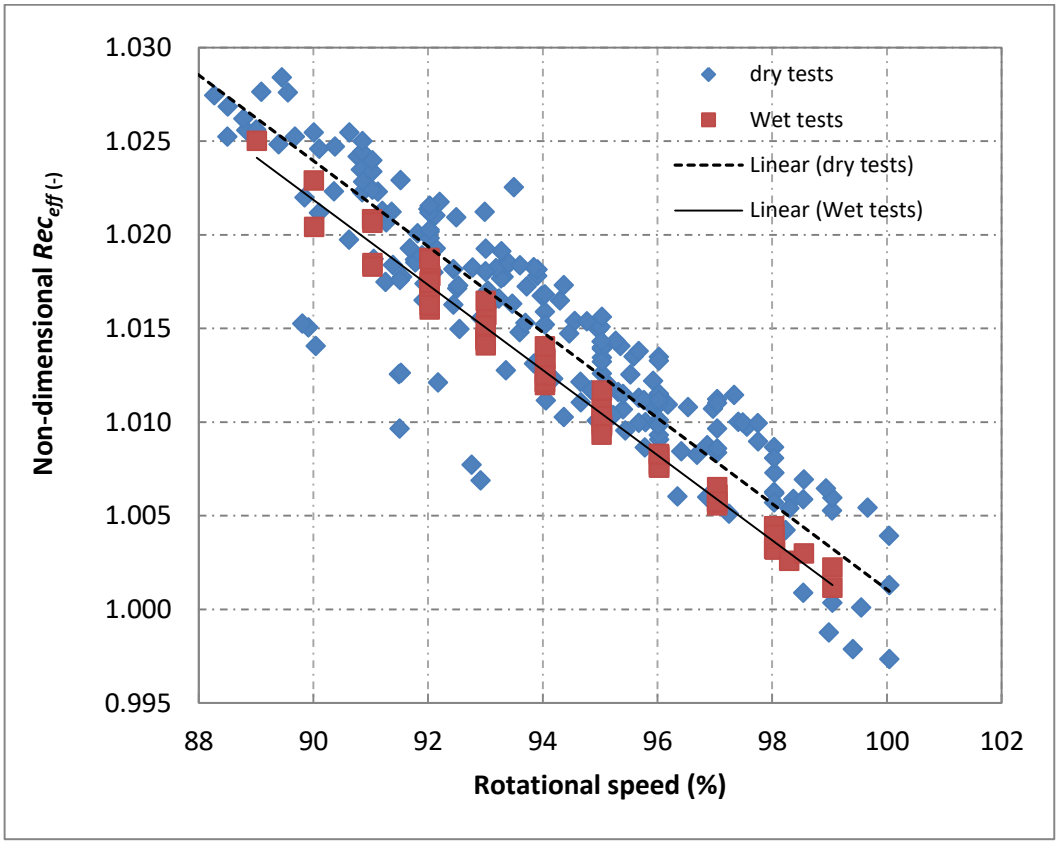

Figure 3-12. Recuperator performance with variable load in wet and dry mode

When comparing the increasing trend in recuperator effectiveness in dry and wet operation when shifting to part load, we can see a quasi linear trend for the increasing effectiveness. However the increase in effectiveness towards part load operation is slightly higher in the dry case, compared to the wet case. At the same time, the net heat exchange in the wet case is significantly higher due to the lower cold side inlet air temperature (hot side inlet air temperature remains constant at 645°C due to the TOT control), the reduced mass flow rate and increased specific heat capacity of the working fluid due to the humidification process. So although the net heat exchange is higher in the wet case, the lower effectiveness at part load indicates that there is potential to recover even more heat by redesigning the recuperator, focusing on wet operation performance.

Finally, the recuperator performance degradation of the VUB-mHAT system, as a result of the performed dry and wet tests, has been assessed using the AE-T100 model. The model has been applied on the dry test results of experiments conducted over the past five years (test shown in Figure 3-8) on the VUB-mHAT system. For this purpose, model has been tuned (following the same tuning practice as shown in Model tuning) and validated based on the same parameters as presented in Table 3.1 and 3.2, to get the new set of design condition. Afterwards, the actual recuperator design effectiveness ,which was determined based on the new set of design conditions at full load (or close to the full load), is compared with the initial value provided by the supplier, to see the degradation under the dry operation over the last five years (Table 3.3 and Figure 3-13).

Table 3.3. Estimation of the recuperator performance degradation in dry operation

Time (dd/mm/yyyy)	**Rotational speed (%)**	**Number of tests included in each time interval**	**Degradation (%)**
08/05/2012	100	36	0.14
04/09/2012	100	51	0.42
29/08/2013	99.67	29	0.87

27/03/2014	100	21	1.10
29/09/2015	99.04	45	1.65
21/09/2016	100	20	1.87
17/03/2017	99.55	12	2.01

The analysis of the dry recuperator effectiveness indicates clearly that, over the past 5 years, the recuperator has degraded significantly (Table 3.3 and Figure 3-13). The non-dimensional value of the effectiveness, obtained by comparing the current value with the initial design effectiveness, has decreased by 2.01% as a result of the continuous tests in dry and wet operation. Although, only a limited amount of wet experiments have been carried out on the mHAT-VUB test rig so far (see Figure 3-9), the recuperator effectiveness is already degrading in the range of 0.1% to 0.4 % per year.

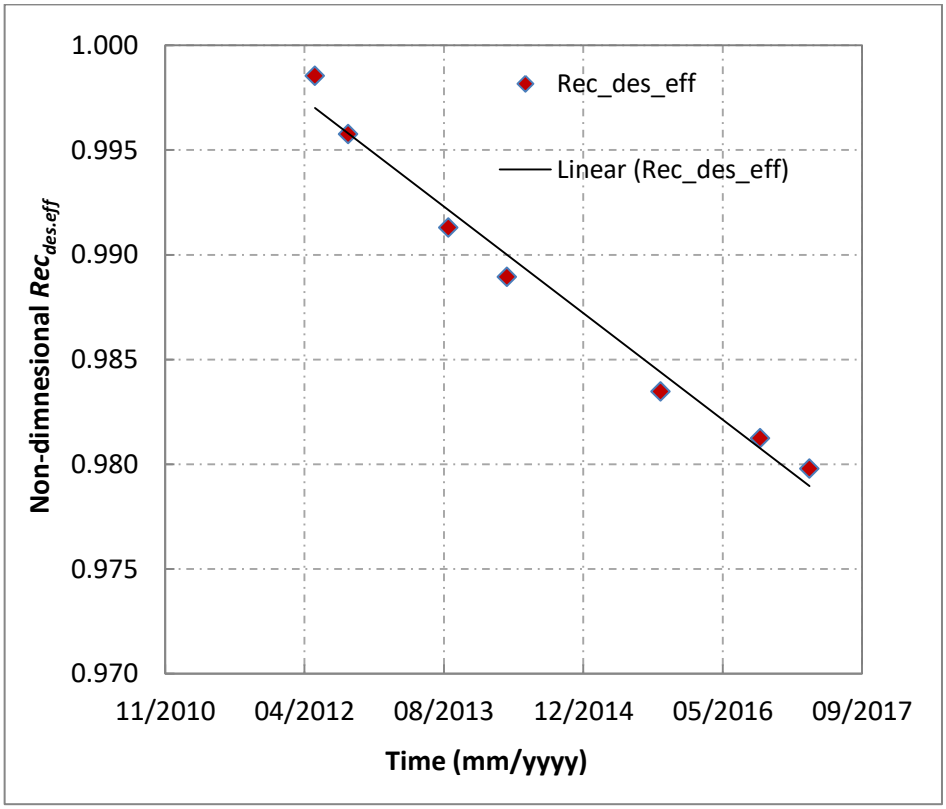

Figure 3-13. Recuperator performance degradation in dry mode over five years of tests

In addition, the change in recuperator design effectiveness is almost linear with the time, although, it depends on several factors such as, the number of tests carried out on the test rig between time interval; the total duration of the test conducted; the operating conditions; the ambient conditions and fuel parameters and finally any possible modification applied to the test rig. Finally, we also notice that this linear effectiveness reduction already started before the wet experiments had been started i.e effectiveness had decreased by 1.65% until the year 2015. This indicates that the degradation is not only a result of the wet operation, but also of the dry operation. A more in-depth analysis is however necessary when more wet experiments have been conducted over a longer period, to see if this will have an impact on the degradation rate of the recuperator.

Similar to the dry case, the recuperator performance degradation in the wet mode can also be analysed. However, at present, the lack of experimental data, captured over a longer time period of wet operation, does not allow for a complete diagnostics of this novel cycle through the AE-T100 tool. Hence, the preliminary assessment of the degradation in dry mode already provides a basis for a more advanced diagnostic application of the AE-T100 tool. Finally, this advanced diagnostic application of the AE-T100 tool will allow us to report the recuperator degradation and to estimate the impact of air humidification on the recuperator effectiveness.

3.5 Final Remarks

The AE-T100 model is a steady state simulation tool that also possesses the diagnostics capability of the mGT cycle. In this work, the AE-T100 model is applied to simulate the mHAT system located at Vrije Universiteit Brussel (VUB). This involves modification in the basic AE-T100 model (since this has been designed to simulate the dry operation of AE-T100 machine) according to the VUB-mHAT cycle configuration. Afterwards, the modified model has been tuned following a routine based on the RMSE criterion, to estimate the correct set of design conditions. Once the model has been validated in real operating conditions at full load, it is applied to analyze the mHAT cycle over the set of several experiments conducted at the nominal and part load in both dry and wet operation mode, with particular focus on the recuperator performance. The recuperator design effectiveness is determined based on the new set of design conditions.

To see the degradation/change in the recuperator performance with time, the new recuperator design effectiveness is compared with initial design value from the supplier. However, since VUB-mHAT cycle is a novel cycle, there is not yet enough experimental data available to do a full diagnostics in wet mode, hence, we applied it for all the dry tests conducted over past five years (2012-2017) on the VUB- mHAT test rig, to demonstrate the first diagnostic application of the AE-T100 tool. The analysis on the dry experiments highlighted that, although a limited amount of wet tests have been conducted on the VUB-mHAT system so far, already a clear recuperator effectiveness degradation could be reported (2.01% over the time period).

In conclusion, this preliminary analysis of the recuperator performance in dry mode provides the basic pathway or algorithm that can be applied for more detailed diagnostics of the mHAT cycle in future, under wet operation over longer time scale. This work also highlights the necessity of more parameters measurement (like pressure drops at certain points of the mHAT cycle) from experiments, to help the model validation further.

3.6 Future Work

In this paper, we have proved the capability of the AE-T100 tool to adapt to a different plant layout i.e mHAT cycle in this case. It also indicated the potential of the AE-T100 tool to be used as a diagnostic tool and predict the performance degradation of the VUB-mHAT test rig, with particular focus on the recuperator. On this test rig, in the past, several other test campaigns with steam and water injection have already been performed. In addition, currently, a large measurement campaign is ongoing to study the dynamic behavior of the mHAT and its capacity to operate in a larger DG network by controlling the mHAT based on the thermal load. This campaign involves intensive water injection experiments spanning over several weeks/months. After this test campaign, a more in-depth analysis of the mGT and more specifically the recuperator performance degradation is planned using the AE-T100 tool, with all tests data captured over the years. Hence, this preliminary analysis together with further experimental data, will be used for more detail diagnostics of the mHAT cycle, to predict the degradation of the recuperator under wet operation, and by doing so, allowing to predict the lifetime of the recuperator under wet operation.

Bibliography

1. Cochran, J., Bird, L., Heeter, J., and Arent, J.D., 2012. “Integrating Variable Renewable Energy In Electric Power Markets: Best Practices From International Experience”. NREL/TP-6A00-53732. http://www.nrel.gov/docs/fy12osti/53732.pdf.
2. Arnold, S., Schatz, M., 2014. “Exploiting Waste Heat In Small And Medium-Sized Combined Heat And Power Plants Using Steam Injection”. ASME paper GT2014-25222.
3. Abdollahi, S. E., and Vahedi, A., 2005. “Dynamic Modeling of Micro-Turbine Generation Systems Using Matlab/Simulink”. The Renewable Energy & Power Quality Journal, 1 (3).
4. Rossi I., Sorce A., Traverso A., Gas turbine combined cycle start-up and stress evaluation: A simplified dynamic approach. Applied Energy, 190 (2017) 880–890.
5. Delattin, F., Bram, S., Knoops, S., and De Ruyck, J., 2008, "Effects of Steam Injection on Micro turbine Efficiency and Performance". Energy, 33(2), pp. 241-247.
6. Ofualagba, G., 2012. “The Modeling and Simulation of a Microturbine Generation System”. International Journal of Scientific & Engineering Research, 2(2), ISSN 2229-5518.
7. Kaikko, J., and Backman, J., 2007, "Technical and Economic Performance Analysis for a Microturbine in Combined Heat and Power Generation," Energy, 32(4), pp. 378- 387.
8. De Paepe, W., Montero Carrero, M., Bram, S., Parente, A., and Contino, F., 2017. “Towards Higher Micro Gas Turbine Efficiency and Flexibility: Humidified mGTs- A Review”, ASME Paper: GT2017-64857.
9. Jonsson, M., and Yan, J., 2005, "Humidified Gas Turbines – a Review of Proposed and Implemented Cycles," Energy, 30(7), pp. 1013-1078.
10. Dodo, S., Nakano, S., Inoue, T., Ichinose, M., Yagi, M., Tsubouchi, K., Yamaguchi, K., and Hayasaka, Y., 2004, "Development of an Advanced Microturbine System Using Humid Air Turbine Cycle," ASME Paper GT2004-54337, pp. 167-174.
11. De Paepe, W., Contino, F., Delattin, F., Bram, S., and De Ruyck, J., 2014, “Optimal Waste Heat Recovery In Micro Gas Turbine Cycles Through Liquid Water Injection”. Appl.Therm. Eng. 70 (1), pp. 846–856.
12. Lee, J. J., Jeon, M. S., and Kim, T. S., 2010, "The Influence of Water and Steam Injection on the Performance of a Recuperated Cycle Microturbine for Combined Heat and Power Application," Applied Energy, 87(4), pp. 1307 - 1316.

13. Traverso A., and Massardo A.F., “Thermoeconomic Analysis of Mixed Gas-Steam Cycles”. Applied Thermal Engineering, 22 (2002), pp: 1-21.

14. Stathopoulos, P., and Oliver Paschereit, C., 2016, “Operational Strategies of Wet-Cycle Micro Gas Turbines and Their Economic Evaluation”, J. Eng. Gas Turbines Power 138(12), 122301. Paper No: GTP-15-1289; doi: 10.1115/1.4033999.

15. Stathopoulos, P., Paschereit, C.O., 2015. Retrofitting micro gas turbines for wet operation. A way to increase operational flexibility in distributed CHP plants. Applied Energy 154 (2015) 438–446.

16. Montero Carrero, M., De Paepe, W., Parente, A., Contino, F., 2016. “T100 mGT Converted Into mHAT For Domestic Applications: Economic Analysis Based on Hourly Demand”. Appl. Energy 164, pp: 1019–1027.

17. Parente, J., Traverso, A., Massardo, A.F., 2003. “Micro Humid Air Cycle Part A: Thermodynamic and Technical Aspects”, ASME paper GT-2003-38326.

18. Parente, J., Traverso, A., Massardo, A.F., 2003. “Micro Humid Air Cycle Part B: Thermoeconomic analysis”, ASME Paper 2003-GT-38328.

19. De Paepe, W., Delattin, F., Bram, S., and De Ruyck, J., 2012, "Steam Injection Experiments in a Microturbine – a Thermodynamic Performance Analysis," Applied Energy, 97, pp. 569-576.

20. De Paepe, W., Delattin, F., Bram, S., Contino, F., and De Ruyck, J., 2013. “A Study on the Performance of Steam Injection in a Typical Micro Gas Turbine”. ASME paper GT2013-94569.

21. Ferrari, M. L., Pascenti, M., Traverso, A. N., Massardo, A.F., 2012. “Hybrid System Test Rig: Chemical Composition Emulation With Steam Injection”, Applied Energy 97 (2012), pp: 809–815.

22. Traverso, A., 2010 “Humidification Tower For Humid Air Gas Turbine Cycles: Experimental Analysis”, Energy 35, pp; 894–901.

23. Montero Carrero, M., Ferrari, M.L., Paepe, W.D., Parente, A., Bram, S., and Contino, F., 2015. “Transient Simulations Of A T100 Micro Gas Turbine Converted Into A Micro Humid Air Turbine”. ASME Paper GT2015-43277.

24. Traverso, A., 2005. “TRANSEO Code for the Dynamic Performance Simulation of Micro Gas Turbine Cycles”. ASME Paper GT2005-68101.

25. De Paepe, W., Carrero, M.M., Bram, S., Contino, F. 2017. Advanced humidified gas turbine cycle concepts applied to micro gas turbine applications for optimal waste heat recovery. Energy Procedia 105, pp: 1712 – 1718.

26. Parente, Joao O.S., Traverso, A., Massardo, A.F., 2003, "Saturator Analysis For An Evaporative Gas Turbine Cycle", Applied Thermal Engineering, 23 (10), pp: 1275-1293.

27. Pedemonte, A.A., Traverso, A., Massardo. A.F., 2008. "Experimental Analysis Of Pressurized Humidification Tower For Humid Air Gas Turbine Cycles. Part A: Experimental Campaign", Applied Thermal Engineering, Vol. 28, pp. 1711-1725.

28. Pedemonte, A.A., Traverso, A., Massardo. A.F., 2008. "Experimental Analysis Of Pressurized Humidification Tower For Humid Air Gas Turbine Cycles. Part B: Correlation Of Experimental Data", Applied Thermal Engineering, Vol. 28, pp. 1623-1629.

29. De Paepe, W., Carrero, M.M., Bram, S., Contino, F., 2014, "T100 Micro Gas Turbine Converted To Full Humid Air Operation: Test Rig Evaluation". ASME Paper GT2014-26123.

30. De Paepe, W., Carrero, M.M., Bram, S., Contino, F., 2015, "T100 Micro Gas Turbine Converted To Full Humid Air Operation – A Thermodynamic Performance Analysis". ASME Paper GT2015-43267.

31. Montero Carrero, M., De Paepe, W., Magnusson J., Parente, A., Bram, S., and Contino, F., 2017, "Experimental Characterization of a Micro Humid Air Turbine: Assessment of the Thermodynamic Performance". Applied Thermal Engineering 118, pp: 796-806.

32. Rodgers, C., 2000. "25-5 kWe Micro Turbine Design Aspects". ASME Paper 2000-GT-626, pp: 1–11.

33. Lara-Curzio, E., Trejo, R., More, K., Maziasz, P., and Pint, B., 2004. "Screening and Evaluation of Materials for Micro Turbine Recuperators". ASME paper GT2004-54254, pp. 145–157.

34. Mahmood, M., Martini, A., Traverso, A., Bianchi, E., 2016. "Model Based Diagnostics of AE-T100 Micro Gas Turbine", ASME Paper GT2016-57671.

35. Mahmood, M., Martini, A., Traverso, A., 2017. "Fault Detection Through Model Based Diagnostics of AE-T100 Micro Gas Turbine". ASME Paper GT2017- 64619.

36. De Paepe, W., Contino, F., Delattin, F., Bram, S., and De Ruyck, J., 2014. "New Concept Of Spray Saturation Tower For Micro Humid Air Turbine Applications". Applied Energy, 130, pp. 723–737.

Section 2: Study of Thermal Energy Storage (TES) Systems

4 Dynamic Modeling and Experimental Validation of Sensible Heat Storage

Scope of this chapter is to present the dynamic modelling and experimental validation of a Thermal Energy Storage (TES) system based on sensible heat, with the help of two models: CFD model based on the ANSYS-FLUENT code, and a model based on the TRANSEO simulation tool. The validation of both model results against the experimental data, modelling capability to present the state of charge (SoC) and thermal stratification of the storage are discussed.

4.1 Concentrated Solar Power (CSP) Hybrid Systems

Global climate change, fluctuating prices and restrained supply of conventional fuels urge immediate measures to be taken in order to curtail the greenhouse gas emissions from the fossil fuel fired power plants. The accelerated deployment of Renewable Energy Sources (RES), and adopting new technologies for energy production can help the emerging economies through provision of clean and secure energy supply, without compromising their economic growth [1-3]. Concentrated Solar Power (CSP) is one of the promising and rapidly expanding renewable energy technologies, owing to its features like wide availability, readiness for hybridization and cost effectiveness.

The higher temperatures achievable with CSP systems make them a more attractive technology for hybridization with gas turbines cycles, hence Hybrid Solar Gas Turbine Systems (HSGT) particularly with micro gas turbine have gained great attention for the last

decades[4]. However, turbine modifications are required for steady operation. Dynamic analysis have been performed to overcome the technical challenges and for optimization of solar hybridization schemes of gas turbines. During past few years, several projects in EU, as well asoutside EU focused on the integration of gas turbines with solar energy; their context has been described briefly in the following section:

The **SOLGATE** Project was started in 2002 by ORMAT industries in Spain, where a solar hybrid test system was developed, built and tested. This system consisted of a modified 250 kWe turbine, two pressurized volumetric receivers and one tubular receiver in series (Fig.4-1). The objective of the SOLGATE project was the development of a solar-hybrid power system with direct solar heating of a gas turbine's pressurized air. The overall project aimed to prove the technical feasibility, the potential of electricity cost reduction of such a system and to gain the operational experience required to initiate a demonstration project [5].

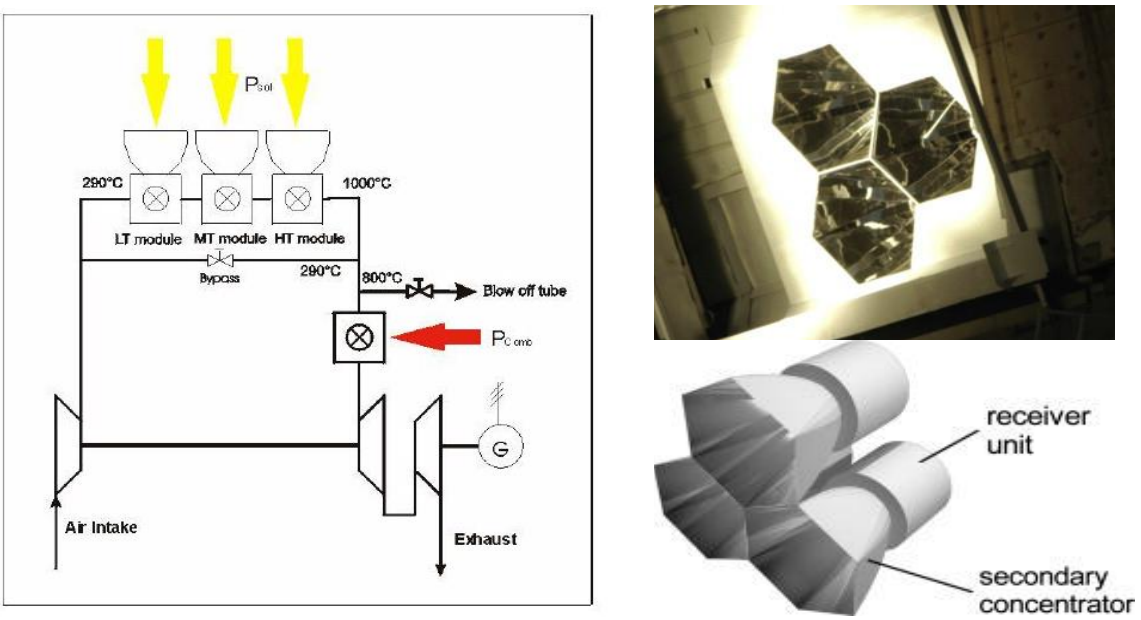

Figure 4-1.The schematic layout of SOLGATE facility (left), honeycomb arrangement of solar receivers (right) [5]

The **OMSoP** project funded by the European Commission, demonstrated the integration of the solar dish and mGT system (Fig.4-2). This project was focused to develop and demonstrate the advanced technical solutions for CSP systems coupled with mGT, to produce

electricity in the range of 3-10 kW. The project work principally involved the development and experimental characterization of the dish component, and the integration of the complete system, leading to a full scale demonstrative plant to be located at the ENEA Casaccia Research Centre, Italy [6].

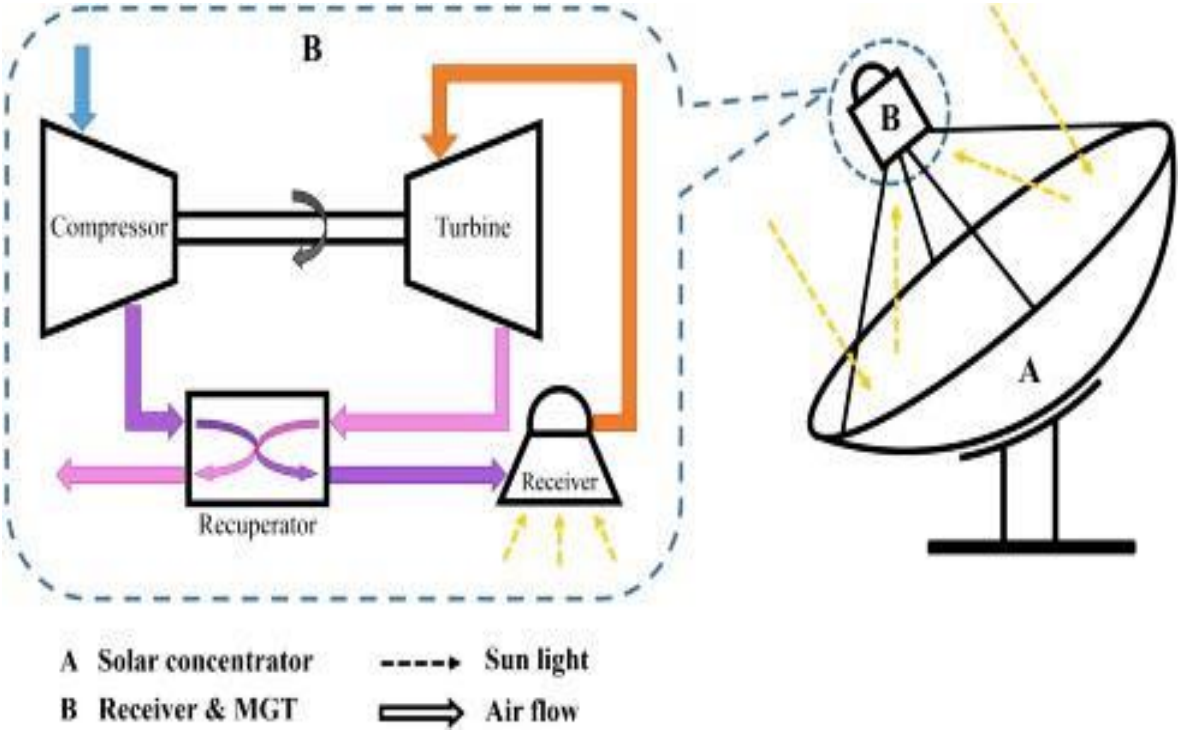

Figure 4-2 The schematic layout of OMSoP test system [6]

The **SOLUGAS** project, first solar hybrid system equipped with a gas turbine at megawatt scale, was commissioned under the European Commission's 7th Framework Programme, in May 2012 in Spain. This involves the demonstration of a solar hybrid power system with direct heating of a gas turbine's pressurized air up to 800 °C (Fig.4-3). A complete solar-hybrid gas turbine demonstration system, heliostat field and tower were built to prove the technical feasibility, performance and potential cost reductions of the technology [7].

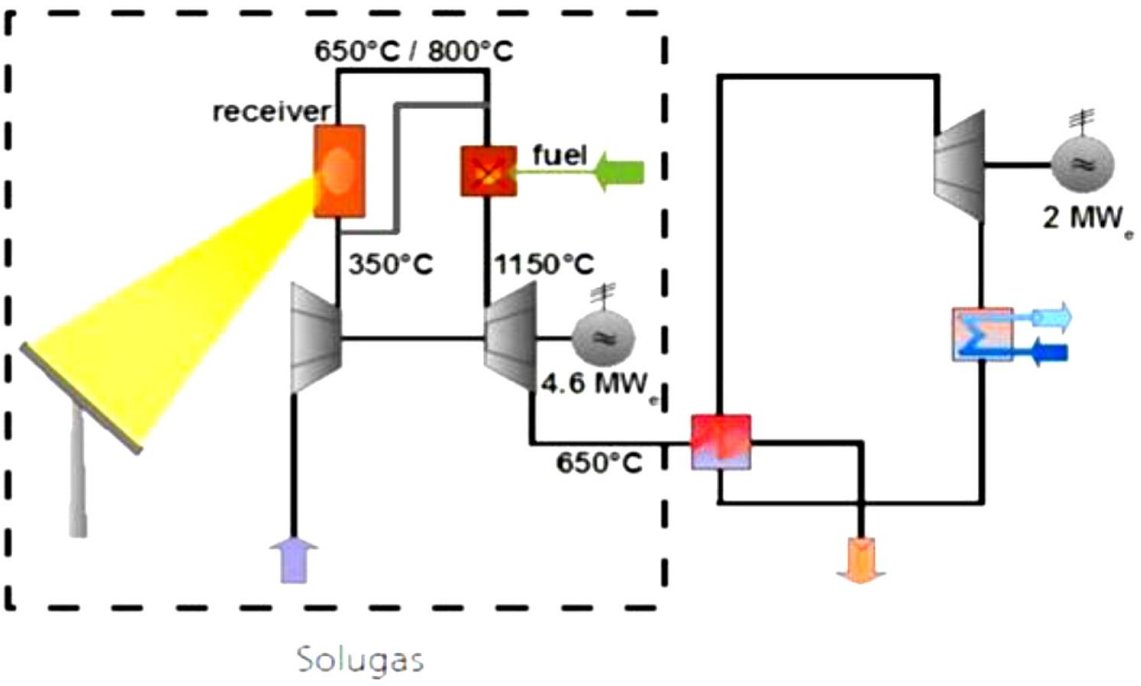

Figure 4-3.The schematic layout of SOLUGAS test system [7]

TULIP solar power plant designed by AORA-Israel is based on the unique Tulip-shaped tower that receives concentrated solar rays reflected from 50 mirrors, and heat air up to 1,000°C (Figure 4-4). This hot pressurized air is directed towards the T100 gas turbine that converts thermal energy to electric energy. Unlike conventional solar thermal systems that use steam to drive large turbines, the Tulip power plant requires only 8% of the amount of water, making it perfect for desert regions. The first AORA power station is operational in Kibbutz Samar-Isreal since 2009, and second demonstration plant is under development in Almeria, Spain [8].

The **PEGASE**, which is R&D project funded by the European Commission's 7th Framework Programme, is aimed at removing the algorithmic barriers related to the monitoring, simulation and optimization of very large power systems. The project has produced powerful algorithms and full-scale prototypes that run the whole European Transmission Network model for state estimation, real time control, dynamic security analysis, and steady state optimization [9].

Figure 4-4. AORA solar TULIP power plant (source: http://www.alternative-energy-news.info/tulip-solar-ethiopia/)

The integration of CSP with other renewables like biomass is also becoming increasingly interesting as low cost option to provide dispatchable renewable energy. A demonstrative plant in Griffith, New South Wales is based on the hybridization of a biomass power plant with a molten salt solar tower system. This hybridization scheme is able to achieve high cycle efficiency as both the steam generators can provide steam at 525°C and 120bar to the steam turbine. This facility has demonstrated the economic benefits compared to a standalone CSP plant [10].

CSP-Geothermal hybrid plants based on the Organic Rankine Cycle (ORC) are also analyzed under thermodynamic and technical aspects. A case study for the retrofit where the ORC module is extended by a solar super -heater and the additional heat input is realized by parabolic trough has been conducted over the period of one year in the Büyük Menderes Graben in Turkey. The results proved the technical feasibility of the selected superheating concept and increased electricity generation up to 4.5 %, compared to the stand-alone geothermal power plant [11].

At present, it can be inferred from the referenced bibliography that technical feasibility of large solar hybrid power plants has been investigated in detail. However, integration of TES in such systems still poses significant challenges.

4.2 Thermal Storage Integration in CSP Systems

Thermal Energy Storage (TES) is a significant technology in the systems involving renewable energies as it can make their operation more efficient, particularly by bridging the gap between energy supply and demand. One of the CSP strengths is the integration of TES, which facilitates the uninterrupted energy production after sunset and during cloudy days. Thus, TES plays an important role in increasing the contribution of CSP in the energy mix of regions and countries. This significantly increases the CSP capacity factor and giving it an edge over solar PV and other renewables. It also enables the dispatchable power generation, which can facilitate both the grid integration and economic competitiveness of CSP power plants [12].

Over the past few decades CSP industry has faced increasing competition from PV industry, as the latter has gained radical cost reductions due to mass production and associated learning curves. Hence, thermal storage integration has become inevitable in order to make the CSP power plants economically viable.

4.2.1 Classification of TES Systems

According to principle of energy storage, there are three main types of TES systems:

- **Sensible heat storage (SHS)**
- **Latent heat storage (LHS)**
- **Thermochemical heat storage (TCS)**

Each of these types presents a sequential process of charge, storage and discharge giving a complete storage cycle as reported in Figure 4-5. During the charging step, external thermal energy is used to heat a fluid or a solid medium (sensible storage), or initiate phase transition (latent storage), or drive an endothermic chemical reaction (thermochemical storage). Then, the medium is stored at the charging step temperature. When this energy is released during discharging step, the medium temperature decreases, or medium phase changes into the first state, or energy is released during the exothermic reaction. (A brief overview of all three energy storage systems have been presented in Chap.1 of this thesis, hence only the sensible heat storage will be discussed in detail in the following section).

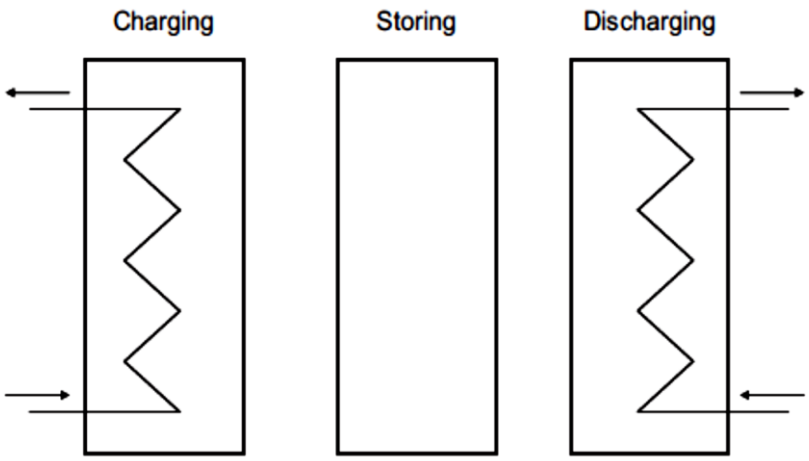

Figure 4-5.TES complete storage cycle

4.2.2 Sensible Heat Storage (SHS) Systems

In sensible heat storage systems (SHSS), thermal energy is stored by raising the temperature of a solid or liquid media, thereby, increasing its energy content. Then, the medium is stored at the charging step temperature. When this energy is released (discharging step), the medium temperature decreases. The sensible heat stored is associated with the increase or decrease of the temperature; hence it is strongly dependent on heat capacity of the medium (C_p). The amount of energy stored is given by the relation:

$$\mathbf{Q} = \int_{\mathbf{T_i}}^{\mathbf{T_f}} \mathbf{m}.\mathbf{C_p}.\Delta\mathbf{T} \qquad (4.1)$$

Where m is mass of the storage material, T_i and T_f are the initial and final temperature of the storage medium, respectively. Examples of materials typically used as a storage medium are water, air, oil, rocks, bricks, concrete, sand and soil. The storage material is usually selected according to its heat capacity and the available space for storage. Gases have very low volumetric heat capacity and therefore are not used for sensible heat or cold storage. Table 4.1 lists some common materials used in SHS.

Table 4.1 Typical materials used in sensible heat storage systems

Material	Density [kg/m3]	Specific heat [J/kg·K]	Volumetric thermal capacity[MJ/m3·K]
Clay	1458	879	1.28
Brick	1800	837	1.51
Sandstone	2200	712	1.57
Wood	700	2390	1.67
Concrete	2000	880	1.76
Glass	2710	837	2.27
Aluminium	2710	896	2.43
Iron	7900	452	3.57
Steel	7840	465	3.68
Gravelly earth	2050	1840	3.77
Magnetite	5177	752	3.89
Water	988	4182	4.17

Water appears to be the best available liquid SHSS because it is cheap and has a high specific heat and volumetric thermal capacity. However above 100 °C, materials such as oils, molten salts and liquid metals are preferred since water should be pressurized. For air heating applications rock or metal bed type storage materials are used.

4.2.3 Comparison of TES Systems

Sensible heat storage represents the simplest and least expensive form of thermal storage. Significant research work has been carried out on SHS systems employing variety of solid materials such as rocks, metals, concrete, ceramics, sand and bricks, and the technology for

their utilisation is well developed. However, in any TES system, storage and recovery of thermal energy must be done efficiently to achieve high capacity factors. For this, TES technologies must meet several requirements: high energy density, good heat transfer between the heat transfer fluid (HTF) and storage media, thermal shock resistance, low cost, and reversibility through multiple charging and discharging cycles.

A quantitatively comparison of the different thermal energy storage technologies is reported in Table 4.2, with reference to relevant performance parameters and factors. It is evident that the various technologies have different operating characteristics, advantages and limitations. Hence, TES integration in CSP systems requires extensive modeling and experimental study to optimize the overall system.

Table 4.2Comparison of different thermal energy storage (TES) systems

	Sensible TES	**Latent TES**	**Thermochemical TES**
Temperature range	Up to:50 °C (Aquifers and ground storage) 110 °C (Water tanks) 300 °C (Sand-rock-mineral oil) 400 °C (Siliconic oil) 400 °C (Concret) 500 °C (NaCl, solid) 700 °C (Cast steel) 1200 °C (Magnesia fire bricks)	-100-0°C (Water-salt solutions) -50-0 °C (Clathrates) -20-100 °C (Paraffins) -20-80 °C (Salt hydrates) 20-450°C (Sugar alcohols) 120-300 °C (Nitrates) 150-400°C (Hydroxides) 350-750 °C (Chlorides) 400-800 °C (Carbonates) 700-900 °C (Fluorides)	180°C (Iron carbonate) 200-300°C (Metal hydrides) 250-400°C (Magnesium oxide) 400-500 °C (Ammonia) 800-900 °C (Calcium carbonate) 500-1000°C(Methane/water) 2000-2500 °C (Metal oxides Zn and Fe)

Energy density Volumetric density Gravimetric density	Small ~ 50 kWh/m^3 of material Small ~ 0.02-0.03 kWh/m^3 of material	Medium ~ 100 kWh/m^3 of material Medium ~ 0.05-1 kWh/m^3 of material	High ~ 500 kWh/m^3 of material High ~ 0.5-1 kWh/m^3 of material
Storage period	Limited (thermal losses)	Limited (thermal losses)	Theoretically unlimited
Lifetime	Long	Often limited due to storage material cycling	Depends on reactant degradation and side reactions
Technology status	Industrial scale	Pilot scale	Laboratory scale
Advantages	Low cost Reliable Simple application with available materials	Medium storage density Small volumes Short distance transport possibility	High storage density Low heat losses (storage at ambient temperature) Long distance transport possibility High compact energy storage
Disadvantages	Significant heat loss over time (depending on level of insulation) Large volume needed	Low heat conductivity Corrosivity of materials Significant heat loss (depending on level of insulation)	High capital costs Technically complex

4.2.4 TES Configurations: Packing Materials vs. Structured Monoliths

In the past decades, different TES configurations like packed beds of spherical particles and monolithic blocks have been extensively investigated by many researchers to examine the effects of several parameters such as void fraction, flow rate variations, thermal losses, particle size, packing material, and fluid inlet temperature on thermal performance of the TES [13, 14]. In general, efficient thermal cycling is linked to the high degree of thermal stratification inside TES, which is affected by the aforementioned system parameters. The thermocline zone in packed beds is prone to mixing in the tank .or degrading after several charging–discharging cycles, hence resulting in higher exergy destruction [15]. The low void fraction (0.3-0.4) in the packed beds leads to high energy storage density, but the pressure drop is also increased, thus resulting in more exergy destruction. Similarly, smaller particle sizes minimize the intra-particle temperature gradients but also lead to a higher pressure drop [16].

On the other hand, structured monoliths and foams have higher void fraction (0.7-0.9) depending on their cpsi (cells per square inch) value. These ceramic monoliths and foams offer several advantages over packed beds such as thin walls, higher gas–solid contact area per unit volume and accommodation of high gas flow rates combined with low pressure drop. These characteristics have led to the significant development of TES systems based on such monoliths. Moreover, scale-up of structured reactors is much easier than of randomly packed beds, slurry reactors and fluidized bed reactors [17], hence they facilitate the TES designing for integration in large power systems.

Thus, due to the technical challenges such as high storage density of packed beds but unacceptable pressure drop at low void fraction in comparison with monoliths and foams, further studies are required to design TES systems based on the packed beds which are capable of high exergy recovery [15].

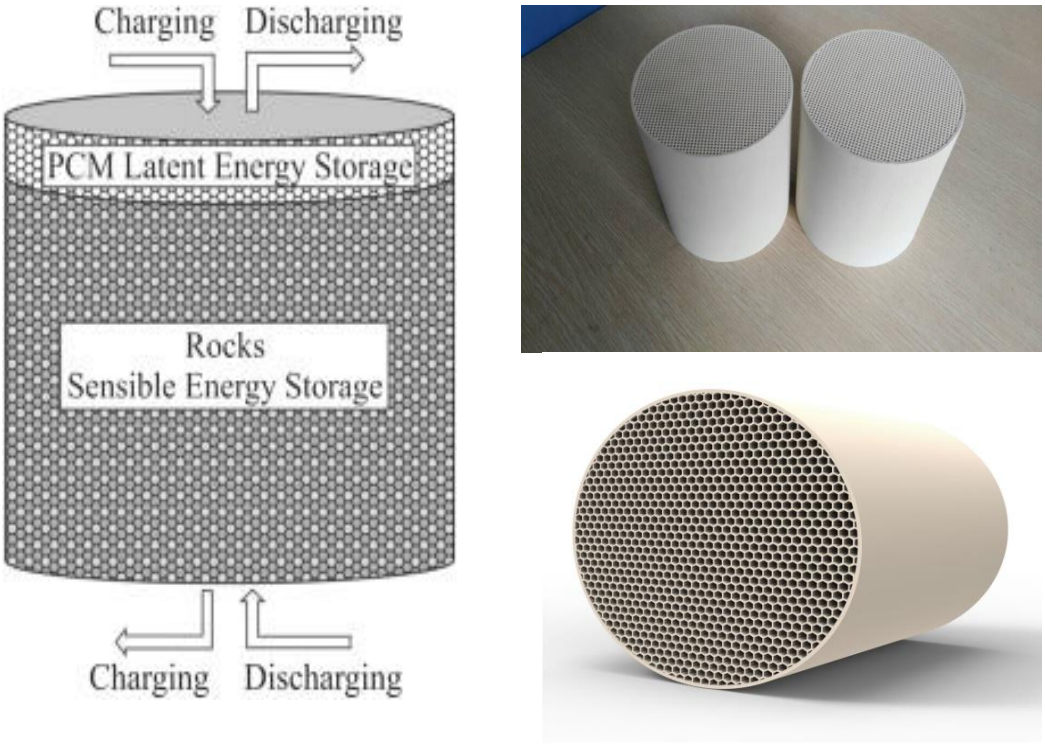

Figure 4-6. TES configurations: Packed bed (right), structured monoliths (left)

4.3 TES Systems Modelling- A Short Review

Since several parameters are associated with the development of TES system, numerical modelling and simulation tools are essential for TES design optimization, efficient charging and discharging, thermal losses control and for understanding the interaction of thermal storage with other components of the plant. Various numerical models are discussed in the following section.

Austin et al. [18] have proposed a control-oriented dynamic model of a thermal energy storage tank with an immersed heat exchanger coil. Based on the space discretization of the storage tank and quasi-steady approach to model the coil dynamics, the resulting model is well-suited for the model-based control design and real-time simulation of TES systems.

Zhen Yang et al. [19] have simulated the cyclic operation of the thermocline storage, operating with a commercially available molten salt as the heat transfer fluid and quartzite rock as the filler. Based on the finite-volume approach and Brinkman–Forchheimer extension

of the Darcy law, the developed model has been successfully validated and afterwards used to optimize the thermocline systems of different power capacities.

Grange et al. [4] have developed a simulation tool to highlight the impact of TES operating conditions on the performance of combustion chamber and hence, on overall HSGT performance. This study highlighted that a major advantage of the storage is stabilizing the air temperature at the combustion chamber inlet, in order to keep the operating conditions of the combustion chamber close to the design point.

A numerical model of high temperature rock bed thermal storage system was formulated by Zanganah et al. [20], with air as HTF at temperature range of 20-650oC. The model accounted the impact of temperature dependant thermo-physical properties on thermal behaviour of the rock bed. Avila et al. [22] have developed a numerical model for a high temperature regenerative TES for CSP plants based on the air cooled receivers, and validated against the experimental data from a lab scale test facility. The work was focused on performance analysis of four types of commercially available alumina spheres, up to the temperature of 640°C.

Klein et.al [21] has analysed a pressurised storage system that utilises a packed bed of alumina spheres as the storage medium and air from the gas turbine cycle as the heat transfer fluid (Fig 4-7). A detailed model of the storage system is developed that accountsfor transient heat transfer between discrete fluid and solid phases. The model includes all relevant convective, conductive and radiative heat transfer mechanisms and is validated against high temperature experimental data from a laboratory scale test facility. The validated model is further utilised to conduct a parametric design study of a nominal six hour TES for micro-gas turbine. The concepts of utilisation factor and storage efficiency are introduced to determine the optimal storage design.

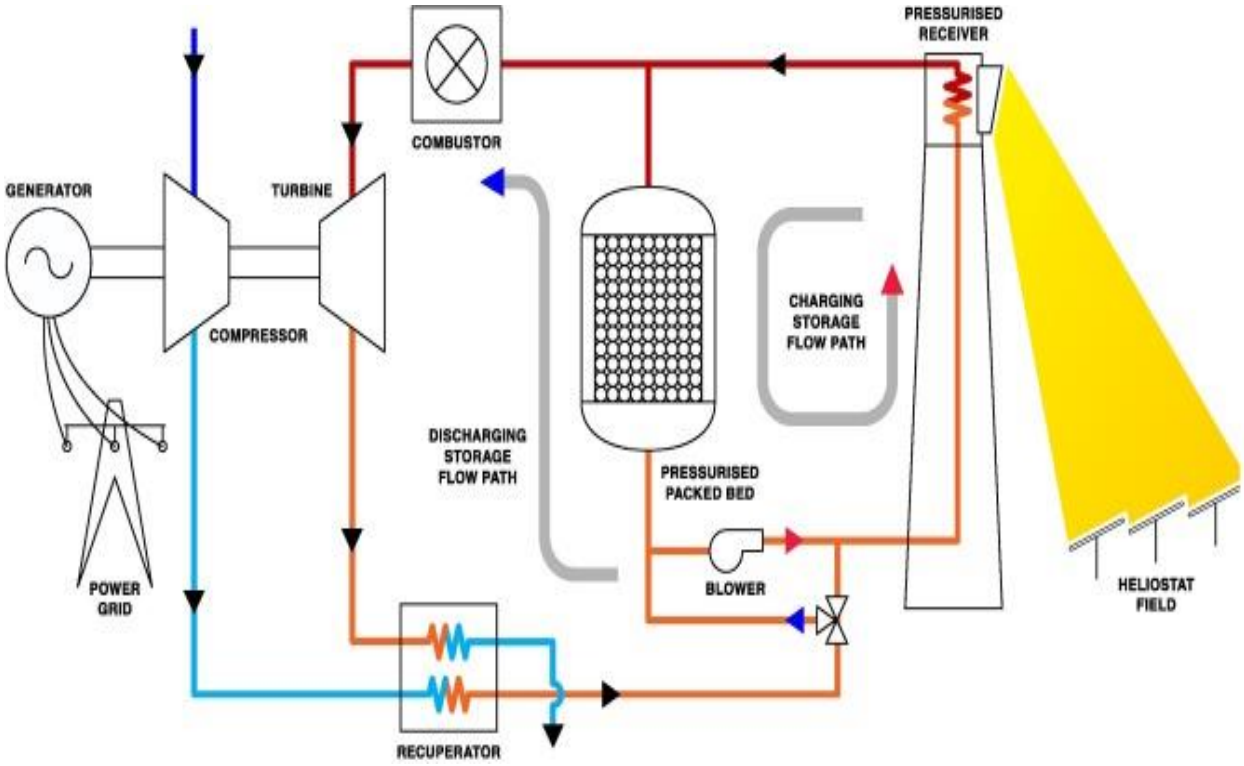

Figure 4-7. Schematic of gas micro-turbine cycle with thermal storage.

Cascetta et al. [22] have analysed the thermal behaviour of a packed bed sensible storage system consisting of a solid material of high thermal capacity: alumina, and using different HTFs: air, molten salt and oil (Fig.4-8). The work was focused on the numerical investigation of the transient thermal behaviour and evaluating the progressive reduction of stored energy, after consecutive charge/discharge cycles.

In the next study, authors have presented the comparison between CFD simulations and experimental results, obtained from the same storage system and using air as HTF. CFD model consisted of an axisymmetric cylindrical tank filled with the porous alumina bed. The model accounted for variable porosity of the alumina beads in radial direction, temperature-dependant thermodynamic properties of both phases and effective thermal conductivity. Numerical results have been validated against the experimental data obtained from the test rig at the University of Cagliari [23].

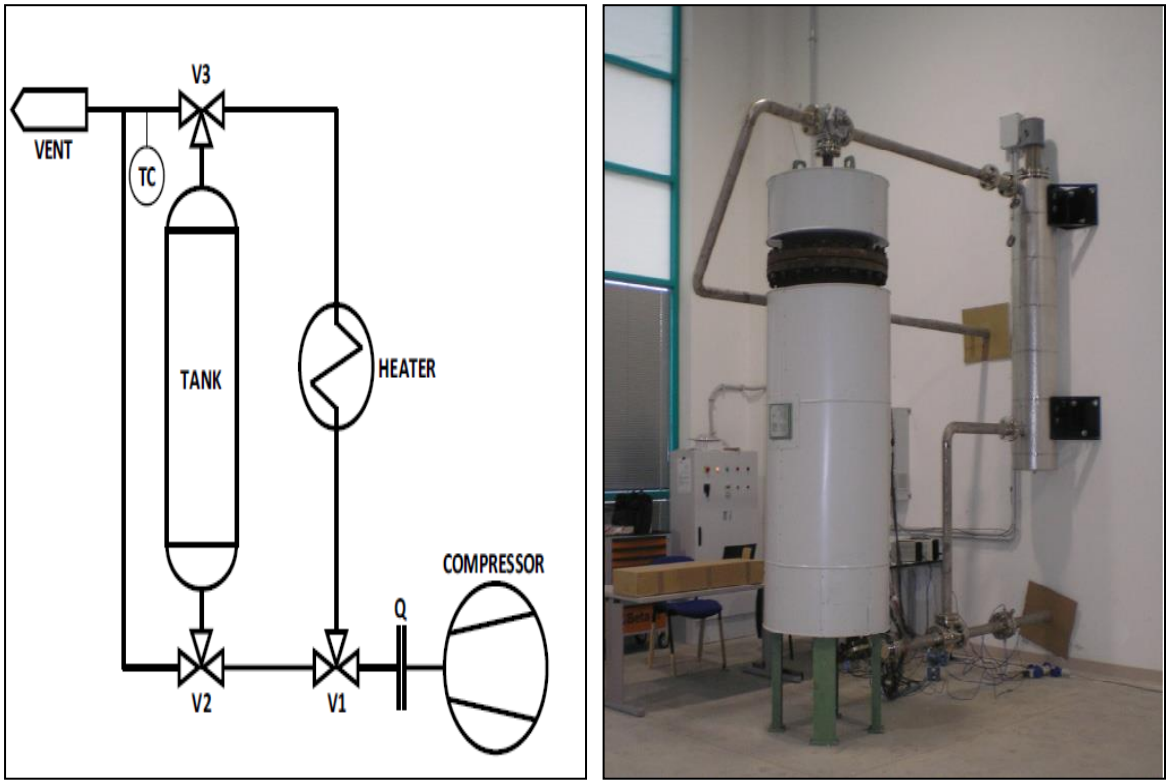

Figure 4-8.Schematic layout (left) and Laboratory test rig (right) at the University of Cagliari [23]

In view of this literature survey, we can understand that numerical analysis as well as experimental investigation of the packed bed TES systems has been the research focus during the past decades, while use of the monolithic structures for TES applications is still under development.

4.4 Hybrid Solar Gas Turbine (HSGT) System with TES Integration- A Demonstration Facility

The Thermochemical Power Group (TPG) of the University of Genoa, Italy, has developed an experimental facility of HSGT system, which is based on mGT-solar hybridization (CSP) with TES integration. The following sections briefly describe the system layout of this HSGT facility and the experimental work.

4.4.1 Experimental Setup of HSGT System

This small-scale demonstration facility has been designed and constructed by TPG, at the SAVONA campus of University of Genova. Fig.4-9 shows the TURBEC T100 mGT which is modified to integrate with CSP system and energy storage. Before the practical realization, detailed dynamic analysis has also been performed with the help of TRANSEO simulation tool [24, 25] to analyse the impact of pressure drops on the gas turbine flow balance due to the Solar Gas Turbine Upgrade (SGTU) system i.e. the overall CSP-TES system [26, 27]. For complete demonstration of HSGT cycle, this system will be integrated with a TURBEC T100 mGT plant in future.

In the present setup (Fig.4-10) air is provided by an external compressor ($C_{external}$), and the solar input is physically emulated with electric heaters (CRS). Compressed air is delivered to the SGTU through valve 1. One regulating three-way valve 2 and one on/off three-way valve 3 are used to change between five plant operating modes; bypass SGTU, TES bypass, pilot charging, pilot discharging, and full discharge. Pressurized air coming from the compressor outlet is led by the three-way valve 2 (the only mid-temperature regulating valve) through the CRS, where it is heated by the collected solar radiance. The heated air then proceeds to the combustion chamber through the high temperature orifice ($T_{orifice}$): a calibrated flange that can be set with a desired pressure drop.

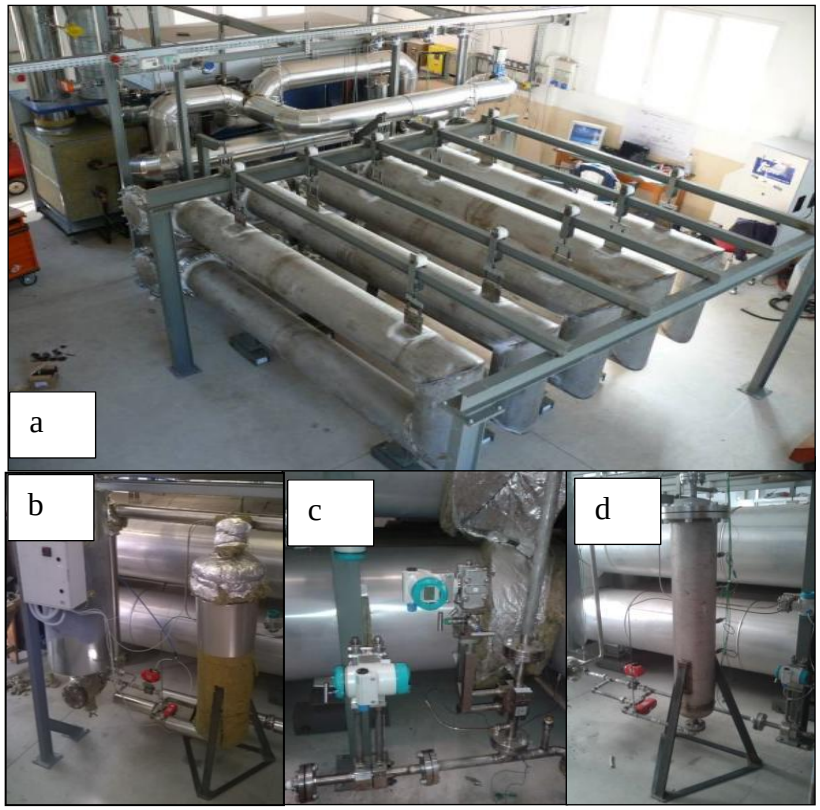

Figure 4-9.. The micro gas turbine test rig being modified for solar hybridization and storage (a), CRS and TES (b), pressure sensors(c), TES vessel with thermocouples (d)

The TES charging (Fig.4-10 – green arrows) begins when excess solar heat is available; the three-way valve 3 (on/off valve) is opened to split the flow stream through TES and the Torifice. The TES is considered charged when the temperature at valve 3 overcomes a given threshold. When solar power is limited, the CRS can be supplemented with stored thermal energy by reversing the flow through the TES, which is done by throttling valve 2 and switching valve 3. In full discharging mode (Fig.4-10 – red arrows), the CRS is bypassed and all air goes throughout the TES, to preheat the compressed air prior to the combustor inlet.

The three-way valves are exposed to the compressor outlet temperature; hence low cost materials can be employed. The full charged TES establishes a thermal gradient from top to bottom, reaching up to 800-900°C on the top, while at the bottom it maintains the temperature close to the compressor exit temperature. In this respect, the bottom part of Fig. 2, between the compressor and the combustor, is referred to the "cold side" of the plant, while the top part is called the “hot side”. Hence, this HSGT system avoids the use of high

temperature valves (800-900°C) in hot side of the plant, to ensure reliability and low costs. A detailed description of the system and control strategy of the storage for charging and discharging phases, have been explained in [28].

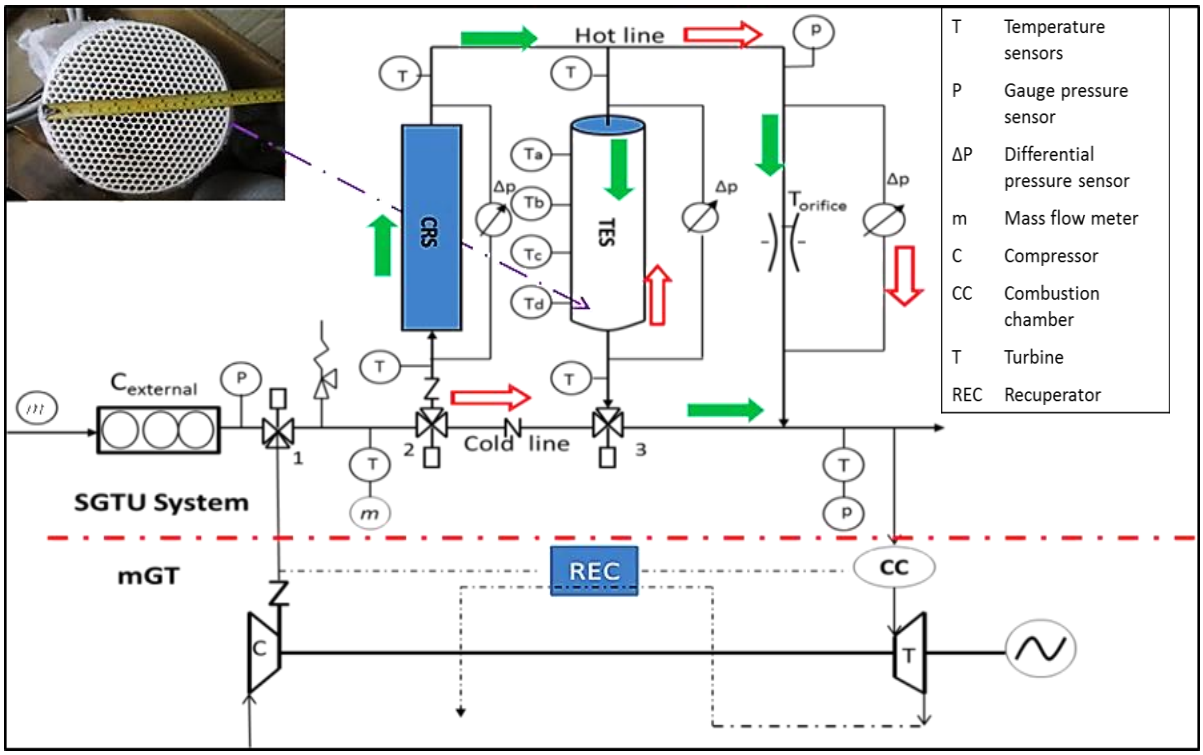

Figure 4-10.Schematics of the CSP TES test rig: charging (green arrows) / discharging (red arrows) phases. Detail of the honeycomb ceramic modules (top left)

4.4.2 Thermal Energy Storage (TES)

Thermal energy storage (TES) system, which is a part of the above HSGT system, is based on sensible heat storage mechanism. The TES is composed of five ceramic monoliths stacked together to constitute the storage column, which is enclosed in a steel vessel and insulated by rock wool insulation to minimize the ambient heat losses. These monoliths are made of Mullite ceramics. Each monolith has very small holes/channels, which make the honeycomb structure (Fig.4-11).

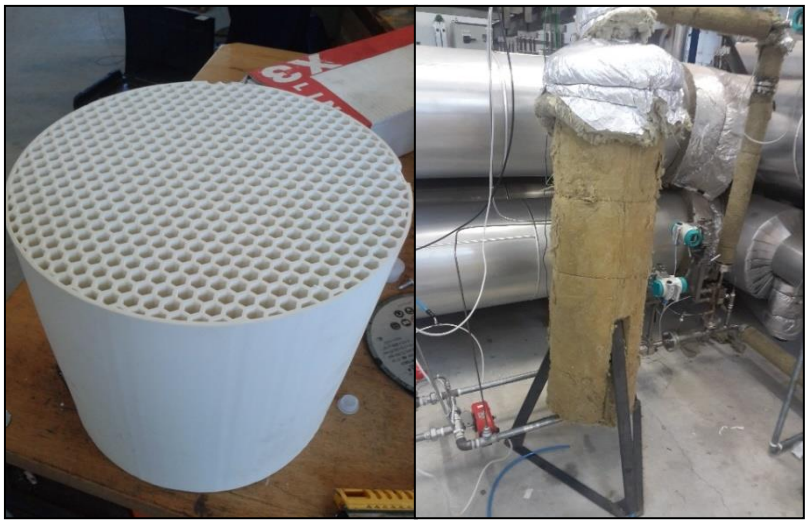

Figure 4-11. Ceramic module for TES (right), Insulated TES vessel (left)

For experimental characterization of the TES, four thermocouples were placed inside the storage after the first, second, third and fourth ceramic module to record the intermediate axial temperatures Ta, Tb, Tc, and Td, respectively (Fig.4-12). All the four thermocouples are equally spaced from each other, and each probe is inserted up to the middle of the storage vessel. Two thermocouples at each end of the vessel (i.e before the first module and after the fifth module) record the inlet and outlet air temperatures, Tin and Tout respectively, depending upon the charging and discharging phase. The storage material properties and design specifications are presented in Table 4.3.

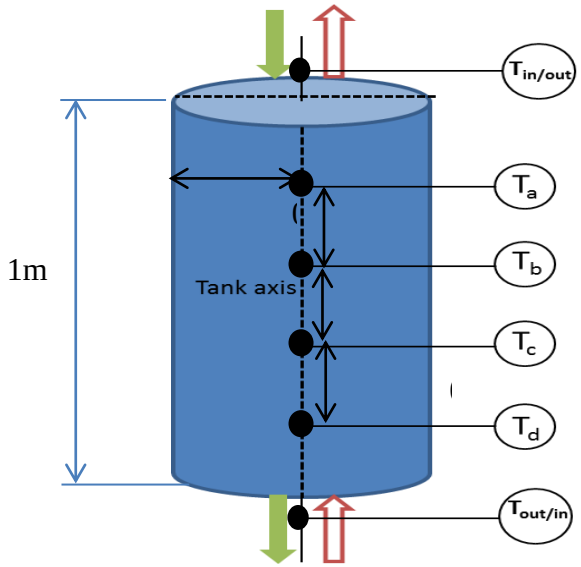

Figure 4-12.Schematic of TES vessel with thermocouples position: charging (green arrows), discharging (red arrows)

Table 4.3Thermal storage data

Parameter	Measure
Ceramic module height [m]	0.2
Ceramic module diameter [m]	0.2
Number of ceramic modules	5
Number of holes in each module	1068
Hole equivalent diameter [m]	0.005
Ceramic mass [kg]	15
Density of ceramics (g/cm3)	3.20
Void fraction of ceramic monolith	0.85
Vessel steel mass [kg]	140
Steel wall thickness [m]	0.04
Insulation thickness [m]	0.2

4.4.3 Instrumentation in HSGT System

The following sensors have been used in the experimental analysis:

- Thermocouples for the higher temperature section (hot line operating at 650°C to 900°C).
- Thermoresistances (RTD) for the cold section of the plant (cold line operating at 250°C to 400°C).
- Two types of pressure probes: one to measure the gauge pressure (p) at a particular station and the second to measure the differential pressure (Δp) between two stations, as shown in Figure.4-9.

Table 4.4. Type k Thermocouples (COMECO Control and Measurement Inc. http://www.comecogroup.com)

Sensor type	**Type 'K' (Nickel Chromium/Nickel Aluminium).**
Construction	Flexible mineral insulated probe with 310 stainless steel sheath
Element/hot junction	Single element, hot junction insulated from sheath in order to prevent electrical noise and interference.

Temperature range	-40°C to +1100°C
Tolerance	In accordance with IEC 584-1&2. Class 1 tolerance: ± 1.5°C (-40 to 375°C); ±0.004 *|T| (375 to 1000°C).

Table 4.5. RTD PT 100(COMECO Control and Measurement Inc. http://www.comecogroup.com)

Sensor type	**RTD PT 100Ω -Class B with compact mineral isolation**
Sheath Composition	AlSl 316
Element/Hot Junction	Single element PT 100 Ω at 0°C class B precision
Temperature Range	-50°C to +500°C
Tolerance	In accordance with IEC-751 class B: ± (0.3 + 0.005*|T|) °C.

Table 4.6. Pressure Sensor Siemens SITRANS-P (SITRANS Pressure transmitters-SIEMENS

Sensor type	**Pressure Sensor Siemens SITRANS**
Measuring range	1 mbar to 400 bar
Measuring accuracy	In accordance with EN 60770-1: 0.075%
Ambient temperature influence	≤ 0.3 %
Temperature of measured medium	–40°C to +100°C
Power supply influence	In percent per change in voltage: 0.005 % per 1 V.

4.4.4 Uncertainty in Measurements

Important parameters in the present HSGT facility include temperature, mass flow rate, absolute and differential pressures. Mass flow rate is measured indirectly from the differential pressure sensors and considering the empirical coefficients associated to the specific probe [28]. Hence, uncertainty in mass flow depends on the measuring accuracy of the differential pressure sensors (which has been mentioned in Table 4.6), and specifications of the probe. The final uncertainty in the mass flow rate is ±1.5%, in the experimental tests reported here.

Since the present study is focused on thermal analysis of the TES, the uncertainty related to temperature measurements is discussed in detail:

- Measuring accuracy/tolerance of the sensors always introduces some uncertainty in the measured values. These are reported in Tables 4.4-4.6.
- Since storage medium and heat transfer fluid in TES are not at thermal equilibrium at any instant during charging and discharging phases, a finite temperature difference exists between solid and fluid phase. Apart from the sensor inaccuracy, there is an uncertainty in the temperature measurement associated with the thermocouples' positions inside the storage vessel. Since ceramic modules have very little pore diameter (around 5 mm), the thermocouple probe is assumed to be in direct contact with ceramic solid surface, and therefore to represent the solid temperature.

In order to confirm this, we have compared the experimental temperature with simulated (air and solid) temperature, from both CFD and TRANSEO models. Figure 4 shows the difference between air and solid temperatures in simulation during the charging phase. In particular, in the second part of the transient (marked by vertical lines in Fig. 4-13), the experimental values are steadily below the simulated ones (both CFD and TRANSEO models), and much closer to the simulated solid temperatures rather than air temperatures: therefore experimental results can be considered representative of the solid temperatures.

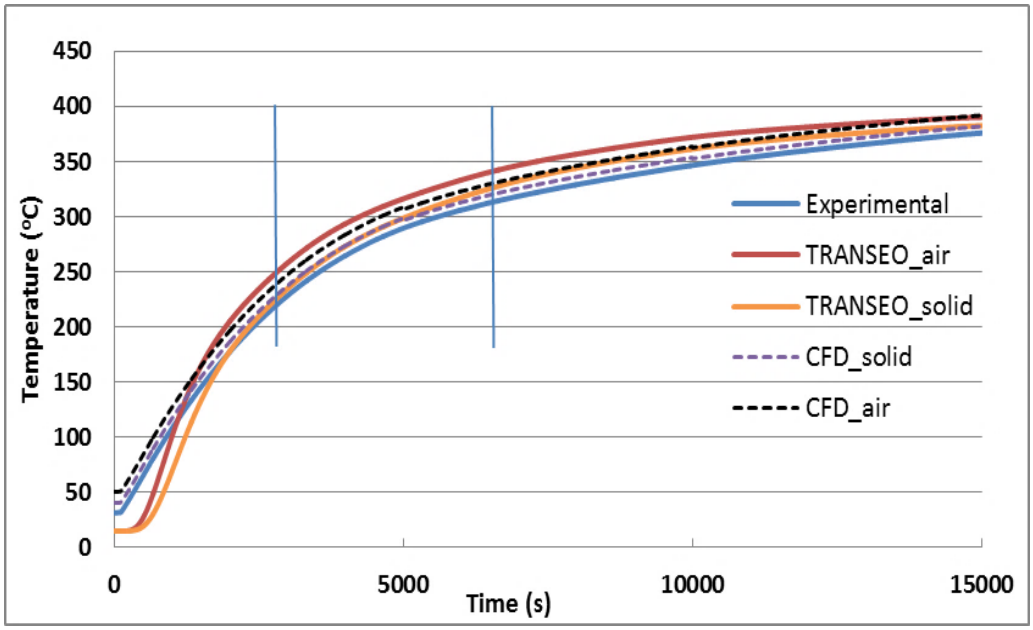

Figure 4-13. Experimental and simulated temperature profile in the middle of TES

- Ideal conditions assume the storage to be at ambient temperature without thermal stratification prior to the charging phase. However, due to previous experimental activity on the TES some heat is retained by the ceramics for a significant period of time. This already existing temperature gradient might have some impact on the results of subsequent test conducted on the same system.

4.4.5 Experimental results of TES

Several experimental investigations have been carried out on the SGTU test rig under different mass flow rates (2-10 g/s), with the aim of analysing the overall pressure drop and thermal behaviour of the TES. Each test consists of a continuous charging phase followed by a discharging phase. The TES is considered completely charged when temperature at the bottom of vessel reaches 250°C in order to maintain a margin of safety, considering the characteristics of the pipe materials. In a discharging phase flow direction is obviously reversed. Control strategy adopted for the charging and discharging phases, overall pressure drop analysis in the SGTU and temperature results have been discussed in detail by Barberis et al. [28]. Keeping in mind scope of this chapter, experimental results of the TES temperature profiles for 10g\s will be discussed briefly in the following sections, while temperature profiles for reduced mass flow rate i.e 5g\s will be discussed in detail in section 4.5.1.3 of this chapter.

The experimental results of charging at nominal flow rate of 10 g/s (Fig.4.14) show that ceramic modules take almost half time to achieve the same temperature in comparison with test at reduced flow rate of 5g/s (Fig.4-18-solid lines). At nominal flow rate, TES maintains thermal stratification for shorter time periods in comparison with test at 5g/s.

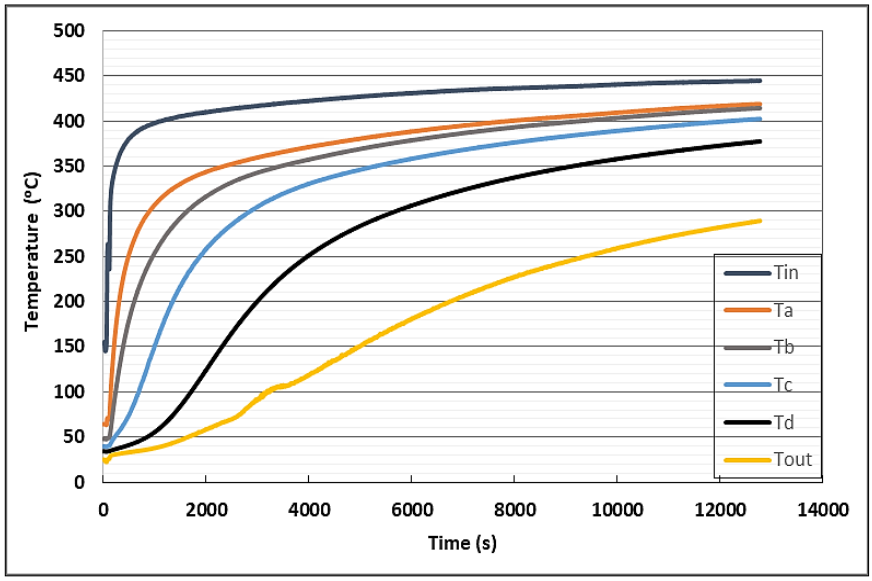

Figure 4-14. TES charging at nominal flow rate (10g/s)

Similar time scale was considered for the discharge phase of the TES (Fig.4-15). During this phase, TES temperatures drop more quickly particularly the bottom ones i.e Tc and Td, in comparison with discharging at 5g/s (Fig.4-20-solid lines).

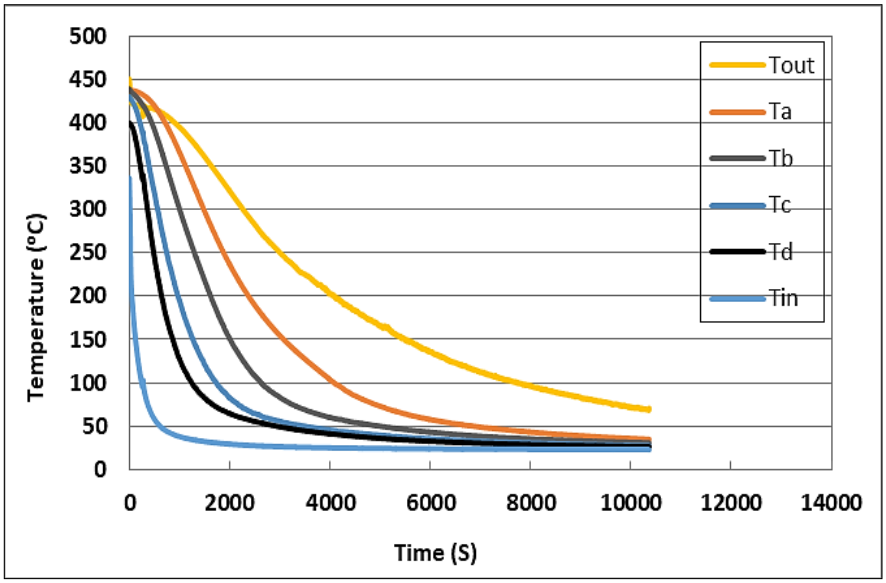

Figure 4-15.TES discharging at nominal flow rate (10g/s)

In [28] study Authors have analysed the overall pressure drops in SGTU system during charging and discharging of the TES for different mass flow rates. This study has concluded that most significant pressure drop is the one related to the high temperature orifice ($T_{orifice}$ in Fig.4-10) in the whole SGTU system, depending on the temperature and mass flow rate. Since the present work is based on the thermal analysis of TES, the pressure drop across the TES during charging and discharging only at 5g/s flow rate has been presented (Fig.4-16).

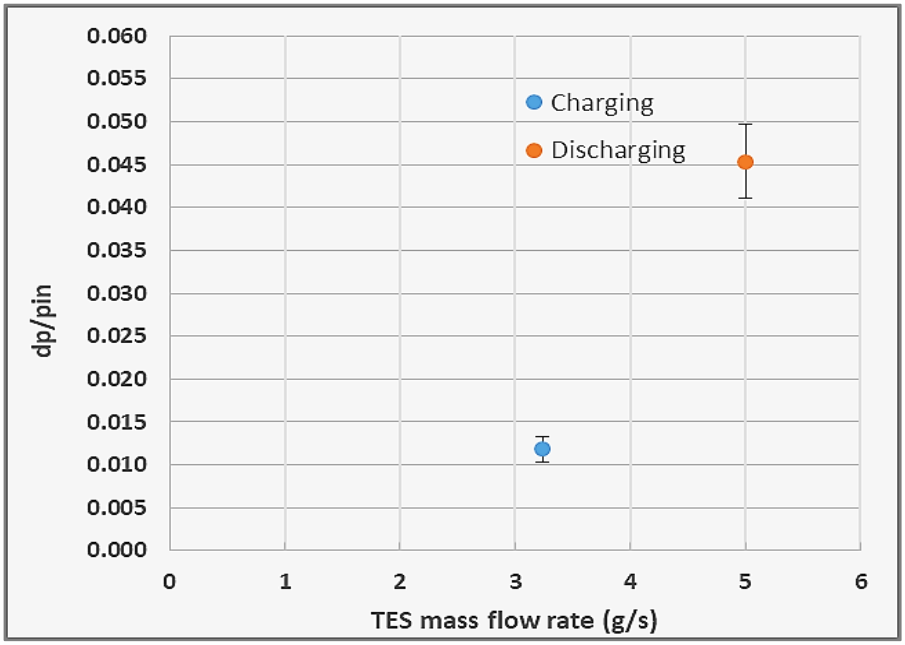

Figure 4-16. TES Pressure drop ratio with respect to inlet pressure during charging and discharging

These experimental results show that pressure drop across the TES (dp) with respect to the inlet pressure (p_{in}), is 0.011 and 0.044, during charging and discharging, respectively. During the charging phase, the total flow stream from CRS is split between the $T_{orifice}$ and TES (as shown by green arrows in Fig.4-10) hence, less pressure drop occurs through the TES. On the contrary, in case of discharging, the whole flow stream enters the TES (red arrows in Fig.4-10); hence higher pressure drop occurs in the TES. The standard deviation of 0.001 and 0.004 in pressure drop during the charging and discharging phase, respectively (shown by error bars in Fig 4-16.) indicate the reliability of experimental results. The mass flow split ratio has been mentioned in the previous study conducted by Barberis *et.al* [28].

However, due to high void fraction (0.85) and smooth channels of the ceramic monoliths, the overall pressure drop across the TES is very low and acceptable for the whole HSGTsystem.

4.5 Dynamic Modelling and Experimental Validation of TES

In this work, TES is modeled by two different approaches: CFD model using the commercial tool ANSYS-FLUENT® and lumped-volume model using TRANSEO, an original simulation tool developed by TPG [24,25]: afterwards both models are compared against the experimental data obtained here for validation.

4.5.1 TES CFD Model

With the aim of evaluating the thermal gradient both in axial and radial directions under charge/discharge conditions, the ceramic TES system has been modelled by means of transient CFD analysis. The Reynolds-Averaged Navier–Stokes (RANS) equations were solved using the commercial CFD software FLUENT, modelling with k-ε (RNG) turbulence model.

4.5.1.1 The computational domain

The geometry considered in the computation is a 2D axisymmetric cylinder, which is divided into two domains: solid domain which consists of steel wall and insulation layer outside the vessel, while fluid domain is the main flow path inside the vessel constituted of ceramics (Fig. 4-17). The entire domain was discretised with a unstructured grid of 2,810,62 *hexa, tri, and quad* elements, with the element size of 5mm.

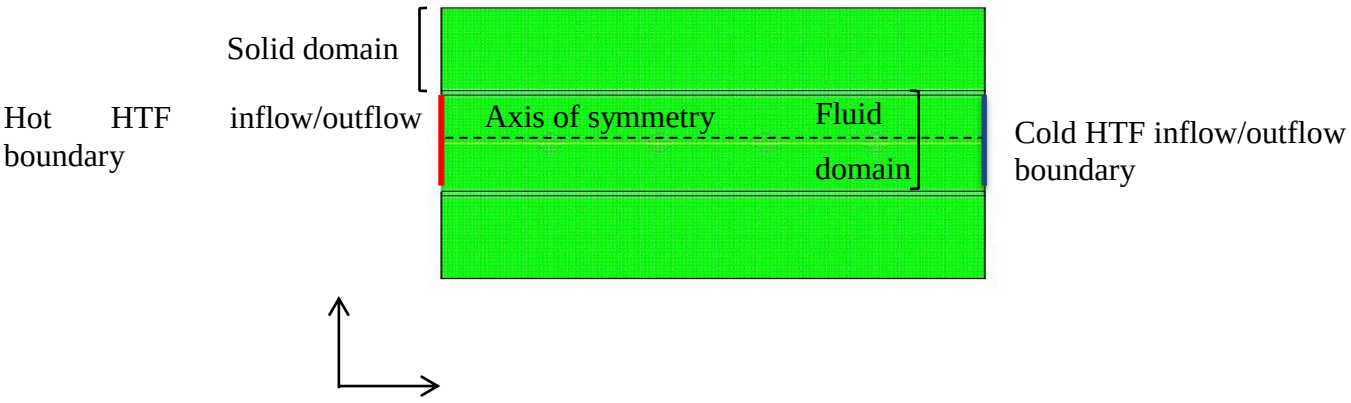

Figure 4-17.The Mesh: 2D axisymmetric model, hot HTF inflow/outflow (red boundary), cold HTF outflow/inflow (blue boundary), Axis of symmetry (dotted line)

The fluid flow is considered incompressible (due to low velocity inside the TES Mach number is lower than 0.3) and thermo-physical properties of the fluid and solid are considered temperature dependent [23], since this factor is important for high temperature storage systems [18]. These are assigned as polynomial interpolations of data available in the literature [29-31]. Reynolds number for the TES varies between 197 at 2 g/s to 944 at 10 g/s, which indicate laminar flow through the TES channels. Porosity is considered constant along the radial direction of the TES column. Table 5 presents thermo-physical properties of the materials involved and heat transfer parameters used for modelling.

4.5.1.2 Modeling approach

The governing equations are based on the unsteady RANS equations which consist of the conservation equations of mass, momentum and energy. Complete simulation of each channel of the ceramic modules with the adjacent thin walls requires a very fine mesh resolution and substantial computational effort, which is out of the scope of this study. Thus, the ceramic zone is modelled as a continuum porous medium exploiting the porous model approach in the Fluent. With this strategy, the porous medium is characterized by the addition of momentum source term to the standard fluid flow equation. This source term takes into account viscous and inertial momentum dissipation due to the flow resistance offered by the porous medium, which for the simplest case of homogeneous porous media is [32-34]:

$$\boldsymbol{S_i} = -\left[\frac{\boldsymbol{\mu}}{\boldsymbol{\alpha}}\boldsymbol{v_i} + \boldsymbol{C_2}\frac{\mathbf{1}}{\mathbf{2}}\,\boldsymbol{\rho}|\boldsymbol{v}|\boldsymbol{v_i}\right] \qquad (4.1)$$

The viscous resistance coefficient 1/α or D (also known as “Darcy term”) and an inertial resistance coefficient C_2 have been derived based on the experimental data available for pressure drop against velocity through the TES [35], and the inertial resistance coefficient has been neglected due to laminar flow. Since a finite temperature difference exists between solid and fluid phases, separate energy equations are needed to solve for each phase. Hence, heat transfer in porous medium has been modelled with Local Thermal Non-Equilibrium (LTNE) model, solving energy equation for the fluid and solid phase (Eq.4.2 and Eq 4.3, respectively) [36].

$$\boldsymbol{\varepsilon(\rho C_P)_f}\frac{\boldsymbol{\partial T_f}}{\boldsymbol{\partial t}} + \left(\boldsymbol{\rho}\mathrm{C}_{\boldsymbol{p}}\right)_{\boldsymbol{f}}.\boldsymbol{u}.\boldsymbol{\nabla T_f} = \boldsymbol{\nabla}\left(\boldsymbol{k_{eff}}\boldsymbol{\nabla T_f}\right) + \boldsymbol{h\alpha_{fs}}\left(\boldsymbol{T_s} - \boldsymbol{T_f}\right) \qquad (4.2)$$

$$(\mathbf{1}-\boldsymbol{\varepsilon}).(\boldsymbol{\rho C_P})_s \frac{\partial T_s}{\partial t} = \nabla\left(k_{eff}\nabla T_s\right) - h\alpha_{fs}(T_s - T_f) \quad (4.3)$$

The empirical correlation of the convective heat transfer for laminar flow is given by Mills [37]:

$$Nu = 3.66 + \frac{0.065.Re.Pr.D/L}{1+0.04\,(Re.Pr.D/L)^{2/3}} \quad (4.4)$$

The overall effective thermal conductivity in the porous medium has been computed by standard approach in the ANSYS-FLUENT considering the fluid conductivity k_f and the solid conductivity k_s:

$$k_{eff} = \varepsilon k_f + (1-\varepsilon)k_s \quad (4.5)$$

Since inlet temperature of the HTF is time-dependent during both charging and discharging, additional User Defined Functions (UDFs) for inlet temperature from the experimental data have been designed and compiled into the CFD code during both phases (Annex-1). Initially, all the domains are set to a constant temperature close to the ambient, to correspond to the initial charge. The temperature distribution at the end of charging phase is used as initial condition for the following discharging phase, where the flow direction is reversed. The internal walls have been modeled by means of conjugate heat transfer approach with meshed wall thickness. This ensures the simultaneous simulation of convection heat transfer from the fluid and conduction heat transfer on the solid; this two heat transfer mechanism creates a coupled effect [38]. Thermal energy losses by means of convection from the external wall towards the environment were also accounted for. A second order upwind scheme was used for the spatial discretization of the convective fluxes, as well as the transient one with a second-order implicit formulation.

4.5.1.3 TES CFD Model Results and Validation

The test case used as reference for CFD model validation is the test conducted at above TES in the HSGT facility, with total mass flow rate of 5g/s.

Charging phase: Figure.4-18 shows the experimental measurements (solid lines) along with the CFD simulation results (dashed lines) during charging phase. Results are presented in terms of temperature distribution inside the ceramics i.e Ta, Tb, Tc, and Td from top to

bottom and outlet air temperature (see Fig.4-12). It can be observed that overall simulated temperatures are slightly higher than experimental ones at any instant of the charging phase. This can be partially justified by the ideal material properties assumed for the TES modelling: ceramic heat capacity and thermal conductivity might not be exactly the same as in the actual storage vessel (as actual material specifications were not available). Secondly, the empirical value of the heat transfer coefficient may not be precise enough for the actual honeycomb ceramics. Finally, the convective heat transfer coefficient is considered to be a constant, neglecting the changes of temperature.

In general simulation result close to the bottom of the storage, i.e T_d, is slightly more accurate in comparison with other axial locations. This can be due to the impact of overall high thermal capacitance and heat exchanging surface. Hence, temperature close to the bottom of the storage is well predicted by the model. This behaviour can be explained by the example of a thermal storage system of infinite length: temperature close to the outlet is constant and can be easily predicted by a model, which, in contrast, can show discrepancies in predicting the internal temperature distribution, especially where temperature gradients are higher.

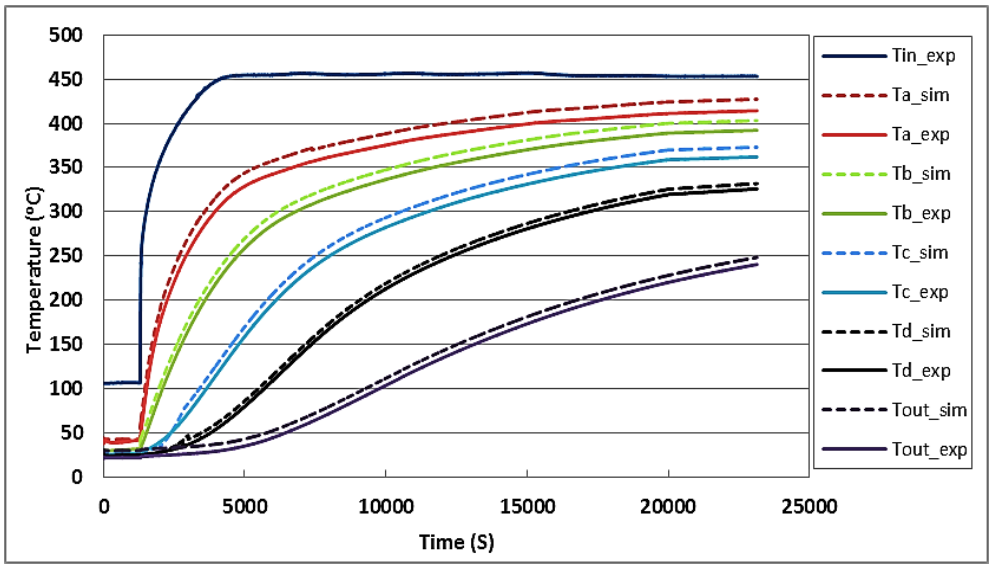

Figure 4-18.Temperature variation at different axial positions of the storage during charging

Despite of some minor differences already clarified: generally simulation results are in close agreement with the experimental results and reasonably describe the temperature gradient of the TES device. The CFD simulations results are also presented in terms of

temperature contours of the storage medium at different intervals of the charging (Fig. 4-19). Starting from a uniform temperature distribution, the thermocline zone can be clearly observed along the length of TES column, and penetrates more towards the bottom as charging proceeds. When charging is complete, nearly the first half of the storage from the top is fully charged and the temperature gradient is observed only in the last half section of the storage. Influence of the wall on the thermal behaviour of the storage is also evident, highlighted by the radial temperature gradient.

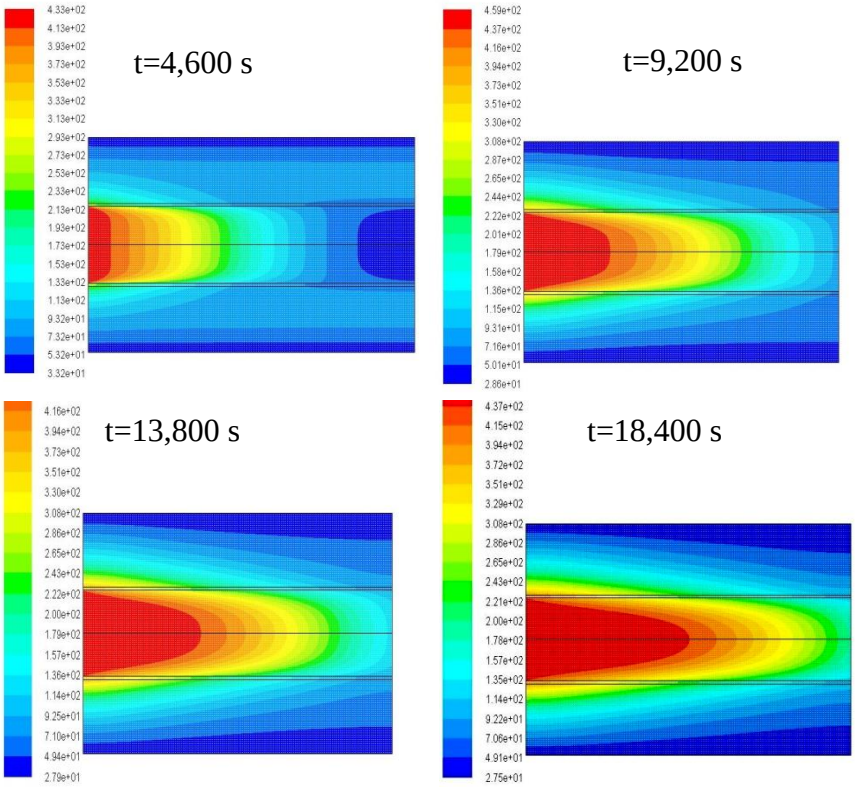

Figure 4-19.Static temperature contours (°C) at different intervals of charging Phase

Discharging phase: During the discharging phase, flow direction is reversed and it starts from the last stage of the charging phase. Similar to the charging phase, inlet temperature of the HTF is time dependent and equal to the experimental values. Fig.4-20 shows the axial temperature distribution during the discharging phase. We can see that after the initial transient phase, simulated inner temperatures of the storage are higher than experimental results. This might be due to the fact that after the initial transient, the thermal inertia of the wall has more influence in the model than the experiment; hence experimental temperatures

drop more quickly than the simulated ones. However, it is evident that simulation results of the discharging phase are also in good agreement with the experimental results.

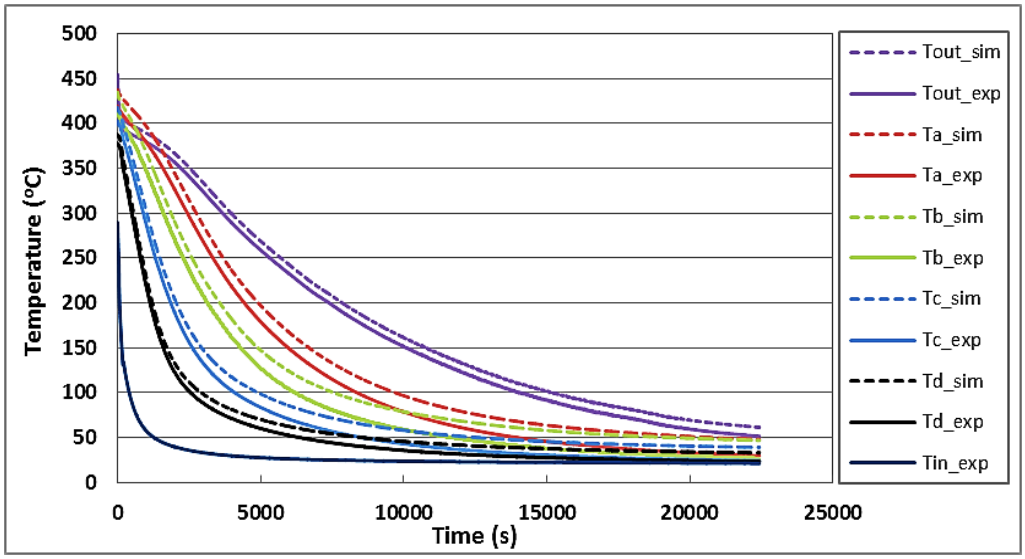

Figure 4-20.Temperature variation at different axial positions of the storage during discharging

The contour plots of the storage temperature at different intervals of the discharging phase are represented by Fig.4-21.

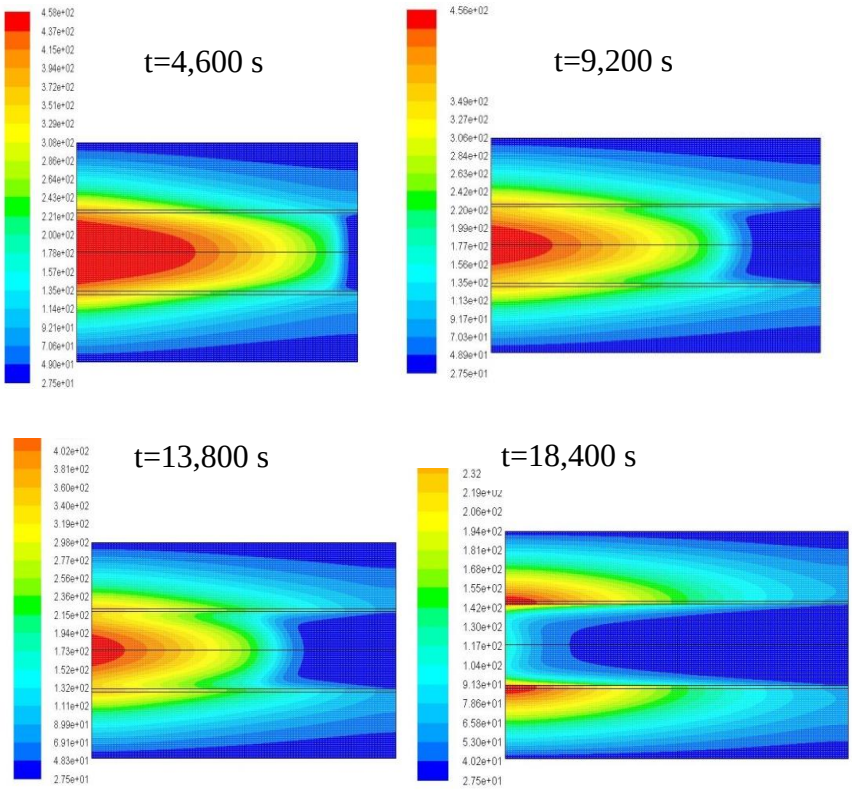

Figure 4-21.Static temperature contours (°C) at different intervals of discharging phase

The initial condition of the discharging phase corresponds to the final state of the charging phase. The thermocline zone now shifts towards top of the column as the discharging proceeds. The contour plots also show the influence of the thermal inertia of the wall: at the end of discharging phase the temperature close to the wall is higher than in the central part of the storage.

Thus, CFD model can predict TES temperature behaviour with good accuracy, but at high computational expense: one complete cycle i.e charging followed by discharging took around 470 hours (20 days) of continuous simulation on the Workstation (Dell Precision R7910).

4.5.2 TRANSEO Model Of Thermal Energy Storage (TES)

It is clear from the calculation time of the CFD model that this approach is not applicable for CSP dynamic system analysis, optimisation and control development through real time analysis. Therefore, it was decided to investigate a simplified model of TES based on the heat exchanger model already present in the TRANSEO software library developed by the Authors [25, 26], for real time and transient analysis of complex energy systems.

Unlike the CFD model, the approach used in the TRANSEO shows a very short simulation time for a complete TES cycle: around 140 seconds. Hence, due to its fast approach it can be effectively used to perform the TES initial design, sensitivity analysis, and it is also very useful for real time modelling to be used for both TES and whole CSP power plant control system development [39-41].

4.5.2.1 Modeling Approach

TRANSEO model of the TES is a reduced-order model based on the in-house transient simulation tool TRANSEO, which has been developed by Thermochemical Power Group (TPG) for energy system dynamic analysis. In the model used here, the following approach has been adopted to simulate the TES transient behavior:

- The energy equation is solved by the “dynamic” approach, using a space discretization into N cells of the heat exchanger, divided into four main sections (Fig.4-22): flow 0 (j=0), exchanging matrix (j=1), flow 2 (j=2) and the external vessel (j=3) in Fig.4-22. The dynamic model is based on the one-dimensional Euler fluid dynamic equations with

source terms for viscous pressure losses, heat exchanges, etc., integrated using an implicit scheme, therefore very stable and fast.

- To reduce the computational time taking into account the target of the model the "lumped-volume" formulation of the continuity and momentum equations is used, in order to consider time for mass flow to reach the steady-state conditions. The lumped-volume model is formed by an off-design model (representing the pressure drops, in this case) that behaves as an actuator disk, followed by a duct, with constant equivalent cross-sectional area and length for the fluid dynamic delay [42].

In general, the partial differential energy equation can be written as follows:

$$\boldsymbol{\rho_{j,i} c_{vj} A_{j,i} \frac{\partial T_{j,i}}{\partial t} = -c_{p,j} \dot{m}_j \frac{\partial T_{j,i}}{\partial x} + q_{j,i}} \qquad (4\text{-}6)$$

where q represents heat source term which depends on the domain under consideration. It takes into account the convective heat transfer between the fluids and the transfer surfaces, the heat dispersion to the environment and the longitudinal conductivity of the matrix and the vessel.

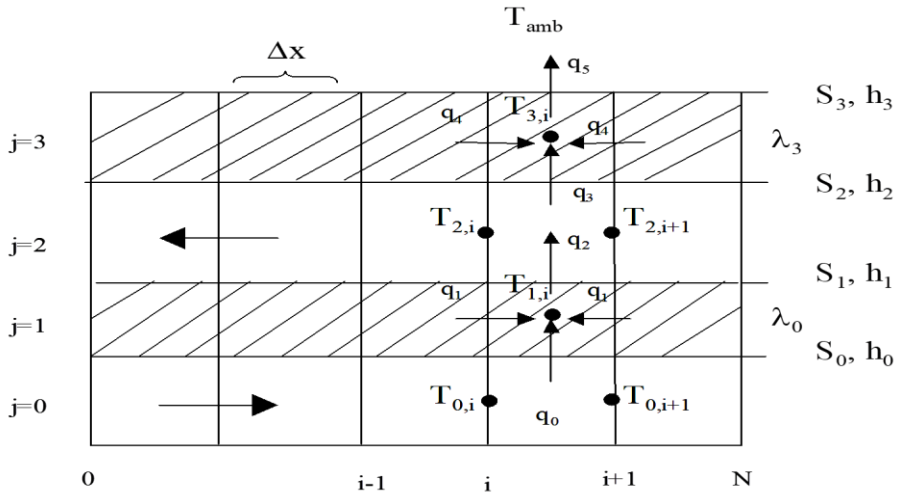

Figure 4-22. Finite difference dynamic model scheme for TES

The energy equations for the flow 2, corresponding to j=2 in Figure 4-22, are summarized below:

$$\rho_{2,i} c_{v2} A_{2,i} \frac{(T_{2,i}^{n+1} - T_{2,i}^{n})}{\Delta t} = \frac{\dot{m}_2 c_{p2}}{\Delta x}\left(T_{2,i+1}^{n+1} - T_{2,i}^{n+1}\right) - \frac{h_1 S_{1,i}}{\Delta x}\left(T_{1,i}^{n+1} - \frac{T_{2,i+1}^{n+1} + T_{2,i}^{n+1}}{2}\right) - \frac{h_2 S_{2,i}}{\Delta x}\left(\frac{T_{2,i+1}^{n+1} + T_{2,i}^{n+1}}{2} - T_{3,i}^{n+1}\right) \quad (4.7)$$

$$T_{2,i}^{n+1}\left(\rho_{2,i} c_{v2} A_{2,i} + \frac{\Delta t}{\Delta x}\dot{m}_2 c_{p2} + \frac{h_1 S_{1,i}\Delta t}{2\Delta x} + \frac{h_2 S_{2,i}\Delta t}{2\Delta x}\right) + T_{2,i+1}^{n+1}\left(-\frac{\Delta t}{\Delta x}\dot{m}_2 c_{p2} + \frac{h_1 S_{1,i}\Delta t}{2\Delta x} + \frac{h_2 S_{2,i}\Delta t}{2\Delta x}\right) + T_{1,i}^{n+1}\left(-\frac{h_1 S_{1,i}\Delta t}{2\Delta x}\right) + T_{3,i}^{n+1}\left(-\frac{h_2 2\Delta t}{2\Delta x}\right) = T_{2,i}^{n}\left(\rho_{2,i} c_{v2} A_{2,i}\right) \quad (4.8)$$

$$\alpha T_{2,i}^{n+1} + \beta T_{2,i+1}^{n+1} + \gamma T_{1,i}^{n+1} + \delta T_{3,i}^{n+1} = \varepsilon T_{2,i}^{n} \quad (4.9)$$

The exchanging surfaces Sj,i are the portion of the exchanging surface relative to each cell. Aj areas are the cross-sectional areas of the j sections of the heat exchanger. The resulting equations per each ith cell can be organized in one matrix and solved at the same time, with an implicit solution of all temperatures. More details on TRANSEO modelling approach and governing equations can be found in [24] and [25]. Since TRANSEO model needs the knowledge of pressure drops and flow condition during each stage of the storage charging or discharging phase, hence a proper investigation has been carried out by Barberis et.al [28].

The following work is aimed to achieve the best possible representation of thermal stratification inside the storage during charging and discharging phases, through both the TRANSEO model, and the CFD model. Based on the above numerical schemes and following parameters (Table.4-7), TES of the test rig shown in Fig.4.9 has been simulated with the TRANSEO model. Since reverse flow is not possible in the TRANSEO recuperator model, it is assumed that thermal storage occurs mainly in the matrix (j=1), which is ceramics in the TES. The flow 2 (j=2) is considered as charging flow and flow 0 (j=0) is considered as discharging flow. As demonstrated later, the assumption of negligible thermal storage in the vessel will be not confirmed by the experiments.

Table 4.7. CFD and TRANSEO model parameters

Parameter	TRANSEO	CFD
Heat exchange coefficient (between air and ceramics) [W/m^{2}K]	45	45

Total heat exchange area [m^2]	10	10
Specific heat of ceramics (C_p) [kJ/kg-K]	1.07*	$-7.927\times10^{-7}T^2 + 1.092\times10^{-3}T + 0.802$ [T=0-1000 ^oC] [29]
Thermal conductivity of ceramics (k) [W/m-K]	4.70*	$2.017\times10^{-6}T^2 - 4.646\times10^{-3}T + 6.484$ [T= 100-1400^oC] [31]
Density of ceramics (g/cm^3)	3.20	3.20 [30]
Density of steel (g/cm^3)	8.11	8.11 **
Specific heat of steel (C_p) [kJ/kg-K]	0.502	0.502**
Thermal conductivity of steel [W/m-K]	16.27	16.27 **
Rock wool insulation	Not considered	Thermal resistance R= 2.85 K·m^2/W,thermal conductivity: 0.045 W/m-K)
Ambient heat loss convective coefficient [W/m^2K]	4	4
Inlet pressure of TES for charging[bar]	2.11	2.11
Inlet pressure of TES for discharging[bar]	2.24	2.24

*This is the average value of the same data taken in CFD over the entire temperature range.
**ANSYS-FLUENT data base.

4.5.2.2 TRANSEO model validation

Similar to the CFD results, TRANSEO results are presented in terms of temperature distribution inside the ceramics i.e Ta, Tb, Tc, and Td from top to bottom and outlet air temperature. Fig. 4-23 and 4-24 represent the simulation results (dashed lines) against the experimental data (solid lines) during the charging and discharging phase, respectively.

From the Fig.4-23, it is evident that the TRANSEO model can reasonably predict the thermal gradient inside the TES during charging phase, except some duration after the initial transient phase when model tends to overestimate the TES inner temperatures. Some discrepancies from the experimental results are related to the 1D discretization of the TES: 1D model is not able to properly capture the impact of the radial temperature gradient which is created due to interaction with the metallic vessel and external insulation, and this is slightly affecting the results.

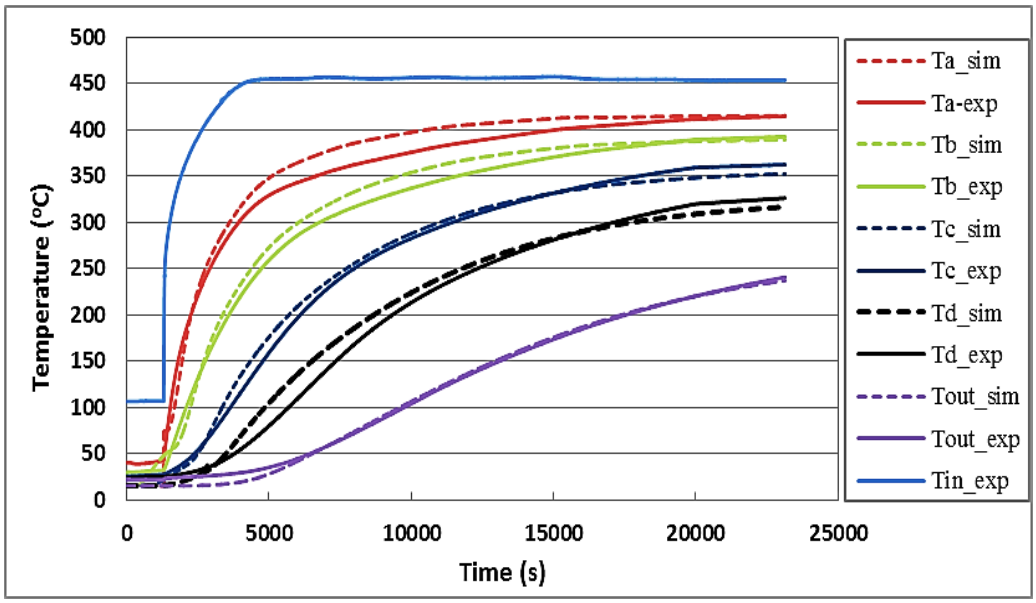

Figure 4-23. Temperature variation at different axial positions of the storage during charging

While during discharging (Fig.4-24), simulated results are in less agreement with the experimental data. In discharging, after the initial transient phase the simulated temperature profiles dropped more quickly than the experimental ones. This is due to the fact that in discharging, the steel vessel is not impacting on the flow, due to the recuperator-like model, where we do not have coincident domains for the charging and discharging phases, and reverse flow is not possible. During the discharging phase, energy stored in the vessel has no impact on the outflow. Experiments, instead, show that the vessel and insulation have a significant impact on the thermal results: this can be well upgraded in the future, since the root cause is now evident.

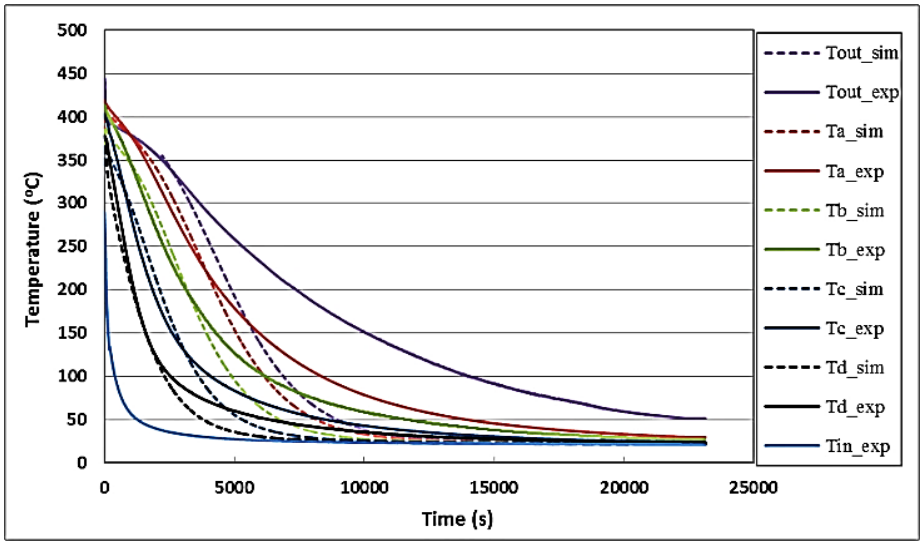

Figure 4-24. Temperature variation at different axial positions of the storage during discharging

4.6 Modelling capability of CFD and TRANSEO Models of TES

After experimental validation of CFD and TRANSEO models, modelling capability of both models to represent the actual TES behaviour is compared.

4.6.1 Relative Percent Error

The capability of both models to represent the thermal stratification of actual TES has been compared in terms of Root Mean Square (RMS) value of the relative percent error between the simulation and experimental results at different points, during the whole cycle (Eq.4-10).

$$RMS_a = \sqrt{\frac{\sum_{t=1}^{N}(e_{rel,t})^2}{N}} \qquad (4\text{-}10)$$

Where N represents the total charging/discharging time

Table 4.8and 4.9 report the RMS values for temperatures Ta, Tb, Tc, and Td calculated during the charging and discharging phases, respectively. It is evident that CFD model can better explain the thermal behaviour of actual TES in comparison with 1D-TRANSEO model, particularly in the discharging phase. The absolute values of errors verify the higher modelling capability of 2D discretised CFD model.

Table 4.8. RMS values of relative percent error between model and experimental results of charging

RMS value	CFD Model	TRANSEO Model
$\mathbf{RMS_a}$	8.7	14.7
$\mathbf{RMS_b}$	8.0	12.2
$\mathbf{RMS_c}$	8.6	10.6
$\mathbf{RMS_d}$	5.0	13.5
$\mathbf{RMS_{out}}$	6.0	4.5

Table 4.9. RMS values of relative percent error between model and experimental results of discharging

RMS value	CFD Model	TRANSEO Model
$\mathbf{RMS_a}$	12.1	25.0
$\mathbf{RMS_b}$	13.0	23.5
$\mathbf{RMS_c}$	9.0	24.3
$\mathbf{RMS_d}$	5.5	19.5
$\mathbf{RMS_{out}}$	7.6	35.5

4.6.2 State of Charge (SoC) Estimation of TES

The modelling capability of both CFD and TRANSEO model has also been compared in terms of the State of Charge (SoC) of TES. Using the axial temperature distribution obtained from experimental and simulation results of the charging phase, the SoC is calculated according to Eq. 4.11.

$$\boldsymbol{SoC} = \frac{\sum_{i=1}^{N} (T_i - T_{min})}{N \times (T_{max} - T_{min})} \qquad (4.11)$$

where N is the total number of temperature monitoring points. Figure 4-25 shows that SoC simulated by CFD model shows good agreement with the actual SoC for most of the time. TRANSEO model overestimates the TES temperatures after the initial phase of the transient

in charging when radial thermal gradient becomes relevant, hence in this phase SoC is higher than the experimental SoC.

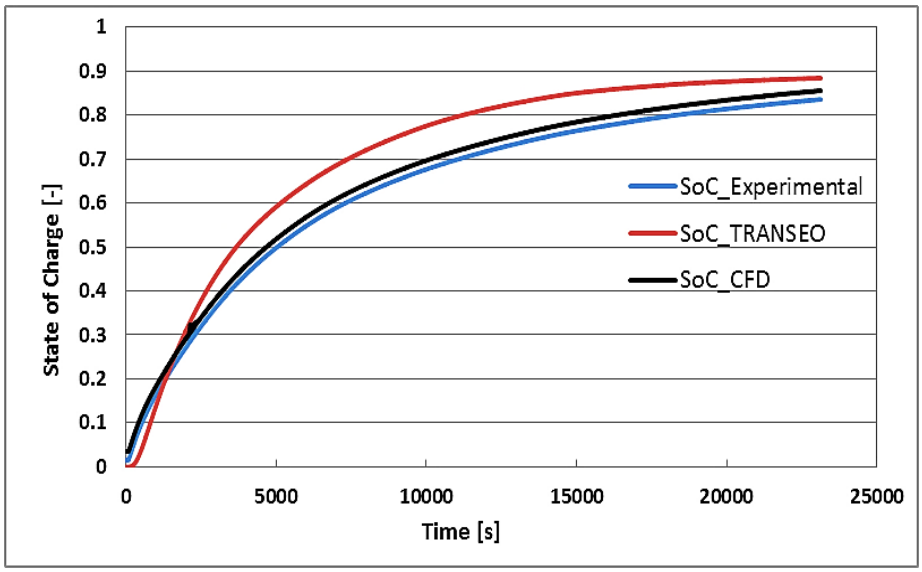

Figure 4-25. SoC estimation during charging of TES

During discharging, after the initial transient phase SoC predicted by TRANSEO is lower than experimental one, which illustrate that rate of heat releasing (discharging rate) exceeds the experimental rate of discharging (Fig.4-26). Overall, during each phase the CFD model presents the actual SoC of TES more accurately, in comparison with TRANSEO model as expected.

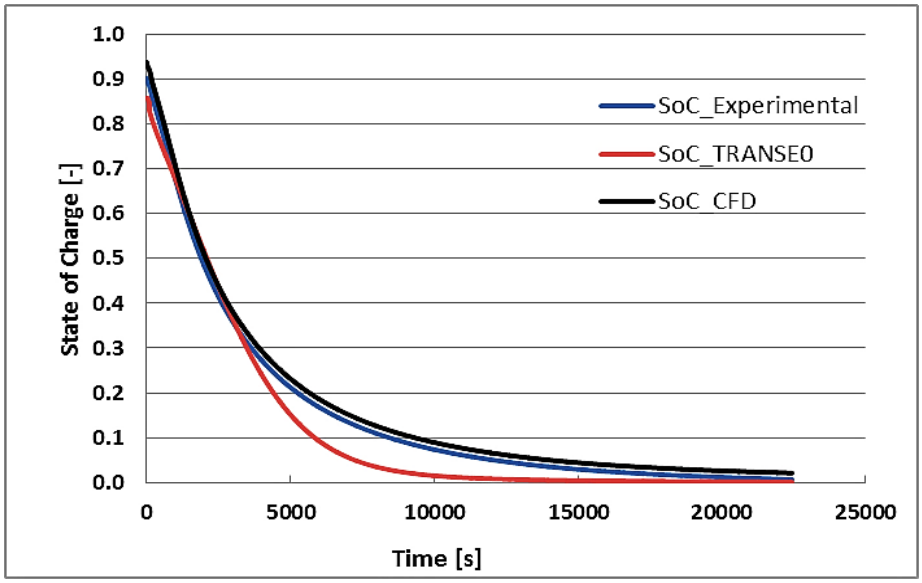

Figure 4-26. SoC estimation during discharging of TES

4.7 Thermal Losses from TES

Thermal energy extracted from the storage system is always less than that stored, as a result of some inevitable losses and irreversibility inherent in the storage process. In order to estimate the energy losses in TES under study, we assume full charged condition when temperature is maximum at all the axial locations of storage i.e 420°C. Total thermal energy stored in the TES depends on total thermal capacitance of the storage:

$$\boldsymbol{Q_{stored}} = \left[\left(\boldsymbol{m_{ceramic}}.\boldsymbol{c_{p,ceramic}}\right) + \left(\boldsymbol{m_{steel}}.\boldsymbol{c_{p,steel}}\right)\right].\ \Delta\boldsymbol{T} \qquad (4.12)$$

where ΔT is the difference between initial (ambient temperature) and final maximum temperature of the storage at the end of the charging

Total thermal losses (Qloss,total) from the TES consist of losses through internal convection, insulation conductance, and external convection to the ambient. Hence, total thermal resistance considering the cylindrical symmetry of the storage is:

$$\boldsymbol{R_{total}} = \left[\frac{1}{h2\pi r_1 L} + \frac{\ln(r_2/r_1)}{2\pi k_{ins} L} + \frac{1}{U_{amb} 2\pi r_2 L}\right] \qquad (4.13)$$

Where r_1 and r_2 are internal and external radius of the storage vessel, respectively

Total thermal losses from internal ceramic to the ambient over the time *t* are estimated as:

$$\boldsymbol{Q_{loss,total}} = \frac{\Delta T}{R_{total}}.\boldsymbol{t} \qquad (4.14)$$

Hence, rate of energy lost (Q_{lost}) from a fully charged storage can be estimated as:

$$\boldsymbol{Q_{lost}}(\%/\boldsymbol{time}) = \frac{Q_{loss,total}}{Q_{stored}} \times \mathbf{100} \qquad (4.15)$$

Applying above approach for the TES under study, the amount of total energy stored in a fully charged TES and thermal losses estimated for one hour, are mentioned in Table 4.10.

Table 4.10. Energy stored and thermal losses in TES

Q_{stored} (MJ)	34.5
$Q_{loss,total}$ (MJ)	0.5
Q_{lost}(%/h)	1.5

The rate of energy lost is estimated with the TES at its maximum temperature, and it actually decreases with the TES average temperature, e.g. during discharging. The rate of energy lost can be reduced by increasing the TES size, i.e. by increasing the volume to surface ratio. Therefore, this TES technology can offer very low thermal losses, and it can be used as an efficient way for long term thermal storage.

4.8 Final Remarks

The present work is focused on dynamic modelling as well as experimental validation of the TES, which is part of the HSGT system under development at the University of Genova. The modelling work compares two time-dependent approaches: a CFD model using ANSYS-FLUENT® code and a simplified model using the simulation tool TRANSEO, developed by TPG.

The 2D modelling of TES was aimed to capture the thermal gradient in axial as well as radial direction of the storage vessel. Satisfactory agreement between the CFD model and the experimental results has highlighted that 2D discretization of the TES can well represent the thermal behaviour of the system. This may be useful for the detail analysis and can also be used for calibration of more simple models which are useful for system transient analysis and control development. However, CFD demands complex modelling techniques and suffers of a high computational cost; hence it is not useful for CSP plant dynamic analysis including real time modelling for control development of the whole CSP plant.

The second analysis has been carried out using a simplified model, which is a 1D model based on a gas-gas heat exchanger model already present in the TRANSEO code library and previously validated. Experimental validation has highlighted that TRANSEO model can also

predict the thermal gradient inside the TES, but, as it was expected, less agreement with experiments is evident mainly during the discharge phase. The justification is related to the fact that 1D discretization is obviously not able to capture the radial temperature gradient which is created due to interaction with the metallic vessel and external insulation.

However, the TRANSEO results, when used properly at the system level, have shown a good level of confidence and, therefore, the TRANSEO approach can be used for system dynamic analysis, real time modelling and control development. In order to improve the TRANSEO approach and model parameters, proper validation at certain conditions may be carried out using the CFD approach that is not applicable for whole plant analysis. In such a way a reduced modelling work is possible.

Hence, we can conclude that 2D discretization of the TES through CFD model can be used to visualize more accurate thermal stratification inside TES. On the other hand, the TRANSEO model offers other advantages over the CFD approach, at the cost of reduced accuracy: due to less computational cost and fast approach it can be effectively used to perform the initial design and sensitivity analysis of TES, control system development and real time transient analysis for the whole plant.

In addition to the modelling scope of both models, this study also highlights the potential of the TES systems based on the monolithic structures for hybrid gas turbines systems. Due to high void fraction (0.85), the ceramic monoliths in TES under study cause low pressure drops across the TES, which are acceptable for the whole gas turbine hybrid system. Due to modular structure also, this TES system can be scaled-up for integration in large power systems. Moreover, this TES system offers very low thermal losses, i.e 1.5% per hour from the fully charged TES (losses can be reduced further by increasing the size of the TES), and thus can be effectively used for long term thermal storage applications.

References

1. Dincer, I., and Rosen, M.A., 1998. A worldwide perspective on energy, environment and sustainable development. International Journal of Energy Research 22 (15), 1305–1321.
2. Dincer, I., 2000. Renewable energy and sustainable development: a crucial review. Renewable and Sustainable Energy Reviews 4(2), 157-175.
3. Rivarolo, M., Cuneo, A., Traverso, A., and Massardo, A.F., 2016. Design optimization of smart poly-generation energy districts through a model based approach. Applied Thermal Engineering, 99, 291-301.
4. Grange, B., Dalet, C., Falcoz, Q., Siros, F., and Ferrière, A., 2014. Simulation of a hybrid solar gas-turbine cycle with storage integration. Energy Procedia 49, 1147-1156.
5. EUR 21615-SOLGATE-Solar Hybrid Gas Turbine Electric Power System. Final report by Office for Official Publications of the European Communities, 2005. ISBN 92-894-4592-0.
6. Lanchi, M., Montecchia, M., Crescenzia, T., Melea ,D., Miliozzia, A., Russoa, V., Mazzeia, D., Misceoa, M., Falchettaa, M., and Mancinib, R., 2015. Investigation into the coupling of Micro Gas Turbines with CSP technology: OMSoP project. Energy Procedia 69, 1317 – 1326.
7. Queroa, M., Korzynietzb, R., Ebert, M., Jiméneza, A.A., Ríoa, D.A., and Brioso, J.A., 2013. SOLUGAS – Operation experience of the first solar hybrid gas turbine system at MW scale. Energy Procedia 49, 1820-1830.
8. https://www.israel21c.org/israels-solar-powered-tulips/. Last access on 28-01-2018.
9. PEGASE project: http://www.fp7 pegase.com, last access 24/11/2017.last access on 5/12/2017.
10. Soria, R., Portugal-Pereira, J., Szklo, A., Milani, R., and Schaeffer, R., 2015. Hybrid concentrated solar power (CSP)-biomass plants in a semiarid region: A strategy for CSP deployment in Brazil. Energy Policy 86, 57-72.
11. Astolfi, M., Xodo, L., Romano, C. M., and Macchi, E., 2011. Technical and economic analysis of a solar-geothermal hybrid plant based on an Organic Rankine Cycle. Geothermics 40, 58-68.
12. Arce, P., Medrano, M., Gil, A., Oró, E., and Cabeza, L., 2011. Overview of thermal energy storage (TES) potential energy savings and climate change mitigation in Spain and Europe. Applied. Energy 88 (8), 2764–2774.

13. Ismail, K.A.R., Stuginsky Jr, R., 1999. A parametric study on possible fixed bed models for PCM and sensible heat storage. Appl. Therm. Eng. 19 (7), 757–788. 16.

14. Anderson, R., Shiri, S., Bindra, H., and Morris, J.F., 2014. Experimental results and modeling of energy storage and recovery in a packed bed of alumina particles. Appl. Energy 119, 521–529.

15. Xu, C., Wang, Z., He, Y., Li, X., Bai, F., 2012. Sensitivity analysis of the numerical study on the thermal performance of a packed-bed molten salt thermocline thermal storage system. Applied Energy 92, 65–75.

16. Anderson, R., Bates, L., Johnson, E., and Morris, F. J, 2015. Packed bed thermal energy storage: A simplified experimentally validated model. Journal of Energy Storage 4, 14-23.

17. Agrafiotis, C., Tescari, S., Roeb, M., Schmucker, M., Sattler, C., 2015. Exploitation of thermochemical cycles based on solid oxide redox systems for thermochemical storage of solar heat. Part 3:Cobalt oxide monolithic porous structures as integrated thermochemical reactors/heat exchangers. Solar Energy 114, 459–475.

18. Nash, A.L., Badithela, A., and Jain, N., 2017. Dynamic modeling of a sensible thermal energy storage tank with an immersed coil heat exchanger under three operation modes. Applied Energy 195, 877–889.

19. Yang Z., Garimella, V., 2013. Cyclic operation of molten-salt thermal energy storage in thermoclines for solar power plants. Applied Energy 103, 256–265.

20. Zanganeh, G., Pedretti, A., Zavattoni, S., Barbato, M., and Steinfeld, A., 2012. Packed-bed thermal storage for concentrated solar power-pilot-scale demonstration and industrial-scale design. Solar Energy 86 (10), 3084–3098.

21. Ismail, K.A.R., Stuginsky Jr, R., 1999. A parametric study on possible fixed bed models for PCM and sensible heat storage. Appl. Therm. Eng. 19 (7), 757–788.

22. Cascetta, M., Cau, G., Puddu, P., and Serra, F., 2014. Numerical investigation of a packed bed thermal energy storage system with different heat transfer fluids. Energy Procedia 45,598 – 607.

23. Cascetta, M., Cau, G., Puddu, P., and Serra, F., 2016. A comparison between CFD simulation and experimental investigation of a packed-bed thermal energy storage system. Applied Thermal Engineering 98, 1263–1272.

24. Traverso, A., 2005. TRANSEO code for the dynamic performance simulation of micro gas turbine cycles. ASME Paper GT2005-68101.

25. Traverso, A., 2004. TRANSEO: a new simulation tool for transient analysis of innovative energy systems, Ph.D. Thesis, DIMSET, Università di Genova, Genova, Italy.

26. Traverso, A., Barberis, S., Lima, D., and Massardo, A.F., 2014. Dynamic analysis of concentrated solar hybridized gas turbines. ASME Paper GT2014-25225.

27. Barberis, S., Spoladore, A., Traverso, A., Traverso, A.N., and Porta, M., 2014. High temperature storage for CSP plants: Test rig dynamic analysis .7th International Gas Turbine Conference, Brussels, Belgium.

28. Barberis, S., Traverso, A.N., Traverso, A., and Massardo, A.F., 2016. High temperature storage for CSP hybrid gas turbine: test rig dynamic analysis and experimental validation. ASME Paper GT2016-56202.

29. Hildmann, B., and Schneider, H., 2004. Heat capacity of Mullite: new data and evidence for a high-temperature phase transformation. Journal of American Ceramic Society 87 (2), 227–34.

30. Schneider, H., Schreuer. J., and Hildmann, B., 2008. Structure and properties of Mullite-A review. Journal of the European Ceramic Society 28, 329–344.

31. Anggono, J., 2005. Mullite Ceramics: Its Properties, Structure, and Synthesis. JURNAL TEKNIK MESIN Vol. 7, No. 1, April 2005: 1 – 10.

32. Zavattoni, S.A., Barbato, M.C., Pedretti, A., Zanganeh, G., and Steinfeld, A., 2014. High temperature rock-bed TES system suitable for industrial-scale CSP plant – CFD analysis under charge/discharge cyclic conditions. Energy Procedia 46, 124-133.

33. Cravero, C., and Marsano, D., 2017. Numerical simulation of regenerative chambers for glass production plants with a non-equilibrium heat transfer model. WSEAS TRANSACTIONS on HEAT and MASS TRANSFER. E-ISSN: 2224-3461.

34. Cravero, C., Marsano, D., and Spoladore, A., 2017. Numerical strategies for fluid-dynamic and heat transfer simulation for regenerative chambers in glass production plant. International Journal Of Mathematical Models And Methods In Applied Sciences. ISSN: 1998-0140.

35. ANSYS FLUENT 12.0 User's guide, Copyright ©2009 by ANSYS, Inc.

36. Klein, P., Roos, T.H., and Sheer, T.J., 2015. Parametric Analysis of a high temperature packed bed thermal storage design for a solar gas turbine. Solar Energy 118, 59-73.

37. A.F. Mills, Heat Transfer, Second Edition, Prentice-Hall, New Jersey, 1999.

38. Tesfay, M., 2014. CFD analysis of sensible thermal energy storage system using solid medium in solar thermal power plant. International Journal of Advances in Engineering & Technology, ©IJAET, ISSN: 22311963.

39. Ghigliazza, F., Traverso, A., Massardo, A.F., Wingate, J., and Ferrari, M.L., 2009. Generic real-time modeling of solid oxide fuel cell hybrid systems. Journal of Fuel Cell Science and Technology 6 / 021312-1.

40. Ferrari, M. L., Pascenti, M., Sorce, A., Traverso, A., Massardo, A.F., 2014. Realtime tool for management of smart polygeneration grids including thermal energy storage. Applied Energy 130, 670678.

41. Ferrari M.L., Traverso A., Massardo A.F., 2016. Smart polygeneration grids: Experimental performance curves of different prime movers. Applied Energy 162, 622-630.

42. Larosa, L., Traverso, A., and Massardo, A.F., 2016. Dynamic analysis of a recuperated mGT cycle for fuel cell hybrid systems. ASME Paper GT2016-57312.

5 Thermochemical Energy Storage

This chapter is focused on the mathematical model for a thermochemical storage based on the redox cycle of cobalt oxides. The transient numerical model involves the energy balance and reaction kinetics of cobalt oxides to simulate the storage cycle, and results have been validated against a reference model from the literature. The developed model provides basis for more advance modeling of thermochemical storage systems and can be used for design optimization and parametric analysis.

5.1 Thermal Energy Storage (TES)

In the last few decades, rapid increase in energy demand, together with growing concern of environmental conservation have resulted in a significant impulse to the development of clean energy systems. Despite of the exhaustible and dwindling supply, fossil fuels still occupy a privileged position in our energy mix owing to their high power density and ease of transportation and storage. Renewable energy sources help to mitigate the tension between the energy demands and public concerns on environmental pollution hence can play a critical role in achieving low carbon economy and reduce the dependency on fossil fuels [1].

Among the renewables, concentrated solar power (CSP) is currently unmatched in its magnitude, cost effectiveness and ease of hybridization. However, the lack of synchronization between solar electricity production and consumption makes the energy storage crucial for the electric grid to function effectively [2].

Thermal storage can be based upon the following basic principles: Sensible Heat Storage (SHS), where heat is stored by increasing the storage medium temperature; Latent Heat Storage (LHS), where energy is stored during the phase transition of PCM; Thermochemical heat Storage (TCS), where energy is stored in reversible chemical reactions [3]. Sensible heat storage represents the simplest and least expensive form of thermal storage. However, due to low energy density SHS require large volumes to store sufficient amounts of energy and also have large thermal losses.

Phase change materials (PCMs), such as paraffin and fatty acids, provide relatively high storage density and are available over a large temperature range. However, coupled with their technical challenges and high cost, these materials are appropriate only for short duration heat storage. On the other hand, ThermoChemical energy Storage (TCS) offers several advantages: high energy density which allows a decrease of the storage unit volume and consequently of its heat losses; possibility of long-term storage and higher temperature range. However, this technology is still under development [4]. (A detail comparison of all the storage systems has been included in chap 1 and 3 of this thesis).

5.2 ThermoChemical Energy Storage (TCES)

5.2.1 Principle of ThermoChemical Energy Storage

Thermochemical storage systems utilize a reversible reaction in which solar energy is stored in chemical form, and heat stored is linked to the reaction enthalpy (ΔH_r). The basic idea of the process is to use concentrated solar thermal energy during high irradiation hours to drive an endothermic chemical reaction i.e charging phase. During this step, thermal energy is used to dissociate a chemical reactant (A), into products (B) and (C).

$$\boldsymbol{A \overset{\Delta Hr}{\Longleftrightarrow} B + C}$$

If this reaction is fully reversible, the thermal energy can be recovered completely by the reverse, exothermic reaction taking place during off-sun operation i.e discharging phase. During the releasing step, the products of the endothermic reaction (B and C) are mixed together and react to form the initial reactant (A). The products of both reactions can be

stored either at ambient temperature or at operating temperature. The generated heat during the exothermic step can be used for power production or heating applications.

The total heat stored in complete cycle depends on the reaction enthalpy (ΔH_r), extent of conversion (α) and mass of the reactant (m) [5]:

$$Q = \alpha . m . \Delta H_r \qquad (5.1)$$

Thermochemical process is divided in two different systems:

- **Chemical reactions**
- **Sorption systems.**

In chemical reactions storage systems, reactive materials of high energy storage density and reversibility are required to achieve efficient storage cycle. Usually TES based on the chemical reaction have better storage performance and efficiency than sensible and latent heat storage systems. These systems are used at high temperature (more than 400 °C) and the main reactions involved are: carbonation reaction, ammonia decomposition, metal oxidation reactions and sulfur cycles [6].

In sorption systems, heat is stored by separation of substances and heat recovery is through recombination. This process is carried into closed and open sorption storage systems. In closed systems, not the sorbate itself but the energy is released/absorbed to/from the environment via a heat exchanger. Sorbate remains within the system (not only water can be used but also other liquids such as ammonia or methanol), and only the evaporation heat is taken from the ambient. The system is mainly composed by two vessels: a reactor where the reactive sorbent is located and a condenser/evaporator where water is collected or condensed and later evaporated (Fig.5.1-a). The charging process consists of a desorption reaction in the reactor and a gas-liquid phase change reaction in the condenser. While, the discharging process works in a reverse direction: it includes a sorption reaction in the reactor and a liquid-gas phase change reaction in the evaporator. Closed sorption is mainly used for space heating and cooling.

Open sorption systems operate at the atmospheric pressure to allow the release and sorption of the sorbate. Thus, only water can be used in those systems to preserve or not to harm the environment. In charging process, a dry air stream, after heating by an external heat

source, becomes a dry hot stream and enters a reactor filled with sorbent. Water adsorbed/absorbed by the sorbent is extracted by the hot air and leaves the bed. The air then becomes wetter and cooler. During discharging, a humid, cool air stream goes into the previously desorbed reactor. Part of the water vapour in the air is pulled in by the sorbent. The released heat of sorption warms up the air so that it could be used for heating (Fig.5.1-b). The open sorption systems offer several advantages compared with closed systems: lower cost of investment, better heat and mass transfer. Hence, current practical projects are employing open sorption systems to store thermal energy [7].

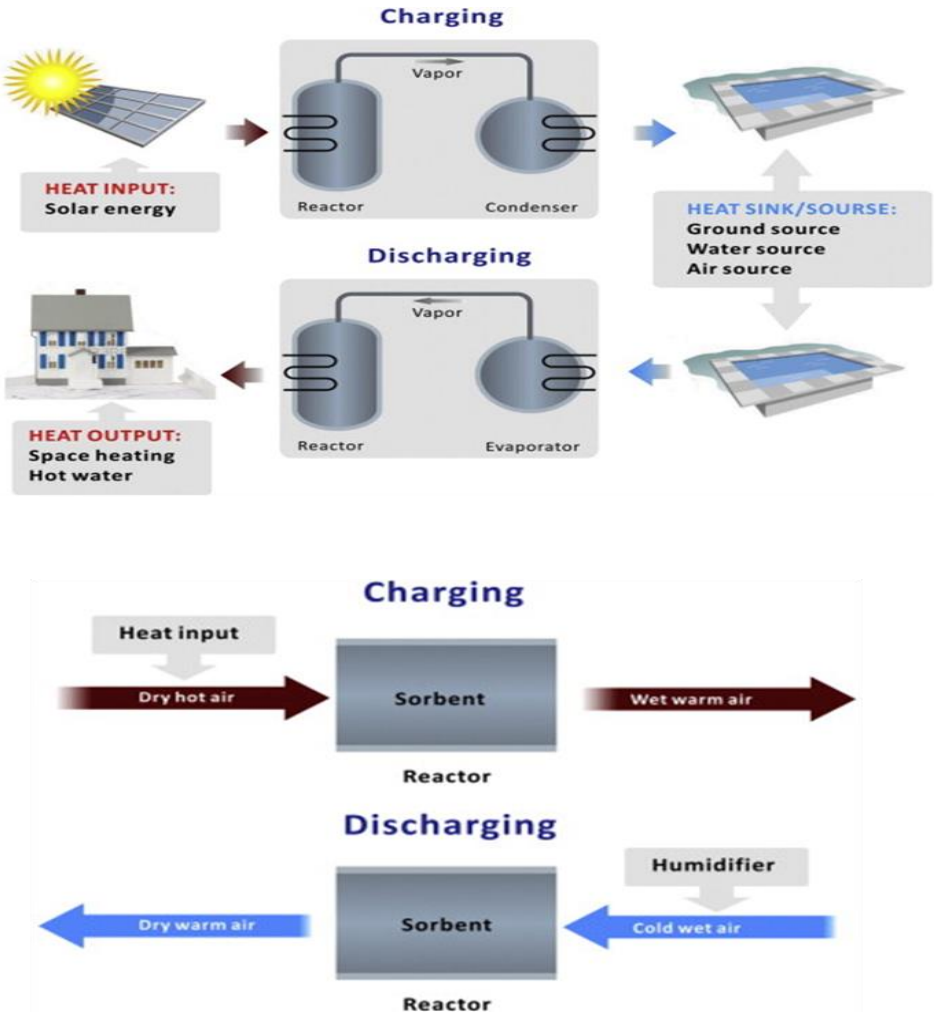

Figure 5-1.Scheme of closed (a) and open (b) sorption storage systems [7]

5.2.2 Potential and challenges of TCES systems

Thermochemical energy storage distinguishes itself through high storage capacity and density characteristics which enable an extension of operative conditions to high temperature regimes. Furthermore, energy losses during the storage period are negligible because the energy is stored as a chemical potential as long as the reactive materials do not degrade and remain unreacted and constant discharge temperature. These characteristics even allow for the long distance transportation of thermal energy and seasonal storage [8,9]. In particular, reversible gase-solid reaction systems offer high storage densities but also need to fulfill other criteria such as cycling stability, low parasitic losses, low cost, non-toxicity, non-flammability and fast heat transfer [10].

However, while TES technologies based on sensible heat and phase change materials have made their way into commercial applications, thermochemical TES for high temperature applications is still largely in a laboratory stage. The up-scaling to larger, practically relevant system sizes has proven difficult and there remain large potentials for efficiency improvements as well as loss reductions [11]. Therefore, simulation tools that capture the processes occurring inside thermochemical reactors are essential to overcome these hurdles and to gain insight into the reaction kinetics and optimize the system performance. High cost and technical challenges also limit the large scale applications of TCS systems.

Storage materials play a key role in these challenges; a suitable material can store the energy without heat loss and is able to release this energy immediately when it is needed. Following are the selection criteria of a suitable material for thermochemical storage systems, which are applicable to both sorption and chemical reaction materials [12]:

- **High storage density**
- **High thermal conductivity (in particular for adsorption) and high heat transfer from sorbate to heat exchangers**
- **Regeneration (charging) temperature as low as possible: this results in higher solar collector efficiency**
- **Heat source needed for the evaporation during discharging period at relatively low temperature**
- **Environment safety, non-toxicity, low Global Warming Potential and Ozone Depletion Potential**
- **Non-corrosiveness of materials**
- **Good thermal and chemical stability under operating conditions (temperature, pressure);**

- **Moderate operating pressure range: no excessive pressure conditions and especially no high vacuum;**
- **Low material cost**
- **High affinity for the sorbent by the sorbate: this has an effect on the rate of the ab/adsorption reaction, which is important for an usable power density**
- **Better volatility of the sorbate (than the sorbent) in absorption.**

5.2.3 State-of-the-art

5.2.3.1 Materials currently used or studied

The first analysis of possible thermochemical storage materials was given in the 1970s, and so far, several materials have been tested as potential candidate to fulfill the aforementioned requirements, for TCS systems.

Salt hydrates are chemicals that release water when heated thereby dissociating into an anhydrous salt. The anhydrous material stores the energy used for the dehydration of the material. In their anhydrous form, these salts are generally hygroscopic, and absorb or adsorb water molecules even at room temperatures. They can be impregnated into porous media such as zeolites or silica gels, which are then used as composite thermochemical energy storage materials. When heated to a charging temperature, thermochemical dehydration of the salt hydrate occurs, releasing water from the compound. The anhydrous salt has larger energy content and can be stably stored at ambient temperature for long durations. When thermal energy is required, a water vapor flow across the salt once again hydrates it, and the stored heat is released to the ambient.

One of the important salt hydrates for thermochemical storage is magnesium sulfate hepta-hydrate ($MgSO_4.7H_2O$), commonly known as Epsom salt:

$$MgSO_4 . 7H_2O \overset{\Delta H}{\Longleftrightarrow} \quad MgSO_4 + \ 7H_2O \tag{5.2}$$

Other examples of salt hydrates for TCS include $MgCl_2$ / H_2O and $SrBr_2$ /H_2O. Unlike PCMs, these salts have both high volumetric heat storage capacity and a large thermal conductivity, and are also inexpensive. However, they also pose several technical challenges: liquid super cooling is of major concern and their poor nucleating properties make them inapplicable for reuse. They melt at high heating rates, which destroy the crystal structure of the salt lattice [13].

Several reversible reaction processes for TCS have been studied so far: carbonation/decarbonation of metal oxides/carbonates, hydration/dehydration of metal hydroxides, decomposition/sulfation of metal sulfates/oxides, ammonia synthesis/dissociation and reduction/oxidation (redox) of metal oxides. Among these materials, the reduction/oxidation (redox) of metal oxides has inherent advantages relevant to its coupling with air-operated solar thermal power plants: air can be used as both the heat transfer fluid and the reactant in direct contact with the storage material (oxide) without the need for additional heat exchangers. Attractive mono-metallic redox pair oxides include: Co_3O_4/CoO , BaO_2/BaO, Mn_2O_3/Mn_3O_4 , CuO/Cu_2O, Fe_2O_3/Fe_3O_4 [14,15].

However among these systems, ammonia has the inherent disadvantage of requiring high pressures, whereas dissociation reactions of carbonates or hydroxides produce CO_2 or H_2O respectively, which have to be separated/evaporated. Co_3O_4/CoO redox pair is a most promising option due to:

- **Suitable redox temperatures (equilibrium temperature is around 1164 K at atmospheric pressure)**
- **Higher energy storage density for the complete conversion i.e. 844 kJ/kg) [16].**
- **Performance of Co3O4 does not degrade during multiple redox cycling [17].**

$$Co_3O_4 \overset{\Delta H}{\leftrightarrow} 3CoO + 1/2O_2 \qquad \Delta Hr = 196\ kJ/mol \qquad (5.3)$$

5.2.3.2 Thermochemical storage reactor/heat exchanger configurations

Thermochemical storage has significant potential to increase the efficiency of industrial processes and thus provide the reliable power supply. However, development of efficient, integrated thermochemical reactors/heat exchangers that can be suitably incorporated within the plants' infrastructure is necessary for large-scale implementation of TCS systems. Mainly thermochemical reactors can be designed in two configurations: redox-oxide-powders-fed rotary kiln receiver/reactors that can be directly solar irradiated and the redox-powder-coated honeycomb reactors.

Structured heat exchangers/reactors

Structured TCS systems are based on the concept of monolithic honeycomb solar reactors consisting of SiC honeycombs coated with redox pair. Direct solar heating of these large

scale reactors through implementation of integrated receiver/reactors is rather complicated to be realized in large-scale due to limited available irradiated surface and material conductivity. For this reason, such reactors are “indirectly” heated by using hot air produced in a separate solar receiver in a CSP plant. In this configuration, the reactor is placed inside an insulating housing where hot air from the solar receiver transfers heat to the solid material [14].

Currently, a CSP plant using air as heat transfer medium, the 1.5MWel Solar Tower Jülich (STJ) in Germany [18] is integrated with a SHS system based on ceramic honeycombs (Fig 5-2). Since SHS requires high quantities of storage media, rendering the scale-up for industrial systems rather difficult. Thus one of the major challenges is the improvement of the plant’s storage capacity by increasing the volumetric energy storage density or/and the storage temperature. The redox-oxide-based TCS systems can offer both advantages. In order to enhance gas–solid heat exchange with minimal pressure drop, the solids currently employed for sensible solar heat storage in STJ facility are porous ceramic honeycombs. Based on this system, storage system using ceramic honeycombs or foams coated with or manufactured entirely from a redox oxide has been proposed; in this way sensible heat storage can be ‘‘hybridized” with thermochemical storage within practically the same volume to achieve higher volumetric heat storage capacities [19].

The study conducted by Tescari et.al [19] describes the next developmental steps in this perspective, namely the design, development, construction and operation of a pilot-scale TCS reactor installed in the STJ facility. The reactor is comprised from 128 real-size cordierite honeycombs of a total mass of 190 kg, coated with almost 90 kg of Co3O4. Test campaigns with Co_3O_4-coated honeycombs were performed to demonstrate the proof-of-concept of the proposed technology. Single-cycle experiments were followed by multi-cycling experiments (22 cycles were run in total) to investigate the system’s performance and its reproducibility. Overall the feasibility of redox thermochemical heat storage under scaled-up and operating conditions typical for a solar power plant was proven by the successful test campaign carried by Tescari et.al [19].

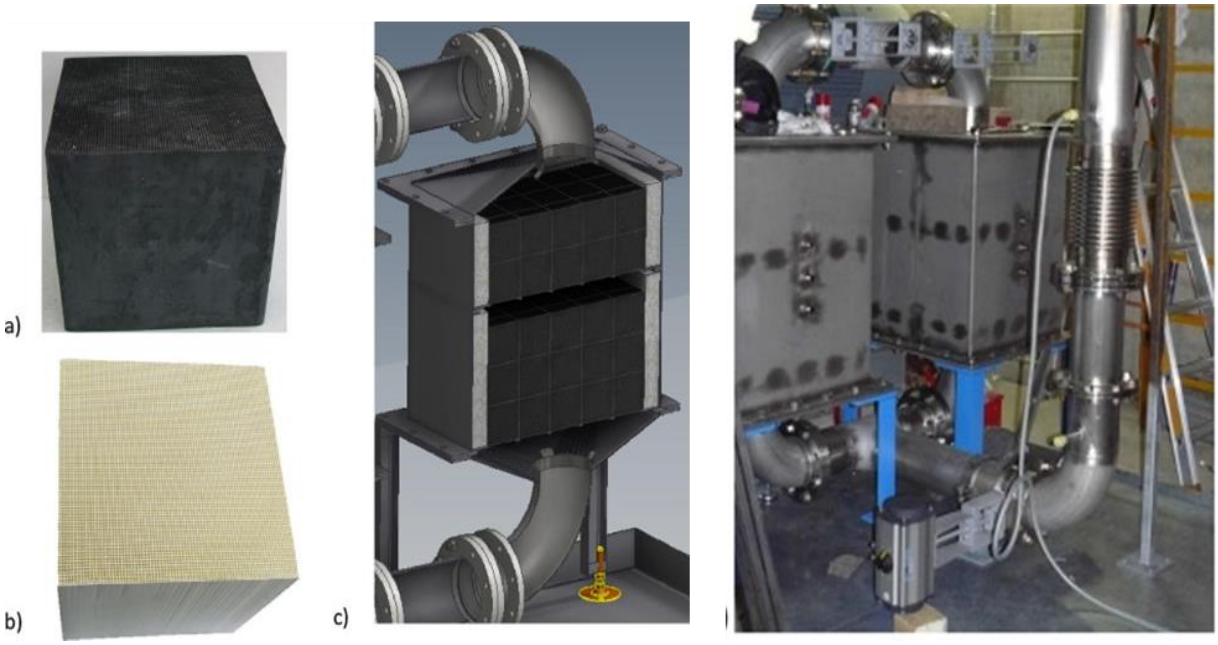

Figure 5-2.Cordierite honeycomb support coated with cobalt oxide (a), uncoated cordierite honeycomb (b), drawing of one reactor chamber with storage material and housing (c), pilot-scale reactor chamber in the STJ plant (d),(reprinted from [18])

Non-structured heat exchanger/reactors

Non-structured TCS heat exchanger/reactors are based on the packed beds, fluidized beds or rotary kilns filled with reactive materials in the form of powder. The packed bed reactor is the simplest reactor concept within which charging and discharging phases can be performed through hot/cold air. This reactor concept is relatively easy to be built and operate, but suffers from high energy losses due to the pressure drop inside the bed when scaling up the reactor. Moreover, the high reaction temperatures required to be achieved during the charging phase require the use of even higher heating fluid temperatures and thus higher temperatures on the receiver [14].

In the rotary kiln reactor configuration, the reactive particles are directly heated through concentrated solar radiation, by introducing the particles on the receiver. This configuration offers several advantages: cavity shape allows obtaining the uniform temperature on the internal wall, and reduces the radiation heat losses. Furthermore the particle movement intensifies the heat transfer not only between the particles themselves but also between the particles and the wall.

Neises *et.al* [20] has successfully demonstrated the feasibility of the concept of thermochemical heat storage through cobalt oxide powder inside a rotary kiln, based on batch mode operation. The chemical conversion achieved was higher than 50%. However, the energy efficiency was limited due to high thermal inertia of the reactor.

Tescari et.al [14] has designed a new optimized rotary kiln (Fig. 5-3), working in continuous mode and will be tested in a solar campaign. The continuous flowing of the particles allows heating up the reactor only once, at the beginning of the experiment. The incident energy is used only for the chemical reaction (reduction of material). The second part of the cycle (material oxidation) takes place on a separate reactor, called oxidation tank (OT). The particles extracted from the rotary kiln are conveyed to the OT under nitrogen atmosphere, where the energy is stored. During discharging, cold air enters from the bottom of the reactor, which will pass through the reactive material, absorbing the sensible and chemical heat released by the particles. Overall work is aimed to define the reactor characteristics, estimation of the optimum amount of redox powder that can be incorporated and exploited efficiently in each reactor concept and effective control of the charging/discharging phases to maximize the discharging potential.

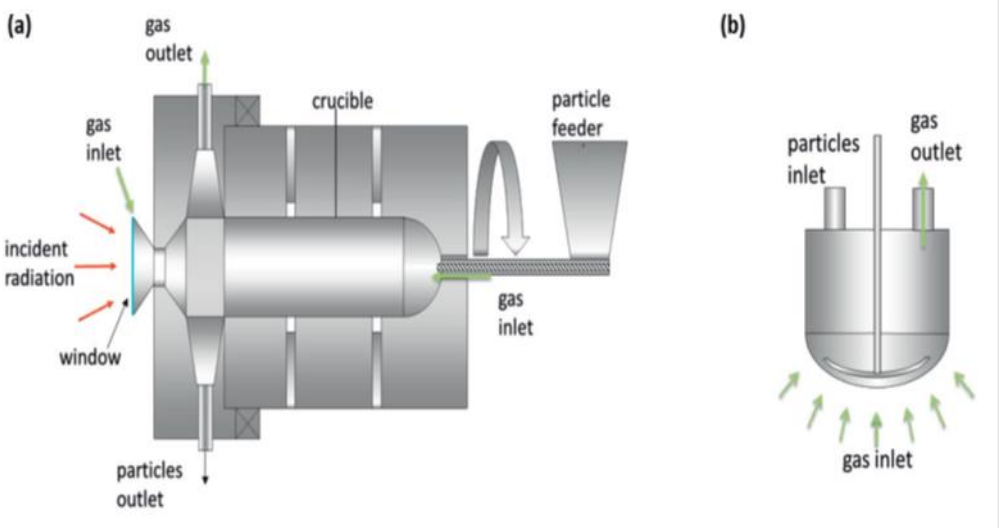

Figure 5-3. Continuous working rotary kiln for powder TCS material,(b) the oxidation tank [14].

5.3 ThermoChemical Energy Storage (TCES) Modelling

The thermochemical storage under study is originally derived from a sensible heat storage system, which has been developed at the Zhejiang University, China. This system is based on the honeycomb ceramics constituting the storage column and air is the HTF, which is heated by an electrical furnace (Figure 5-4). Luo et al. [21] have also developed the numerical model to simulate the thermal performances of this system. After the experimental validation, the developed model has been applied for the parametric study to predict the effects of geometric and thermo-physical parameters on the TES performance.

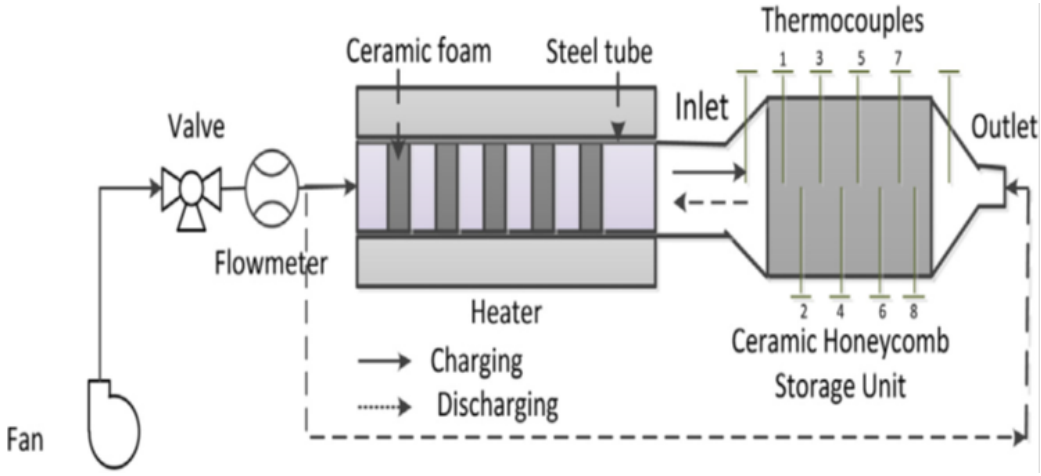

Figure 5-4.Schematic of experimental system at Zhejiang University (reprinted from [21])

Further, to achieve higher energy storage capacity and storage temperature within same volume of the storage, TCES system is proposed. Hence, next development in this project is designing of a TCES system based on the redox cycle of metallic oxides such as Co3O4/CoO or CuO/Cu2O coated on the similar ceramics honeycomb. For this purpose Thermo Gravimetric Analysis (TGA) of various metallic oxides is also being carried out to select the suitable oxides for thermochemical storage [23]. The modeling of a TCES prototype presented in this study is a contribution towards this work: optimize the storage performance and study the reaction kinetics of cobalt oxides before designing the actual TCES system. Figure 5-5 (left) shows the physical model of TCES being considered: cordierite honeycomb is coated with reactive material, i.e Co3O4, and the HTF, which is air in the present case, flows through storage during charging and discharging phases. Specifications of the storage system considered for the numerical model are presented in Table 5.1.

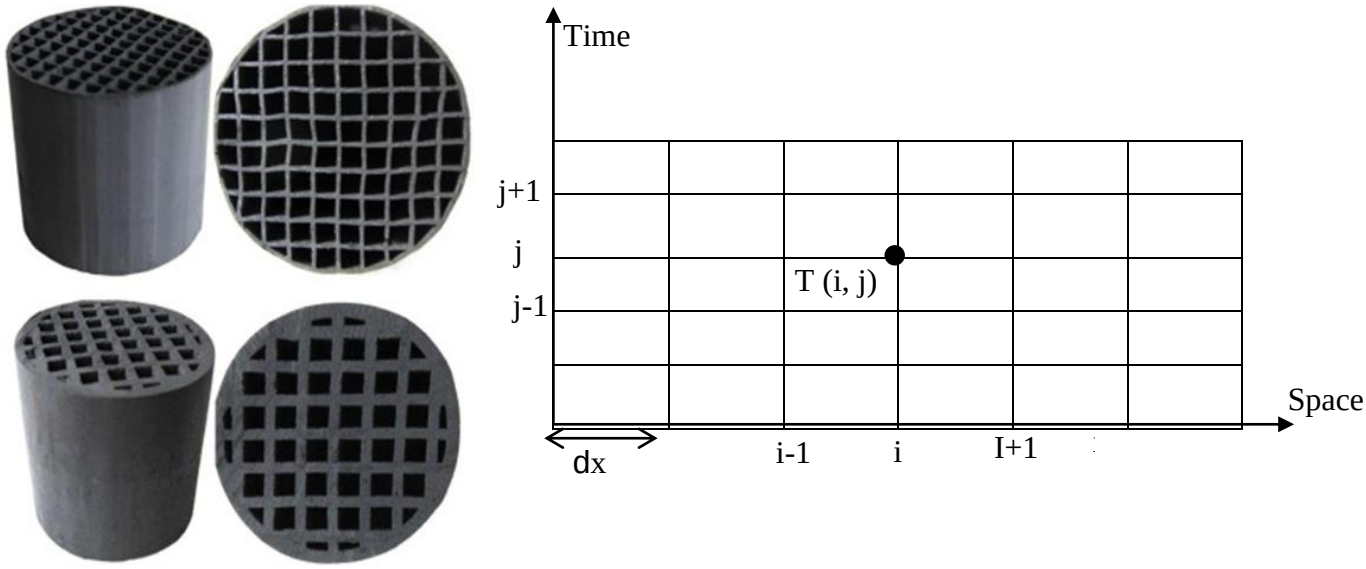

Figure 5-5. Cordierite honeycomb coated with cobalt oxide (left), Discretization scheme of the flow channel (right)

Numerical model of TCES system is one-dimensional model, developed in the MATLAB environment. The heat transfer involves conductivity of the solid material and convection between air and solid surfaces. The simulation configuration is discretized into M cells. Energy balance and reactions kinetics are solved for each i^{th} cell using explicit scheme at each time interval j (Figure 5-5, right).

Table 5.1. Specifications of the storage system

Total mass of the storage (kg)	95
Mass of the reactive material (kg)	44
Total number of flow channels in honeycomb	840
Inner diameter of the channel (m)	0.006-0.007
Length of the storage reactor (m)	0.6
wall thickness of the channels (m)	0.003
Initial fraction of Co_3O_4 inside the storage (-)	0.31

5.3.1 Heat transfer Model

In the aforementioned study [21], it is assumed that boundary of each channel is adiabatic, thus there is no heat transfer between channels. Moreover, due to very thin walls in comparison with length of the channel, thermal conductivity of the solid material in the Y axis is assumed to be infinite. Since, similar ceramics honeycombs are considered for thermochemical storage, these assumptions are also adopted for thermochemical storage modeling. The heat transfer includes conduction in the solid and convective heat transfer between air and solid surfaces. Solid and fluid are not in thermal equilibrium at any instant of the cycle, hence, to model thermal non-equilibrium separate energy equations are solved for each phase.

Solid:

$$\rho C_p \frac{T_S(j+1,i)-T_s(j,i)}{dt}.A_s = \lambda.\frac{T_S(j,i+1)-2T_s(j,i)+T_s(j,i-1)}{dx^2}.A_s + h(j).\pi.di.\left[T_g(j,i)-T_s(j,i)\right] + s_h(j,i) \quad (5.4)$$

Fluid: $$\rho(j)C_p(j).u(j).\frac{T_g(j,i+1)-T_g(j,i)}{dx}.A_f = h(j).\pi.di.\left[T_s(j,i)-T_g(j,i)\right] \quad (5.5)$$

According to Reynolds number calculation (Re<2000), the air flow is in laminar state, the empirical correlation of the convective heat transfer for laminar flow is given by Mills [24]:

$$Nu = 3.66 + \frac{0.065.Re.Pr.D/L}{1+0.04\,(Re.Pr.D/L)^{2/3}} \quad (5.6)$$

The heat transfer coefficient *h* is considered variable with temperature.

Thermodynamic properties of the HTF i.e air are considered as temperature dependent. The solid reactive material is the ceramic cordierite coated with Co_3O_4. Hence, thermodynamic properties such as specific heat capacity, thermal conductivity and density of the reactive material depend on the fraction of Co_3O_4 (φ) in the total solid material, reaction advancement (*f*) and properties ($\emptyset$) of both cordierite and cobalt oxide specie *i*. The following relation is used for each parameter $\emptyset$ [15]:

$$\emptyset = \varphi.\sum_i f\,.\emptyset_i + (1-\varphi).\emptyset_{corderite} \quad (5.7)$$

Where *i* denote the respective cobalt oxide species

Table 5.2 Material properties of cobalt oxides, cordierite and Co3O4 coated cordierite [15]

Material	Cp (J/kg-K)	ρ (kg/m^3)	λ (W/m-K)
Co_3O_4	$0.55T + 328.6$	6110	$-1.25 * 10^{-8}T^3 + 4.27 * 10^{-5}T^2 - 5.78 * 10^{-2}T + 33.381$
CoO	$0.12T + 628$	6450	---------
Cordierite	$5 * 10^{-7}T^3 - 0.0019T^2 + 2.3033T + 664.18$	2000	2.5
Reactive material i.e. Co_3O_4 Coated cordierite	$\varphi.\sum_i f\,.Cp_i + (1-\varphi).Cp_{corderite}$	$\varphi.\sum_i f\,.\rho_i + (1-\varphi).\rho_{corderite}$	$(1.95 * 10^{-12}T^4 - 2.19 * 10^{-8}T^3 + 6.05 * 10^{-5}T^2 - 0.0728T + 38.2) * (1-\varphi)$

Due to unavailability of experimental data from the TCES system since it is under development, the transient temperature and mass flow rate of the inlet air are taken from the reference study by Singh et al. [15], for the whole cycle (Figure 5-6, right). Average flow rate is 0.032 kg/s during charging and 0.025 kg/s during discharging.

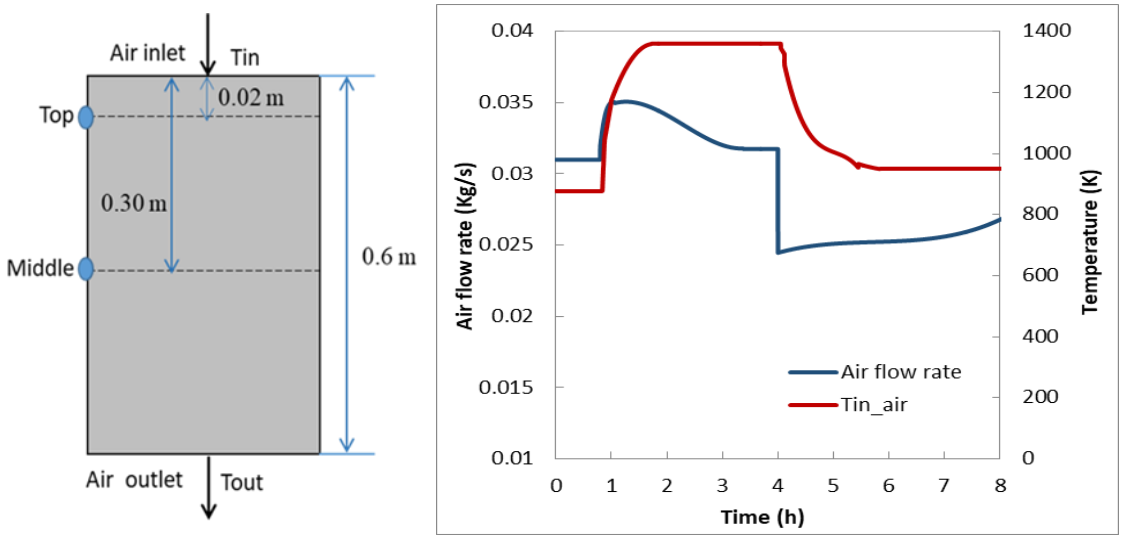

Figure 5-6 Temperature positions at various axial distances from top of the storage (left), Inlet air temperature and mass flow rate for thermochemical storage cycle (right)

5.3.2 Reaction Kinetics

The reaction kinetic model implemented in this study is based on the model originally derived by Pagkoura *et al* [26]. This model was created from the experiments using flow through pellets of Co_3O_4 in the temperature range of 1073–1273 K. Afterwards, this kinetic model was extrapolated for temperatures outside this temperature range by Singh *et al.* [15]. In actual, the kinetic model fitting parameters (E_{red} and E_{oxi}) depend upon the experimental conditions, sample preparation and the reaction mechanism. During the numerical model validation, the reaction kinetics parameters (E_{red} and E_{oxi}) are varied to get optimum fit to the experimental data. Table 5.3 shows the kinetic model parameters for this study.

The extent of reactants conversion informs us about the reaction advancement during each phase, and it is calculated from their initial concentration C_o and instantaneous concentration C_t:

$$\alpha(t) = 1 - \frac{C_t}{C_o} \tag{5.8}$$

Reaction rate constants are determined by Arrhenius relation [15]:

$$k_1 = A_{red}.e^{-\frac{E_{red}}{T}} \tag{5.9}$$

$$k_2 = A_{oxi}.e^{-\frac{E_{oxi}}{T}} \tag{5.10}$$

The overall reaction rate during each phase is defined as:

Reduction $$R_{CO3O4} = k_1.(1-\alpha) - k_2.\alpha. \tag{5.11}$$

Oxidation $$R_{CoO} = k_2.(1-\alpha) - k_1.\alpha \tag{5.12}$$

The redox reaction interacts thermally with the solid material, as it absorbs heat from the solid during the reduction step and supplies heat to it during the oxidation step. Hence, in the numerical model, a heat source term S_h is integrated in the energy equation for solid medium (Eq.3). It is defined as a function of the reaction rate *R* and concentration *C* of the reactive species at any time instant *t*, and overall reaction enthalpy ΔH_r:

$$S_{h(t)} = \Delta H_r . R_t . C_t \quad (5.13)$$

The variation of the oxygen concentration along the storage length depends on the reaction advancement: the reacting material releases and consumes oxygen during reduction and oxidation respectively. Species transport is solved to determine the change in oxygen concentration γ_{O2}during the reaction, along the channel.

$$\frac{\partial(\rho.\gamma_{O2})}{\partial t} + \nabla(u.\rho.\gamma_{O2}) = -\Delta.J_{O2} + R_{O2} \quad (5.14)$$

Where Diffusion flux ***j*** is described by Fick's law:

$$J_{O2} = D_{O2N_2}.\frac{dc_{O2}}{dz} \quad (5.15)$$

Table 5.3 enlists the kinetic model parameters which have been derived from Pagkoura *et al [26]*.

Table 5.3. Kinetic model parameters

Symbol	**Value**
ΔH_r	196000 (J/mol)
T_r	1164 K
E	E_{red} = 81,000 K E_{oxi} = -30,000 K
A	A_{red}= 2.12 *10^{27} (s^{-1}) A_{oxi}= 1.4*10^{-15} (s^{-1})
D	1.79*10^{-5} (m^2/s)
R	8.314 (J/mol.K)

5.4 Model Results and Discussion

Considering the reaction temperature of cobalt oxides and for computational convenience, the entire solid is assumed to be at 875 K in the beginning of cycle. In the beginning, the high temperature inlet air transfers heat to the solid material leading to an increase in solid temperature (sensible storage). When solid temperature approaches the reduction temperature of Co_3O_4 (1164 K at 1 bar pressure), the reaction starts and the heat from the inlet air is absorbed by the endothermic reaction (chemical storage), and solid temperature remains constant (plateau formation). When the chemical reaction reaches completion, the energy is again stored in its sensible form, and solid temperature starts rising.

Charging (reduction) $$Co_3O_4 \xrightarrow{\Delta H_r} 3CoO + 1/2O_2 \quad (5.16)$$

During discharging, cold air flows through the storage. In the beginning, the solid material releases heat to the air in sensible form, thereby cooling down the solid until the oxidation temperature of CoO (1164 K at 1 bar pressure) is reached. At the oxidation reaction temperature, the inlet air is heated up using the energy of the exothermic oxidation reaction and solid temperature remains constant resulting in plateau formation. After completion of the oxidation, again sensible heat from the solid is released to the air until the solid temperature decreases up to the inlet air temperature.

Discharging (oxidation) $$3CoO + 1/2O_2 \xrightarrow{\Delta H_r} Co_3O_4 \quad (5.17)$$

Since experimental data from the TCES system at Zhejiang University is not available at present, Authors has tried to validate the present model against the experimental data obtained from the reference study for similar system. In the reference study, Singh *et al.* [15] has modelled a TCES system based on the redox cycle of Co_3O_4/CoO, which is coated on the cordierite honeycombs. This is a 2D model based on the ANSYS-FLUENT code, and it has been validated against the experimental data from the TCES prototype reactor installed at Solar Tower Jülich (STJ), Germany [18]. The model developed in this study is also validated against the same experimental results. For this purpose, same storage specifications and concentration of the reactive materials have been considered (shown in Table 1).

Figure 5-7 shows the comparison between experimental results and our model results for temperature at the middle and top of the storage and outlet air temperature (see Figure 3), during a complete redox cycle. It can be observed that generally simulation results are in good agreement with the experimental results except some discrepancies.

It is noticed from both the experimental and simulation results that during discharging, air outlet temperature first increases almost to the final value of the inlet air temperature of charging process, and decreases afterwards. This might be due to the fact that, flowing through the front part of the storage, cold air is heated to a higher temperature which is even higher than that of the bottom of the storage, but the heat transferred from air back to solid is less than that absorbed by air from the front part, which causes an increase in outlet air temperature. After one hour of discharging, with solid temperature gradually decreasing, heat transferred to air becomes less evident; hence air outlet temperature decreases onwards.

It is evident that simulations results at the top and middle of storage are more accurate in comparison with outlet air temperature, which shows more deviations during discharging particularly. This can be due to ideal system considered in the model i.e. no heat losses from the storage; this causes peak value of the air outlet temperature higher than that of the experiments. This can also be partially justified by the air flow rate of discharging process which seemed less than that in the real experiments, which causes obvious time delay in air outlet temperature. Actually, air flow rate has been derived from the reference study by Singh *et al*. [15] (as shown in Figure 3) which shows high fluctuations. This trend cannot be exactly captured by the numerical equations provided as input to the model, thus it might not be as accurate as in the real experiments. Hence, results in deviations from the experimental data.

Overall discrepancies from the experimental data can be related to the fact that developed model is one-dimensional model; hence it cannot take into account the radial thermal effects in the storage. Moreover, one-dimensional model cannot take into account the concentration or distribution of reactive species in the whole storage more accurately, which influence the overall reaction rate and consequently the thermal behaviour of the storage.

Despite of some minor discrepancies clarified as above, the established model can reasonably predict the overall trend of thermochemical storage.

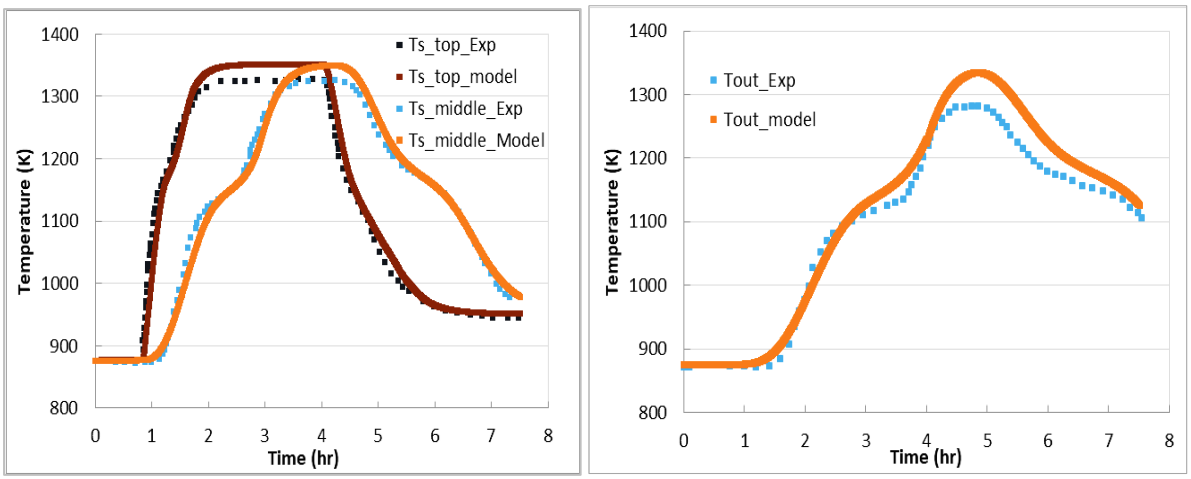

Figure 5-7 Comparison of temperatures from the model and experiments: top and middle solid temperature (left), outlet air temperature (right)

In order to demonstrate the whole cycle of thermochemical storage, different stages have been marked on a temperature curve (Figure 5-8). The temperature plateau during each phase is the characteristic of thermochemical storage. The width of the plateau (about 45 min for charge and 40 min for discharge) is proportional to the chemical energy stored inside the storage. Hence total energy stored/released in an ideal TCES system i.e without any heat losses is given as [18]:

$$Q_{stored} = Q_{sensible} + Q_{chemical} \quad (5\text{-}18)$$

Sensible heat storage ($Q_{sensible}$) depends on the total thermal capacitance of the storage material, considering heat capacity of the cobalt oxides and cordierite.

$$Q_{sensible} = m_{reactive} \cdot c_{p,reactive} \cdot \Delta T \quad (5\text{-}19)$$

Where ΔT is the temperature difference between consecutive time intervals along the storage length *(L)*

The chemical heat storage depends on the reaction enthalpy (ΔH_r) and change in concentration of the reactive species from the beginning and end of the cycle, over the entire length of the storage (*L*):

$$Q_{chemical} = \int_0^L \Delta H_r . \Delta C \, . dx \quad (5\text{-}20)$$

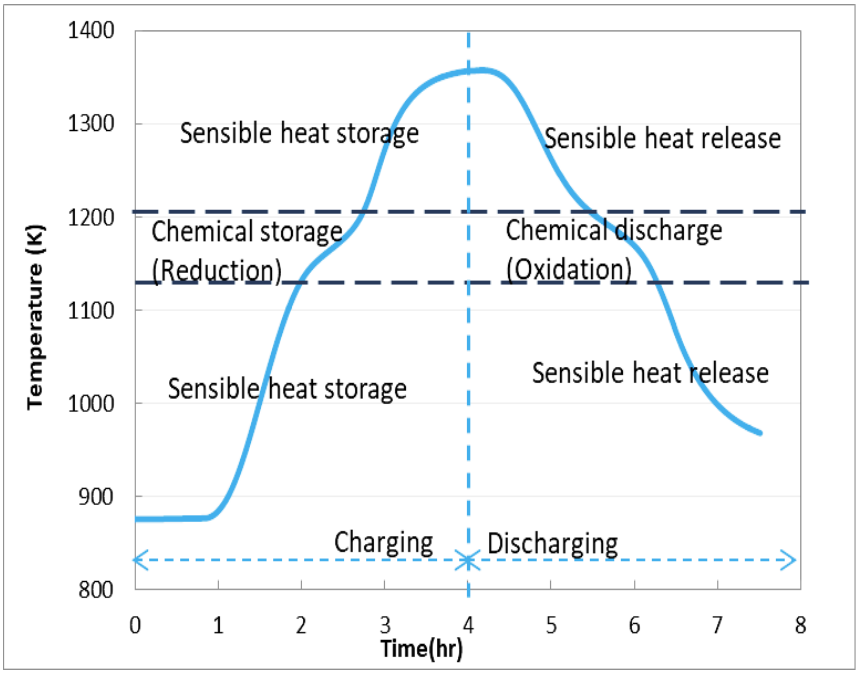

Figure 5-8. Air outlet temperature during complete redox cycle

Table 5.4 shows the total energy (sensible as well as chemical) stored/released from the TCES, and relative percent error between simulation and experimental results. It can be observed that total energy released during discharging is less than energy stored during charging: since at the end of discharging, temperature of the storage is still higher than initial temperature at the start of charging, hence some of the energy is still retained by the solid, which is not discharged. Assuming that the heat loss accounts for 18% of the total energy stored/released in the storage system [reference], the percentage relative error is 21.6% and 16.04%, for charging and discharging, respectively.

Table 5.4 Total energy stored/released during the redox cycle from TCES

	Charging	**Discharging**
$Q_{total,ideal}$ (MJ)	129.15	90.54
Q_{losses} (MJ)	23.24	16.29
$Q_{total,real}$ (MJ)	105.93	74.24
ε_{rel} *(%)*	21.60	16.04

According to stoichiometric conversion, one mole of Co3O4 will yield three moles of CoO and vice versa. The concentration of reactive species changes as the reaction proceeds. During charging, initially concentration is constant, until the solid achieves the reduction

temperature. Afterwards, the Co3O4 concentration decays as the reduction proceeds and produces CoO. When the reduction is complete concentration of both oxides again becomes constant (Figure 5-9).

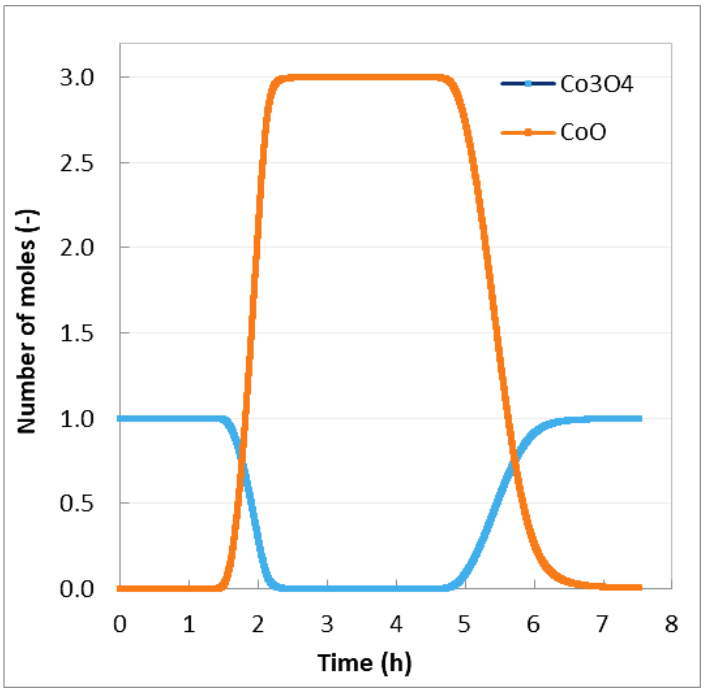

Figure 5-9 Conversion of cobalt oxides during the redox cycle

Likewise during discharging, initially concentration of CoO is constant; when solid cools down to the reaction temperature, oxidation of CoO initiates and produces Co3O4. When the oxidation is complete concentration of both species again becomes constant. Figure 6 shows the concentrations trend of both oxides during the complete redox cycle

5.5 Parametric Study for ThermoChemical Energy Storage

The developed model can be used to perform the parametric study to analyse the impact of material properties and reaction kinetics on the thermochemical storage.

The specific heat capacity of the storage material is an important parameter for the thermal capacity of storage system. Figure 7 shows the effect of the specific heat capacity of the reactive material on the outlet air temperature. Although, higher heat capacity results in higher energy storage, however, it also delays the reaction as the solid requires more heat to achieve the reaction temperature. In case of smaller heat capacity, air outlet temperature

reached the higher temperature in a shorter time during the charging phase: it reached to □1330 K in 4.4 hours when specific heat capacity was 1200 J/kg-K, and reached to □1290 K in 5.2 hours with 1200 J/kg-K specific heat capacity. However, with smaller heat capacity, air temperature dropped more quickly during discharging, while higher heat capacity resulted in more gradual heat release during discharging.

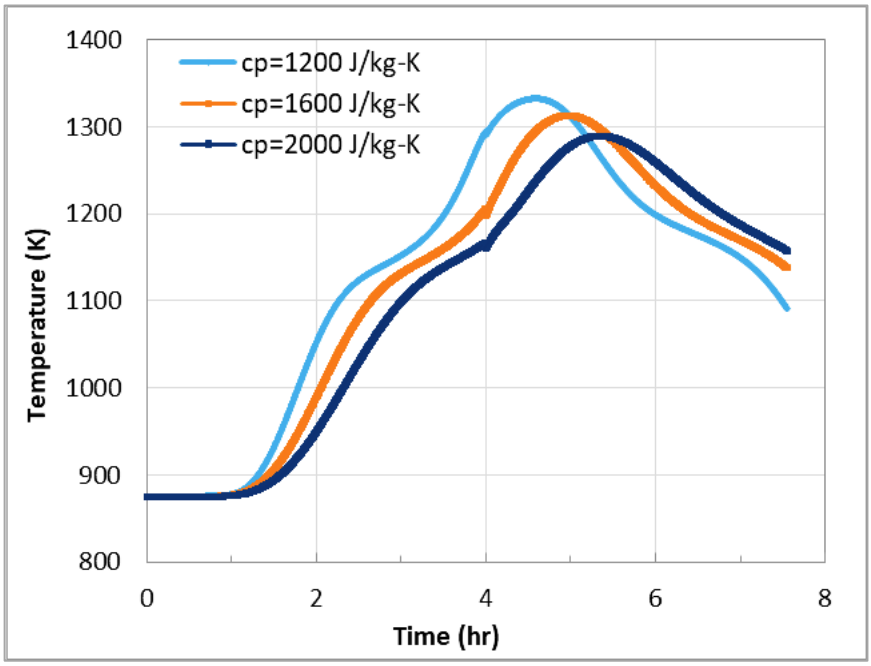

Figure 5-10 Effect of the specific heat capacity on the air outlet temperature

Reaction enthalpy of the redox pair has significant impact on the thermochemical storage process, as it determines the chemical contribution for the total energy storage i.e Qchemical (Eq.19). Higher reaction enthalpy ensures that all of the supplied energy is utilized towards the reaction and a negligible fraction of the input energy diffuses through the system. Figure 8 shows the impact of reaction enthalpy of the reactive material on the outlet air temperature.

Higher reaction enthalpy results in more chemical energy density, so width of the plateau in solid temperature curve increases both in charging and discharging. Hence, total energy storage increases with the increase in reaction enthalpy. Air outlet temperature is lower for higher reaction enthalpy during second half of the charging, as most of the energy is utilized to carry out chemical reaction: it reached to □ 1325 K when reaction enthalpy was 200 kJ/mol and reached to □1285 K when reaction enthalpy was 400 kJ/mol. During

discharging, higher reaction enthalpy results in more gradual heat release in comparison with lower reaction enthalpy.

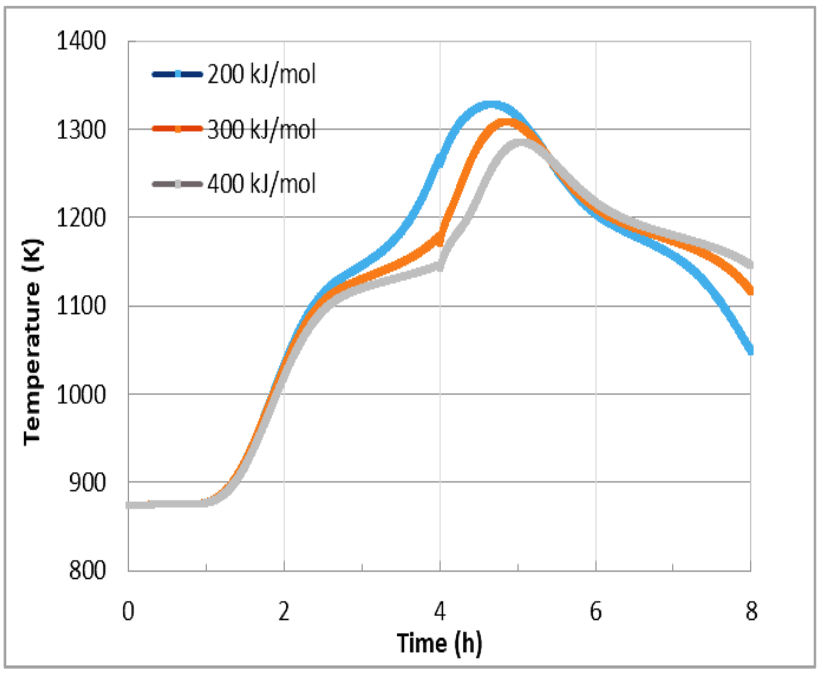

Figure 5-11 Effect of reaction enthalpy on the air outlet temperature

Figure 5-12 shows the impact of different wall thickness of the channels on air outlet temperature, when inner diameter of the channel is fixed at 0.007 m. During charging, air outlet temperature changes more gradually and reaches to lower peak value for higher wall thickness as more heat is conducted through solid walls: air temperature reached up to □1360 K for 0.001m thick wall and up to □1280 K for 0.005 m thick wall. Higher wall thickness also delays the redox reaction. During discharging also, higher wall thickness results in more gradual heat release and hence longer discharging period, in comparison with less wall thickness.

The influence of inner diameter of the channel on the air outlet temperature is shown in Figure 5-13, when wall thickness of the channel is fixed at 0.003m. In case of smaller channel diameter, the air outlet temperature increases faster and reaches to higher value during charging: it reached up to 1337 K in 3.8 hours when diameter was 0.003 m, and reached to □1318 K in 4.8 hours when diameter was 0.009 m. During discharging, air outlet temperature decreases sharply for smaller diameter, while larger diameter resulted in more gradual heat release.

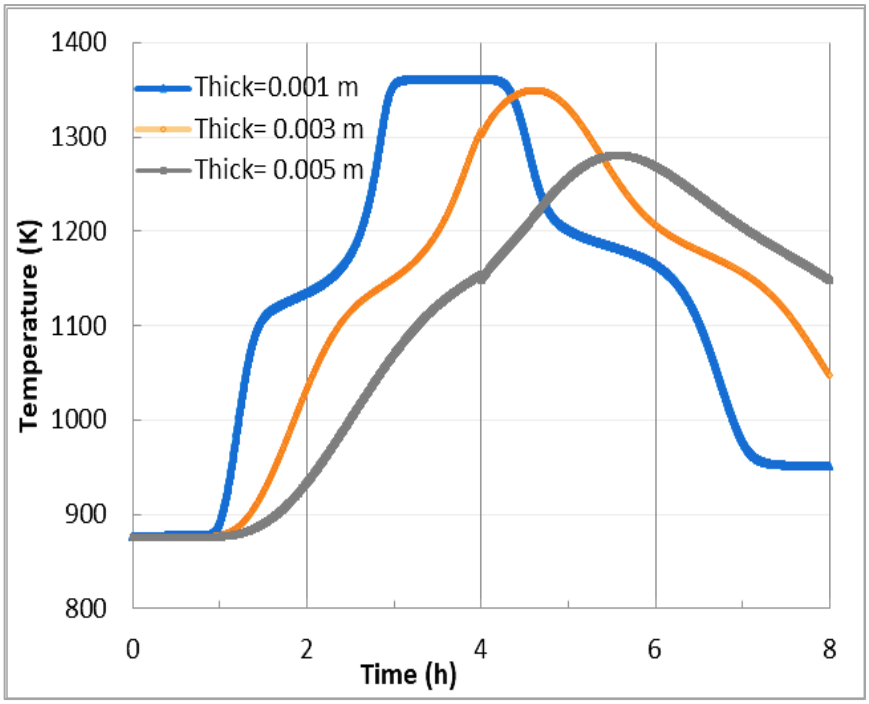

Figure 5-12 Effect of wall thickness on the air outlet temperature

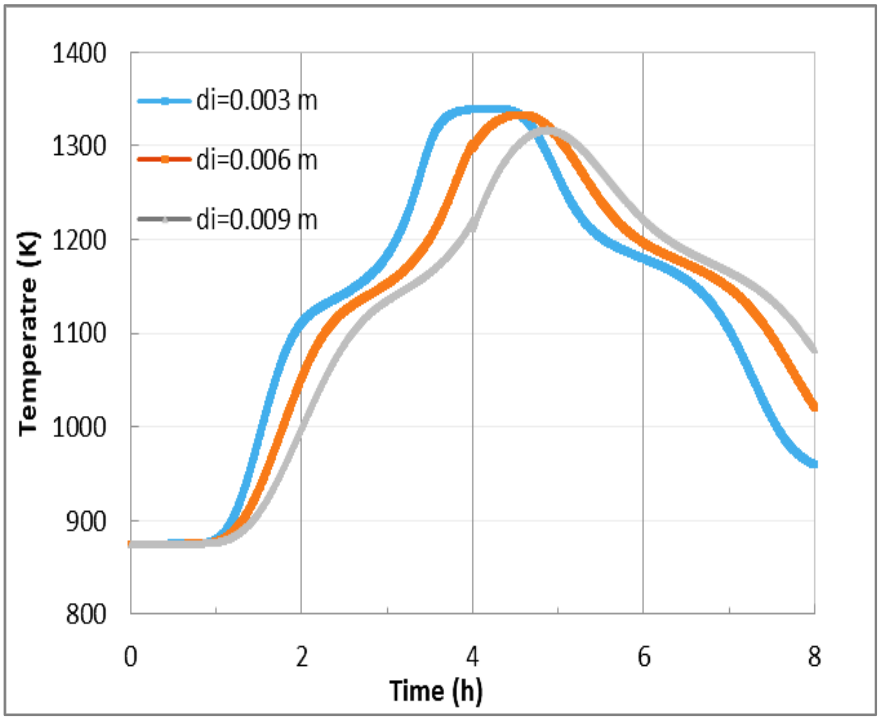

Figure 5-13 Effect of channel diameter on the air outlet temperature

5.6 Final Remarks

ThermoChemical Energy Storage (TCES) offers distinguished advantages such as high energy density, less heat losses, possibility of long-term storage and higher temperature range. However, this technology is still developing in comparison with sensible and latent heat storage, which have developed on the commercial scale. In this study, a one-dimensional model for thermochemical storage based on the redox cycle of Co3O4/CoO pair is developed. The mathematical model is based on the energy balance and reaction kinetics for the cobalt oxides. The developed model is validated against the experimental results obtained from the literature [15], since experimental data is not available at present. From this study, it is concluded that one-dimensional numerical model can reasonably predict the overall trend of thermochemical cycle, except some discrepancies.

This model can be used to study the process of thermochemical storage, understand the reaction kinetics and investigate the capability of cobalt oxides to store thermochemical energy, with less computational effort. This simulation tool was also used to conduct the parametric study, which provides guidance to carefully identify the reactive species to optimize the system performance within practical constraints. The metallic oxides which have high heat capacity offer more energy density but chemical reaction is also delayed; high reaction enthalpy improves the chemical energy storage and results in more gradual heat release, however, it also requires large energy input to carry out the chemical reaction, while change in thermal conductivity of the reactive material have less significant impact on the performance of the thermochemical storage, in comparison with reaction enthalpy and specific heat capacity. Geometric parameters like channel diameter and wall thickness also influence the thermal behaviour: with thin walls, the air outlet temperature increases quickly in charging process and decreases sharply in discharging; with big channel diameter, the air outlet temperature increases and decreases gradually during charging and discharging, respectively. Total energy stored/released from the TCES has also been calculated using the model, and compared with the experimental results. Considering the heat loss of 18% of the total energy stored/released in the storage system, the percentage relative error between simulation and experimental results is 21.6% and 16.04%, for charging and discharging, respectively. Future work will focus on the integration of TCES model in the whole system dynamic models for CSP hybrid systems.

References

1. Al-Badi, A.H., Albadi, M.H., 2012. Domestic solar water heating system in Oman: Current status and future prospects. Renew. Sustain. Energy Rev. 16, 5727–5731. doi:http://dx.doi.org/10.1016/j.rser.2012.06.007.
2. Pietzcker RC, Stetter D, Manger S, Luderer G. Using the sun to decarbonize the power sector: the economic potential of photovoltaics and concentrating solar power. Appl Energy 2014;135:704–20.
3. Xu, B., Li, P., and Chan, C., 2015. Application of phase change materials for thermal energy storage in concentrated solar thermal power plants: A review to recent developments. Applied Energy 160, 286–307.
4. S. Tescaria, G. Lantin, M. Lange, S. Breuer, C. Agrafiotis, M. Roeb, C. Sattler. 2015. "Numerical model to design a thermochemical storage system for solar power plant". Energy Procedia 75 (2015) 2137 – 2143.
5. Cot-gores, J., Castell, A., and Cabeza, L. F., 2012. "Thermochemical energy storage and conversion : A-state-of-the-art review of the experimental research under practical conditions". Renew. Sustain. Energy Rev. 16 5207–24.
6. Cabeza, L.F., 2014 Advances in Thermal Energy Storage Systems_ Methods and Applications (Woodhead Publishing Series in Energy).
7. Yu, N., Wang, R.Z., Wang, L.W., 2013. Sorption thermal storage for solar energy. Progress in Energy and Combustion Science 39, 489–514. doi:10.1016/j.pecs.2013.05.004.
8. Li T, Wang R, Kiplagat JK, Kang Y. Performance analysis of an integrated energy storage and energy upgrade thermochemical solid-gas sorption system for seasonal storage of solar thermal energy. Energy 2013;50:454-67. http://www.sciencedirect.com/science/article/pii/S0360544212009073. Last access on 30-12-2017
9. Michel B, Mazet N, Mauran S, Stitou D, Xu J. Thermochemical process for seasonal storage of solar energy: characterization and modeling of a high density reactive bed. Energy 2012;47(1):553-63 . http://www.sciencedirect.com/science/article/pii/S0360544212007074**. Last access on 30-12-2017**

10. Schaube F, Wörner A, Tamme R. High temperature thermochemical heat storage for concentrated solar power using gasesolid reactions. Journal of Solar Energy Engineering 2011;133(3):031006. http://link.aip.org/link/?SLE/133/031006/1. Last access on 30-12-2017

11. T. Nagel, H. Shao, A.K. Singh, N. Watanabe, C. Roßkopf, M. Linder, A. Wörner, O. Kolditz. Non-equilibrium thermochemical heat storage in porous media: Part 1-Conceptual model. Energy 60 (2013) 254-270.

12. K. Edem N'Tsoukpoe, Hui Liu, Nolwenn Le Pierre` s, Lingai Luo, 2009. A review on long-term sorption solar energy storage. Renewable and Sustainable Energy Reviews 13 (2009) 2385–2396.

13. Ganesh Balasubramanian, Mehdi Ghommem, Muhammad R. Hajj, William P. Wong, Jennifer A. Tomlin, Ishwar K. Puri. 2010. Modeling of thermochemical energy storage by salt hydrates. International Journal of Heat and Mass Transfer 53 (2010) 5700–5706.

14. S. Tescari, C. Agrafiotis, S. Breuer, L. de Oliveira, M. Neises-von Puttkamer, M. Roeb, C. Sattler. 2014, Thermochemical solar energy storage via redox oxides: materials and reactor/heat exchanger concepts. Energy Procedia 49 (2014)1034 – 1043.

15. Abhishek Singh, Stefania Tescari, Gunnar Lantin, Christos Agrafiotis, Martin Roeb, Christian Sattler. 2017, solar thermochemical heat storage via the Co3O4/CoO looping cycle: Storage reactor modelling and experimental validation. Solar Energy 144 (2017) 453–465.

16. Hutchings, K.N., Wilson, M., Larsen, P.A., Cutler, R.A., 2006. Kinetic and thermodynamic considerations for oxygen absorption/desorption using cobalt oxide. Solid State Ionics 177, 45–51.

17. Agrafiotis, C., Roeb, M., Sattler, C., 2016. Exploitation of thermochemical cycles based on solid oxide redox systems for thermochemical storage of solar heat. Part 4: Screening of oxides for use in cascaded thermochemical storage concepts. Solar Energy 139, 695–710.

18. Schwarzboezl P, Pomp S, Koll G, Hennecke K, Hartz T, Schmitz M, et al. The solar tower in Jülich – first operational experiences and test results. In: SolarPACES, Perpignan, France; 2010.

19. S. Tescari , A. Singh, C. Agrafiotis, L. de Oliveira, S. Breuer, B. Schlögl-Knothe, M. Roeb, C. Sattler, 2017. Experimental evaluation of a pilot-scale thermochemical storage system for a concentrated solar power plant. Applied Energy 189 (2017) 66–75.

20. Neises, M.; Tescari, S.; de Oliveira, L.; Roeb, M.; Sattler, C.; Wong, B., Solar-heated rotary kiln for thermochemical energy storage. Solar Energy 2012, 86, (10), 3040-3048.
21. Zhongyang Luo, Cheng Wang, Gang Xiao, Mingjiang Ni, Kefa Cen. 2014. Simulation and experimental study on honeycomb-ceramic thermal energy storage for solar thermal systems. Applied Thermal Engineering 73 (2014) 620-626.
22. Guangwei Yang, Gang Xiao, Tianfeng Yang, Mingjiang Ni, Kefa Cen. 2017. Thermal Kinetics of CuO/Cu2O redox system. SolarPaces 2017.
23. A.F. Mills, Heat Transfer, Second Edition, Prentice-Hall, New Jersey, 1999.
24. Armand Fopah Lele, Frédéric Kuznik, Holger U. Rammelberg, Thomas Schmidt, Wolfgang K.L. Ruck. 2015. Thermal decomposition kinetic of salt hydrates for heat storage systems. Applied Energy 154 (2015) 447–458.
25. Benoit Michel, Nathalie Mazet, Sylvain Mauran, Driss Stitou, Jing Xu. Thermochemical process for seasonal storage of solar energy: characterization and modeling of a high-density reactive bed. Energy, Elsevier, 2012, 47 (1), pp.553-563.
26. Pagkoura, C., Karagiannakis, G., Zygogianni, A., Lorentzou, S., Kostoglou, M., Konstandopoulos, G.A., Rattenburry, M., Woodhead, W.J., 2014. Cobalt oxide based structured bodies as redox thermochemical heat storage medium for future CSP plants. Sol. Energy 108, 146–163.

6 Conclusions and Future work

In the scenario of energy security, environmental conservation, economical and efficient power generation, Concentrated Solar Power (CSP) hybrid gas turbine systems based on micro Gas Turbines (mGT) are expected to play a significant role in the present and future power infrastructure. To overcome the intermittent nature of solar power and technical challenges associated with hybridization and improve the cycle efficiency, research is focused on the integration of Thermal Energy Storage (TES) in CSP hybrid gas turbine systems. TES systems have emerged as a viable solution to bridge the gap between the solar availability and power demand. In this framework, the present work has focused on the modeling of both mGT cycle and TES systems, in order to achieve a better understanding of the behavior of TES and its interaction with other components in a hybrid gas turbine system.

AE-T100 model is a steady-state simulation tool and it also possesses the diagnostic capability of the T100 cycle. First part of this study is based on the AE-T100 model development, results verification and sensitivity analysis in order to fully characterize the mGT behavior under different ambient temperatures and load. AE-T100 model has been used in real operating conditions through the Ansaldo Energia test rig AE-T100 to estimate the recuperator effectiveness at different power levels.

Finally the AE-T100 model has been applied for diagnostic aims of the whole mGT cycle with the help of two case studies from AE-T100 test rig. In the first case, AE-T100 model was able to successfully diagnose the damage in the recuperator of T100 machine. The second case study also verified the diagnostic capability of the AE-T100 tool, although it was not able to detect the exact fault in the test rig. Hence, we can state that, although the

current model AE-T100 has not the capacity to identify the exact fault in mGT cycle in some cases, however it can be effectively used to monitor the mGT operation and detect any unexpected performance.

AE-T100 model has also been applied to simulate the Humid Air Turbine (mHAT) system located at Vrije Universiteit Brussel (VUB). This involves modification in the basic AE-T100 model according to the VUB-mHAT cycle configuration. The modified AE-T100 model has been validated against the experimental data obtained from the mHAT unit at nominal and part load. Once the model was validated using real operating conditions, it has been used for monitoring the recuperator performance over large number of tests in dry mode, conducted over past five years, as well as initial tests in wet mode, from the VUB-mHAT system. In conclusion, this work has proved the modeling capability of AE-T100 tool to simulate the mHAT cycle with reasonable accuracy, first diagnostic application of the AE-T100 tool, in dry mode. Hence, this preliminary analysis will provide basis for more detail diagnostics of the mHAT cycle using AE-T100 tool, over the longer time scale under wet operation, in future.

The second part of this thesis is based on the study of thermal energy storage (TES). Dynamic modeling and experimental validation of a sensible heat storage system has been carried out. The modeling work compares two time-dependent approaches: a CFD model using ANSYS-FLUENT® code and a simplified model using the simulation tool TRANSEO, developed by TPG.

Experimental validation of CFD model results highlighted that 2D discretization of the TES can well represent the thermal stratification, but it suffers from high computational cost, thus it is not useful for CSP plant dynamic analysis and for control development of the whole CSP plant. However, this can be used for the detail analysis and calibration of more simple models. Experimental validation of TRANSEO model has highlighted that 1D discretization can also predict the thermal gradient inside the TES, but with less accuracy. However, due to fast and simplified approach, TRANSEO model is applicable for dynamic analysis, real time modeling and control development.

In addition to the modeling scope of both models, this study also highlighted the potential of the TES systems based on the monolithic structures for hybrid gas turbines

systems in comparison with packed beds and use of this TES system for long term thermal storage applications.

In addition to the sensible heat storage, the author has also studied the Thermo-Chemical heat Storage (TCS) system. A simplified 1D model for TCS system based on the redox cycle of Co_3O_4/CoO pairs was developed and validated against a reference model from open literature. This simplified model provides the basis for more detailed modeling of TCS system, to study the principle of thermochemical storage, understand the reaction kinetics and optimize the system performance with the help of parametric study of the reactive species.

Future work

Mainly the future work will involve development of a single simulation tool merging the knowledge and modelling capabilities developed for mGT cycle and TES systems in this study. This tool will be used for assessing the performance, at design, off-design and transient conditions of the microturbine-based CSP hybrid systems.

In this work, we have proved the capability of the AET100 simulation tool to adapt to a different plant layout i.e mHAT cycle and its potential to be used as a diagnostic tool for the recuperator performance analysis of the VUB-mHAT test rig, in dry mode. In future, a more in-depth analysis of the mHAT cycle is planned using the AET100 tool, over larger number of experiments, under wet operation.

Future work will focus on integration of thermochemical storage model in plant dynamic model for CSP hybrid systems. Currently, experimental work is ongoing on the thermochemical storage system at Zhejiang University.

Publications

Mahmood, M., Martini, A., Traverso, A., Bianchi, E.
Model Based Diagnostics of AE-T100 Micro Gas Turbine‖, ASME Paper GT2016-57671.

Mahmood, M., Martini, A., Traverso, A.
Fault Detection through Model Based Diagnostics of AE-T100 Micro Gas Turbine‖. ASME Paper GT2017- 64619.

Mahmood, M., Martini, A., Massardo, A.F., De Paepe, W.
Model Based Diagnostics Of Ae-T100 Micro Humid Air Turbine Cycle‖. ASME Paper GT2018- 75979.

Mariam Mahmood, Alberto Traverso, Alberto Nicola Traverso, Aristide F. Massardo, Davide Marsano, Carlo Cravero.
Thermal energy storage for CSP hybrid gas turbine systems: Dynamic modelling and experimental validation‖. Applied Energy Vol.212, 2018, pp: 1240–1251.

Annexure 1

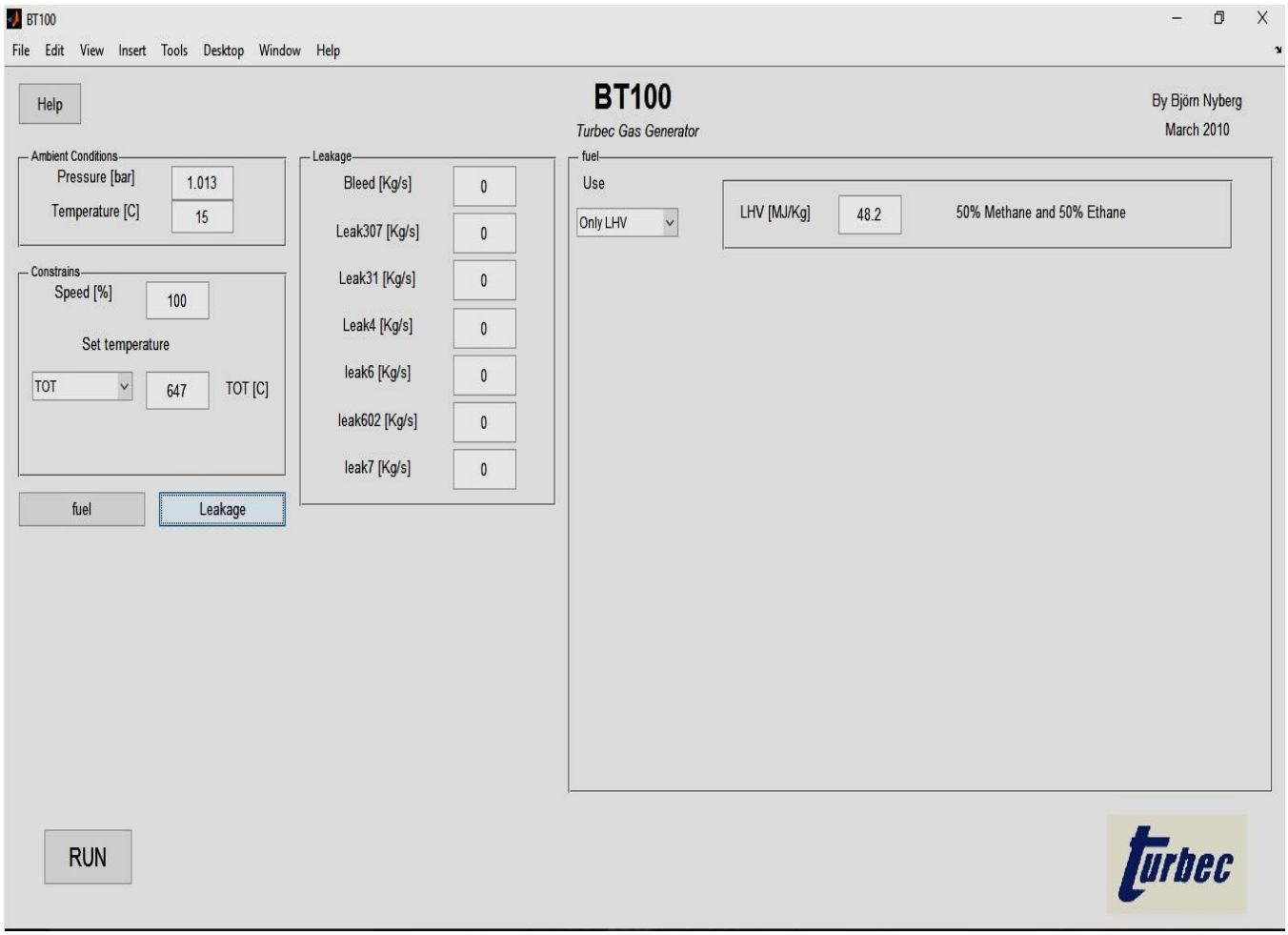
BT100
File Edit View Insert Tools Desktop Window Help
Help
BT100
Turbec Gas Generator
By Björn Nyberg
March 2010
Ambient Conditions
Pressure [bar]
1.013
Temperature [C]
15
Constrains
Speed [%]
100
Set temperature
TOT
647
TOT [C]
fuel
Leakage
Leakage
Bleed [Kg/s]
0
Leak307 [Kg/s]
0
Leak31 [Kg/s]
0
Leak4 [Kg/s]
0
leak6 [Kg/s]
0
leak602 [Kg/s]
0
leak7 [Kg/s]
0
fuel
Use
Only LHV
LHV [MJ/Kg]
48.2
50% Methane and 50% Ethane
RUN
Turbec

Annexure II

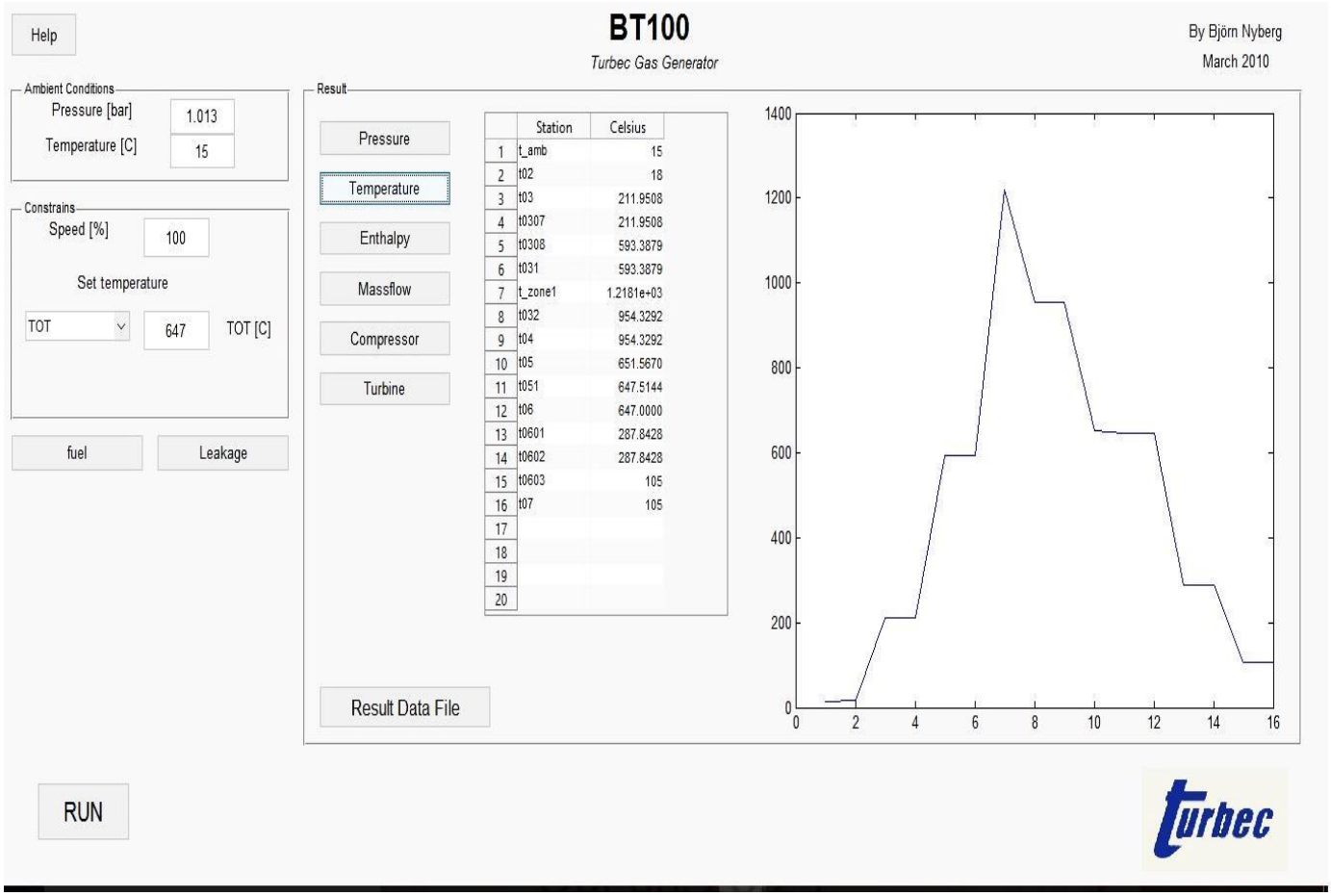
Help
BT100
Turbec Gas Generator
By Björn Nyberg
March 2010
Ambient Conditions
Pressure [bar]
1.013
Temperature [C]
15
Constrains
Speed [%]
100
Set temperature
TOT
647
TOT [C]
fuel
Leakage
Result
Pressure
Temperature
Enthalpy
Massflow
Compressor
Turbine
Result Data File
RUN
Station
Celsius
1 t_amb 15
2 t02 18
3 t03 211.9508
4 t0307 211.9508
5 t0308 593.3879
6 t031 593.3879
7 t_zone1 1.2181e+03
8 t032 954.3292
9 t04 954.3292
10 t05 651.5670
11 t051 647.5144
12 t06 647.0000
13 t0601 287.8428
14 t0602 287.8428
15 t0603 105
16 t07 105
17
18
19
20
1400
1200
1000
800
600
400
200
0
0
2
4
6
8
10
12
14
16
turbec

Annexure III

Annexure IV

UDF for inlet air temperature for TES charging

```
#include"udf.h"
DEFINE_PROFILE(inlet_temperature,thread,position )
{
face_t f;
begin_f_loop(f,thread)
{
real t = RP_Get_Real("flow-time");
if ( t <= 100.0 )
{
F_PROFILE(f,thread,position) = 379.48 + 0.0004*t;
}
elseif (100.0 < t && t <= 180.0 )
{
F_PROFILE(f,thread,position) = -8.34641*pow(10,-6)*pow(t,4.0)+ 5.49800*pow(10,-3)*pow(t,3.0)- 1.35243*pow(t,2.0)+ 1.47648*pow(10,2.0)*t - 5.51650*pow(10,3.0);}
elseif (180.0 < t && t <= 200.0 )
{
F_PROFILE(f,thread,position) = 0.2716*t + 494.4;
}
elseif (200.0 < t && t <= 400.0 )
{
F_PROFILE(f,thread,position) = 328.14*pow(t,0.097);
}
elseif (400.0 < t && t <= 600.0 )
{
F_PROFILE(f,thread,position) = 315.73*pow(t,0.1035);
}
elseif (600.0 < t && t <= 800.0 )
{
F_PROFILE(f,thread,position) = 317.74*pow(t,0.1026);
}
elseif (800.0 < t && t <= 1000.0 )
{
F_PROFILE(f,thread,position) = 311.12*pow(t,0.1058);
}
elseif (1000.0 < t && t <= 1300.0 )
{
F_PROFILE(f,thread,position) = 309.21*pow(t,0.1067);
}
elseif (1300.0 < t && t <= 1600.0 )
```

```
{
F_PROFILE(f,thread,position) =  0.0524*t + 596.97;
}
elseif (1600.0 < t && t <= 1900.0 )
{
F_PROFILE(f,thread,position) =   301.12*pow(t,0.1106);
}
else if (1900.0 < t && t <= 2200.0 )
{
F_PROFILE(f,thread,position) =   0.0397*t + 618.6;
}
else if (2200.0 < t && t <= 2600.0 )
{
F_PROFILE(f,thread,position) =   341.25*pow(t,0.0945);
}
else if (2600.0 < t && t <= 3000.0 )
{
F_PROFILE(f,thread,position) =   0.0177*t + 671.54;
}
else if (3000.0 < t && t <= 3400.0 )
{
F_PROFILE(f,thread,position) =   580.75*pow(t,0.0277);
}
else
{
F_PROFILE(f,thread,position) = 727.82;
}
}
end_f_loop(f,thread)
}
```